ELECTRONIC STRUCTURE OF GRAPHENE UNDER THE INFLUENCE OF EXTERNAL FIELDS

A DISSERTATION SUBMITTED TO

THE DEPARTMENT OF PHYSICS

AND THE GRADUATE SCHOOL OF ENGINEERING AND SCIENCE

OF BILKENT UNIVERSITY

IN PARTIAL FULFILLMENT OF THE REQUIREMENTS

FOR THE DEGREE OF

DOCTOR OF PHILOSOPHY

By

Selcen İslamoğlu

August 2012

I certify that I have read this thesis and that in my opinion it is fully adequate, in scope and in quality, as a dissertation for the degree of Doctor of Philosophy.

Prof. Dr. Oğuz Gülseren(Supervisor)

I certify that I have read this thesis and that in my opinion it is fully adequate, in scope and in quality, as a dissertation for the degree of Doctor of Philosophy.

Assoc. Prof. Dr. M. Özgür Oktel

I certify that I have read this thesis and that in my opinion it is fully adequate, in scope and in quality, as a dissertation for the degree of Doctor of Philosophy.

Asst. Prof. Dr. Coşkun Kocabaş

I certify that I have read this thesis and that in my opinion it is fully adequate, in scope and in quality, as a dissertation for the degree of Doctor of Philosophy.

Prof. Dr. Şinasi Ellialtıoğlu

I certify that I have read this thesis and that in my opinion it is fully adequate, in scope and in quality, as a dissertation for the degree of Doctor of Philosophy.

Asst. Prof. Dr. Hande Toffoli (Üstünel)

Approved for the Graduate School of Engineering and Science:

Prof. Dr. Levent Onural
Director of the Graduate School

iii

ABSTRACT

ELECTRONIC STRUCTURE OF GRAPHENE UNDER THE INFLUENCE OF EXTERNAL FIELDS

Selcen İslamoğlu
Ph.D. in Physics
Supervisor: Prof. Dr. Oğuz Gülseren
August 2012

In this thesis, the electronic structure of graphene under the influence of external fields such as strain or magnetic fields is investigated by using tight-binding method. Firstly, we study graphene for a band gap opening due to uniaxial strain. In contrast to the literature, we find that by considering all the bands (both σ and π bands) in graphene and including the second nearest neighbor interactions, there is no systematic band gap opening as a function of applied strain. Our results correct the previous works on the subject. Secondly, we examine the band structure and Hall conductance of graphene under the influence of perpendicular magnetic field. For graphene, we demonstrate the energy spectrum in the presence of magnetic field (Hofstadter Butterfly) where all orbitals are included. We recover both the usual and the anomalous integer quantum Hall effects depending on the proximity of the Dirac points for pure graphene and the usual integer quantum Hall effect for pure square lattice. Then, we explore the evolution of electronic properties when imperfections are introduced systematically to the system. We also demonstrate the results for a square lattice which has a distinct position in cold atom experiments. For the energy spectrum of imperfect graphene and square lattice under magnetic field (Hofstadter Butterflies), we find that impurity atoms with smaller hopping constants result in highly localized states which are decoupled from the rest of the system. The bands associated with these states form close to $E = 0$ eV line. On the other hand, impurity atoms with higher hopping constants are strongly coupled with the neighboring atoms. These states modify the Hofstadter Butterfly around the minimum and maximum values of the energy and for the case of graphene they form two self similar bands decoupled from the original butterfly. We also show that the bands and gaps due to the impurity states are robust with respect to the second order hopping. For the Hall conductance, in accordance with energy spectra, the localized states associated to the smaller hopping constant impurities or vacancies do

not contribute to Hall conduction. However the higher hopping constant impurities are responsible for new extended states which contribute to Hall conduction. Our results for Hall conduction are also robust with respect to the second order interactions.

ÖZET

GRAFENİN ELEKTRONİK YAPISININ DIŞ ALANLARIN ETKİSİ ALTINDA İNCELENMESİ

Selcen İslamoğlu

Fizik, Doktora

Tez Yöneticisi: Prof. Dr. Oğuz Gülseren

Ağustos 2012

Bu tezde grafenin elektronik yapısının mekanik gerinim veya manyetik alan gibi dış alanların etkisiyle nasıl değiştiği sıkı-bağlanım metoduyla incelenmiştir. Öncelikle grafenin tek eksenli gerinim altında enerji bant açıklığı gösterip göstermediğini inceledik. Literatürden farklı olarak, grafenin bütün bantları (hem σ hem π bantları) düşünüldüğünde ve ikincil komşu etkileşimleri hesaba katıldığında grafende uygulanan gerinimin fonksiyonu olarak değişen bir bant açıklığı görülmemektedir. Bizim sonuçlarımız bu alandaki önceki çalışmaların sonuçlarını düzeltmektedir. İkinci olarak, grafenin bant yapısını ve Hall iletkenliğini grafen yüzeyine dik manyetik alanın etkisi altında inceledik. Grafenin manyetik alan altındaki enerji bant yapısını (Hofstadter Kelebeği) tüm orbitaller dahilinde gösterdik. Saf grafen için olağan ve kuraldışı, saf kare ağ örgüsü için de olağan tamsayı kuantum Hall etkilerini gözlemledik. Daha sonra, elektronik özelliklerinin sisteme sistematik olarak dahil edilen safsızlıklara göre değişimini çalıştık. Ayrıca, soğuk atom deneylerinde önemli bir yere sahip olan kristal kare ağ örgüsüne ait sonuçları da benzer şekilde elde ettik. Kusurlu grafen ve kare ağ örgüsünün manyetik alan altındaki enerji tayfı (Hofstadter Kelebekleri) için, küçük sekme katsayısına sahip kusurlar, yüksek oranda yerel olarak konumlanmış ve sistemin geri kalanından ayrılmış öz-değerlik durumlarına sebebiyet vermektedir. Bu durumlarla ilişkili bantlar $E = 0$ eV çizgisine yakın olarak biçimlenmiştir. Diğer taraftan, büyük sekme katsayısına sahip kusurlar ise komşu atomlarla yüksek oranda bağlaşıma girmişlerdir. Bu öz-değerlik durumları Hofstadter Kelebekleri'ni enerji değerlerinin en küçük ve en büyük olduğu bölgelerde değişikliğe uğratmakta ve grafen söz konusu olduğunda özgün kelebekten tamamen ayrılmış iki adet öz-benzeş bant oluşturmaktadır. Ancak, kusur öz-değerlik durumları nedeniyle oluşan bantlar ve bant açıklıkları ikinci derece sekmeye karşı dirençlidir. Hall iletkenliği için de, enerji tayfındaki değişikliklerle uyumlu olarak,

küçük sekme katsayısına sahip kusur ve boşluklar kökenli yüksek oranda yerel olarak konumlanmış öz-değerlik durumlarının Hall iletkenliğine katkıda bulunmadıkları soylenebilir. Fakat, görece büyük sekme katsayısına sahip kusur atomları Hall iletkenliğine katkıda bulunan yersizleşmiş yeni öz-değerlik durumlarının oluşmasına neden olmaktadır. Hall iletkenliği hesaplarımızın sonuçları da ikinci derece etkileşimler karşında kalıcıdır.

Anahtar sözcükler: Grafen, sıkı-bağlanım metodu, noktasal kusurlar, eksiklikler, gerinim, manyetik alan, Hofstadter Kelebekleri, Hall iletkenliği, İki boyutlu elektronik sistemler .

Acknowledgement

Contents

List of Figures

List of Tables

Chapter 1

Introduction

Carbon is the basic element of Nature. Various structures having carbon atoms have been popular fields of research through the last few decades. Among these systems, two dimensional (2D) graphene, composed of only carbon atoms, has a basic and a unique position in order to examine the other carbon-based systems [1]. It became experimentally accessible after the isolation as single layer by mechanical exfoliation [2, 3]. As a result, it is one of the systems that attracted the most attention in recent years. There are several works that concentrate on the electronic and mechanical properties of graphene [4, 5, 6, 7]. The band structure of graphene was determined in 1947 [8]. Graphene exhibits several unusual properties because of the Dirac points appearing in its band structure. The π bands due to the p_z orbitals of graphene form conic shapes and the conduction and valance bands touch each other at Dirac points. These bands of graphene are unique in 2D electronic systems, where the relativistic quantum mechanics governs the system due to the linear dispersion of Dirac cones. The behavior of Dirac fermions under magnetic fields and electrostatic potentials is a popular interest for researchers [4, 5, 9, 10, 11, 12]. One of the main consequence of graphene's band structure is the observation of anomalous integer quantum Hall effect in low magnetic fields which was predicted by earlier calculations [12, 13]. Soon after the discovery of the anomalous integer quantum Hall effect in graphene [5, 14], many theoretical studies discussing the Hall conductance in low magnetic field

regime were reported [15, 16, 17, 18, 19].

One of the most popular questions asked by researchers is whether it is possible to apply band gap engineering on graphene. To investigate this point, the effects of uniaxial strain on graphene's band structure has been determined theoretically as well as experimentally [20, 21, 22, 23, 24, 25, 26]. The most interesting result was reported by Castro-Neto *et al.* which indicated that it is possible to obtain a band gap opening in graphene by applying $\sim$ 24 % uniaxial strain due to the merging of the Dirac cones [27, 28]. They have used the nearest neighbor tight-binding method which is a very practical approach and it is capable of investigating the electronic structure in a smart way. The analytical tight-binding method applied to graphene was published in 2002 [29]. However, in that paper, the only bonds under consideration were the π bonds, and the calculation contained only the 1st nearest neighbors, since this level of approximation was thought to provide information about the one-dimensional nanotube band structure. Since the band structure of graphene is not composed of only π bonds, we provide a detailed calculation about the band structure which contains σ bonds as well as the π bonds.

The effects of the external field induced changes on the electronic structure of graphene is a very interesting and promising problem. In this thesis, we concentrate on two external fields: strain and magnetic field which can be investigated by the tight-binding method. Firstly, we demonstrate the results of 2nd nearest neighbor tight-binding approach applied to single-layer graphene under strain which has an opposing result to what was reported in the literature. Another recent study suggests that, with 26.5% of uniaxial strain the system develops a 45.5 meV band gap [30]. We claim that, it is impossible to get a band gap opening in monolayer graphene by applying uniaxial strain. Secondly, we examine graphene and a square lattice which is also a 2D system under magnetic field. The choice of the square lattice is due to its simple yet representative nature. Moreover it also has a unique position in cold atom experiments and calculations [31, 32, 33, 34]. We use tight-binding method again up to second order interactions through which we obtain the energy spectra under magnetic field (*Hofstadter Butterflies*) and

the Hall conductance values. In addition we demonstrate the effects of lattice imperfections on the electronic structure when the system is subjected to magnetic field.

Graphene is composed of a layer of hexagonally arranged carbon atoms, which has a structure similar to honeycomb. It is a sp^2 hybridized structure, in which the hybridization of one s orbital with two p orbitals (p_x and p_y) leads to the formation of σ bonds among the carbon atoms. As a result of this, graphene has a trigonal planar geometry with carbon atoms which are separated by 1.42 Å. The remaining p orbital (p_z) which is perpendicular to the plane of consideration, is responsible for the covalent bonding to upper or lower layer neighboring atoms which has a consequence of the formation of π bonds. In this thesis, we mostly concentrated on the electronic structure due to π bonds which are the leading features for magnetic field considerations, however for the case of strain the σ bonds have an important role.

In 2D, the Bloch electrons display an unusual behavior under magnetic field. When there is a perpendicular magnetic field applied to the system the spectrum has a fractal structure which depends on the magnetic flux, the chemical potential and the temperature. The fractal nature of this spectrum originates from two different length scales competing with each other: The length scale of the unit cell which is governed by the lattice constant and the magnetic length of the system. This competition gives rise to the phenomenon called "frustration" [35]. This unique spectrum is actually a phase diagram of the system with infinitely many phases. The spectrum consist of recursive subbands which form phase boundaries around the gaps. This structure of bands and gaps is generated by the adiabatic changes in the magnetic flux and the chemical potential. The number of subbands is dependent on some number connected to the magnitude of the magnetic field. Hypothetically, this number "q" can be represented as a function of the fraction of magnetic flux per plaquette penetrating into the system to flux quanta. This ratio actually is the ratio of two characteristic periods of the system: period of a single electron in a state with crystal momentum $2\pi\hbar/a$, "a" is being simply the lattice constant and the other period is the reciprocal of the cyclotron frequency [36]. The energy spectrum of these electrons display a

self-similar structure. The primary work was performed by Douglas R. Hofstadter in 1976, which concentrates on the square lattice and later these unique spectra have been called by his name: The Hofstadter Butterflies [36] for several 2D electronic systems. Several works concentrated on the energy spectra of various examples of the 2D lattices, such as square, triangular, hexagonal, and honeycomb lattices [37, 38, 39, 40, 41, 42, 43]. Although graphene is a non-Bravais lattice, with two atoms in its basis, it still represents a fractal energy spectrum under magnetic field.

The Hofstadter Butterfly has another interesting property. It gives information about the magnetotransport properties of the system. Each gap in the energy spectrum has a certain Hall conductance value within a gap. These values are associated to every gaps and they stay constant within the gaps. These constant values of Hall conductance indeed correspond to the Hall conductance plateaus when the conductance is plotted as a function of Fermi Energy. The conductance values of the gaps can be determined by the Diophantine equation whose solutions are known as Chern numbers [44] for the square and honeycomb lattices as long as the Fermi energy or the chemical potential lies in a gap. The relation between the Hall conductance and the Chern numbers originates from the topological aspects of the Hall conductance. However, since the Diophantine equation is no longer valid when there are imperfections in the system, we use a general Kubo formula for Hall conductance calculation which gives results regardless of the position of the Fermi energy.

The thesis is organized as follows: In the first chapter, we demonstrate the general methodologies that we used in our calculations. Then, we concentrate on the electronic behaviors of graphene under two external fields: Strain and perpendicular magnetic field. For the magnetic field, we also studied the square lattice. Moreover, we monitor the changes on the energy spectra and the Hall conductance as a function of imperfections introduced to the systems periodically for both graphene and the square lattice.

Chapter 2

The Tight-Binding Method

2.1 The Tight-Binding Approximation—Overview

Tight-binding approximation -also referred to as Linear Combination of Atomic Orbitals (LCAO)- is one of the simplest tools for calculating band structures. In this method, the orbitals which are based on atomic states are used as a basis for the expansion of the crystal wavefunction. Since the crystal wavefunctions are tightly bound to the atoms, the name "tight-binding" was given for this method.

Suppose that the orbital set $\phi_l(\mathbf{r} - \mathbf{t}_i)$ is centered at the position of the ith atom, denotes the set of atomic wavefunctions where $\mathbf{t}_i$ is the position of the ith atom and l is one of the angular momentum characters such as s, p, d and *etc.* Then, we can use this set of wavefunctions as a basis for expanding the crystal wavefunctions $\{\chi_{\mathbf{k}li}(\mathbf{r})\}$ which obey the Bloch's theorem:

$$\chi_{\mathbf{k}li}(\mathbf{r}) = \frac{1}{\sqrt{N}} \sum_{\mathbf{R}'} e^{i\mathbf{k}\cdot\mathbf{R}'} \phi_l(\mathbf{r} - \mathbf{t}_i - \mathbf{R}') \quad , \tag{2.1}$$

N is the number of unit cells in the crystal,

$$
\begin{aligned}
\chi_{\mathbf{k}li}(\mathbf{r} + \mathbf{R}) &= \frac{1}{\sqrt{N}} \sum_{\mathbf{R}'} e^{i\mathbf{k}\cdot\mathbf{R}'} \phi_l(\mathbf{r} + \mathbf{R} - \mathbf{t}_i - \mathbf{R}') \\
&= \frac{1}{\sqrt{N}} \sum_{\mathbf{R}'} e^{i\mathbf{k}\cdot(\mathbf{R}'-\mathbf{R})} e^{i\mathbf{k}\cdot\mathbf{R}} \phi_l(\mathbf{r} + \mathbf{R} - \mathbf{t}_i - \mathbf{R}') \\
&= e^{i\mathbf{k}\cdot\mathbf{R}} \frac{1}{\sqrt{N}} \sum_{\mathbf{R}'} e^{i\mathbf{k}\cdot(\mathbf{R}'-\mathbf{R})} \phi_l(\mathbf{r} - \mathbf{t}_i - (\mathbf{R}' - \mathbf{R})) \\
&= e^{i\mathbf{k}\cdot\mathbf{R}} \frac{1}{\sqrt{N}} \sum_{\mathbf{R}''} e^{i\mathbf{k}\cdot\mathbf{R}''} \phi_l(\mathbf{r} - \mathbf{t}_i - \mathbf{R}'') \\
&= e^{i\mathbf{k}\cdot\mathbf{R}} \chi_{\mathbf{k}li}(\mathbf{r}),
\end{aligned}
\tag{2.2}
$$

and $\mathbf{R}'' = \mathbf{R}' - \mathbf{R}$ is just another lattice vector. The single particle eigenstates can be expanded via these functions as follows:

$$
\psi_{\mathbf{k}}^{(n)} = \sum_{i,l} c_{\mathbf{k}il}^{(n)}(\mathbf{r}) \chi_{\mathbf{k}li}(\mathbf{r}).
\tag{2.3}
$$

Under these circumstances the single particle Schrödinger equation now becomes:

$$
\begin{aligned}
H^{sp}\psi_{\mathbf{k}}^{n}(\mathbf{r}) &= \epsilon_{\mathbf{k}}\psi_{\mathbf{k}}^{n}(\mathbf{r}); \\
\sum_{i,l}[\langle \chi_{\mathbf{k}mj}|H^{sp}|\chi_{\mathbf{k}li}\rangle - \epsilon_{\mathbf{k}}^{(n)}\langle \chi_{\mathbf{k}mj}|\chi_{\mathbf{k}li}\rangle]c_{\mathbf{k}li}^{(n)} &= 0
\end{aligned}
\tag{2.4}
$$

Now, we have two sets of integrals to deal with. The first one $\langle \chi_{\mathbf{k}mj}|\chi_{\mathbf{k}li}\rangle$ are "overlap matrix elements" which can be defined as follows

$$
\begin{aligned}
\langle \chi_{\mathbf{k}mj}|\chi_{\mathbf{k}li}\rangle &= \frac{1}{N} \sum_{\mathbf{R}',\mathbf{R}''} e^{i\mathbf{k}\cdot(\mathbf{R}-\mathbf{R}'')} \langle \phi_m(\mathbf{r} - \mathbf{t}_j - \mathbf{R}'')|\phi_l(\mathbf{r} - \mathbf{t}_i - \mathbf{R}')\rangle \\
&= \frac{1}{N} \sum_{\mathbf{R},\mathbf{R}'} e^{i\mathbf{k}\cdot\mathbf{R}} \langle \phi_m(\mathbf{r} - \mathbf{t}_j)|\phi_l(\mathbf{r} - \mathbf{t}_i - \mathbf{R}')\rangle \\
&= \sum_{\mathbf{R}} e^{i\mathbf{k}\cdot\mathbf{R}} \langle \phi_m(\mathbf{r} - \mathbf{t}_j)|\phi_l(\mathbf{r} - \mathbf{t}_i - \mathbf{R})\rangle
\end{aligned}
$$

The $1/N$ factor drops out since there is no more explicit dependence on $\mathbf{R}'$ owing to crystal symmetry. In a similar manner one can calculate the second integral

$\langle \chi_{\mathbf{k}mj}|H^{sp}|\chi_{\mathbf{k}li}\rangle$;

$$\langle \chi_{\mathbf{k}mj}|H^{sp}|\chi_{\mathbf{k}li}\rangle = \sum_{\mathbf{R}} e^{i\mathbf{k}\cdot\mathbf{R}}\langle \phi_m(\mathbf{r}-\mathbf{t}_j)|H^{sp}|\phi_l(\mathbf{r}-\mathbf{t}_i-\mathbf{R})\rangle \qquad (2.5)$$

One of the main approximations behind the tight-binding theory is "the orthogonal basis approximation", which approximates by a diagonal one i.e. the overlap matrix (represented by S), elements to be nonzero if and only if they are acting for the same orbitals on the same atom such that;

$$\langle \phi_m(\mathbf{r}-\mathbf{t}_j)|\phi_l(\mathbf{r}-\mathbf{t}_i-\mathbf{R})\rangle = \delta_{lm}\delta_{ij}\delta(\mathbf{R}) \quad . \qquad (2.6)$$

In fact this is just a useful assumption, since if the overlap matrix elements were to be strictly zero for different orbitals, then we would have no interactions among the nearest neighbors. For the Hamiltonian matrix elements we have a similar situation, if they are acting for the same orbitals on the same atom we get the "on-site" energies:

$$\langle \phi_m(\mathbf{r}-\mathbf{t}_j)|H^{sp}|\phi_l(\mathbf{r}-\mathbf{t}_i-\mathbf{R})\rangle = \delta_{lm}\delta_{ij}\delta(\mathbf{R})\epsilon_l \qquad (2.7)$$

If the orbitals are on different atoms but these atoms are located at the nearest neighbor sites which are represented by vector $\mathbf{d}_{nn}$;

$$\langle \phi_m(\mathbf{r}-\mathbf{t}_j)|H^{sp}|\phi_l(\mathbf{r}-\mathbf{t}_i-\mathbf{R})\rangle = \delta((\mathbf{t}_j-\mathbf{t}_i-\mathbf{R})-\mathbf{d}_{nn})V_{lm,ij} \qquad (2.8)$$

we obtain the $V_{lm,ij}$ "hopping matrix elements". The on-site energies and the hopping matrix elements and the overlap matrix elements are parameterized and tabulated [45, 46].

For generalized tight-binding method, the off-diagonal elements of the overlap matrix S are not necessarily non zero. In the presence of non zero values for overlap matrix elements, the energy eigenvalues are the solutions of:

$$det(H - SE) = 0 \quad .$$

However, this equation can be reduced to orthogonal tight-binding method:

$$det(H - IE) = 0 \quad , \qquad (2.9)$$

by Löwdin transformation. In our tight-binding calculations our parameter are modified in accordance with the generalized tight-binding, however we solve Eq. 2.9.

2.2 Tight-Binding Method for Mono-layer Graphene

Graphene has a hexagonal lattice structure which can be constructed by two lattice vectors,

$$\vec{a_1} = \frac{a\sqrt{3}}{2}\hat{x} + \frac{a}{2}\hat{y} \tag{2.10}$$

$$\vec{a_2} = \frac{a\sqrt{3}}{2}\hat{x} - \frac{a}{2}\hat{y} \tag{2.11}$$

where a is the distance between the carbon atoms. The reciprocal lattice vectors can be calculated from the basis vectors. In addition, graphene has two identical atoms in its basis, which are labeled as atoms type A and type B, as shown in Figure 2.1.

According to the tight-binding method, the Hilbert space which is spanned by the atomic-like orbitals is able to describe the wavefunction solutions of the Schrödinger equation [45]. These wavefunctions satisfy Bloch's Theorem due to the translational symmetry. Under these circumstances, the tight binding Hamiltonian for graphene can be written as an 8×8 matrix, including the interactions of one s and three p orbitals. A convenient way to visualize this matrix is writing it as a composite of four blocks according to the consideration of atoms A and B.

$$H = \begin{bmatrix} H^{AA} & H^{AB} \\ H^{BA} & H^{BB} \end{bmatrix}, \tag{2.12}$$

Each of H^{AA}, H^{AB}, H^{BA}, and H^{BB} are 4×4 matrices denoting the orbital interactions of atom A with itself, atom A and atoms B, atom B atoms A, and atom B with itself, respectively. The eigenvalues of this Hamiltonian give the desired energy values. In our calculations, we did not take the overlap matrix into account, since its already implemented through the parameter we use. For more
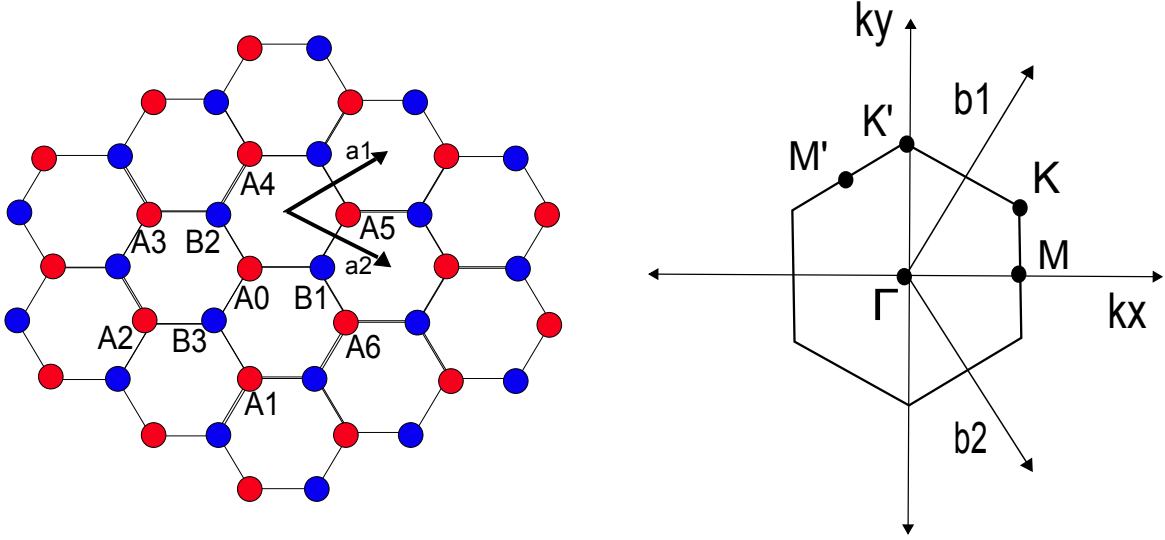
Figure 2.1: Graphene in real and reciprocal space. The nearest neighbors of atom $A0$ up to 2nd order are presented in the first picture. The high symmetry points used in the construction of a route in drawing the band structure are shown in the second figure.

accurate energy values, instead we took our calculations two steps further via inclusion of p_x and p_y orbitals and also the second nearest neighbor interactions into the calculations in comparison to the similar work done before [27]. As an example to the components of the main Hamiltonian matrix given in equation 2.12, H^{AA} and H^{AB} are displayed below.

$$H^{AA} = \begin{bmatrix} \langle 2S^A|H|2S^A\rangle & \langle 2S^A|H|2P_x^A\rangle & \langle 2S^A|H|2P_y^A\rangle & \langle 2S^A|H|2P_z^A\rangle \\ \langle 2P_x^A|H|2S^A\rangle & \langle 2P_x^A|H|2P_x^A\rangle & \langle 2P_x^A|H|2P_y^A\rangle & \langle 2P_x^A|H|2P_z^A\rangle \\ \langle 2P_y^A|H|2S^A\rangle & \langle 2P_y^A|H|2P_x^A\rangle & \langle 2P_y^A|H|2P_y^A\rangle & \langle 2P_y^A|H|2P_z^A\rangle \\ \langle 2P_z^A|H|2S^A\rangle & \langle 2P_z^A|H|2P_x^A\rangle & \langle 2P_z^A|H|2P_y^A\rangle & \langle 2P_z^A|H|2P_z^A\rangle \end{bmatrix}$$

$$H^{AB} = \begin{bmatrix} \langle 2S^A|H|2S^B\rangle & \langle 2S^A|H|2P_x^B\rangle & \langle 2S^A|H|2P_y^B\rangle & \langle 2S^A|H|2P_z^B\rangle \\ \langle 2P_x^A|H|2S^B\rangle & \langle 2P_x^A|H|2P_x^B\rangle & \langle 2P_x^A|H|2P_y^B\rangle & \langle 2P_x^A|H|2P_z^B\rangle \\ \langle 2P_y^A|H|2S^B\rangle & \langle 2P_y^A|H|2P_x^B\rangle & \langle 2P_y^A|H|2P_y^B\rangle & \langle 2P_y^A|H|2P_z^B\rangle \\ \langle 2P_z^A|H|2S^B\rangle & \langle 2P_z^A|H|2P_x^B\rangle & \langle 2P_z^A|H|2P_y^B\rangle & \langle 2P_z^A|H|2P_z^B\rangle \end{bmatrix}$$
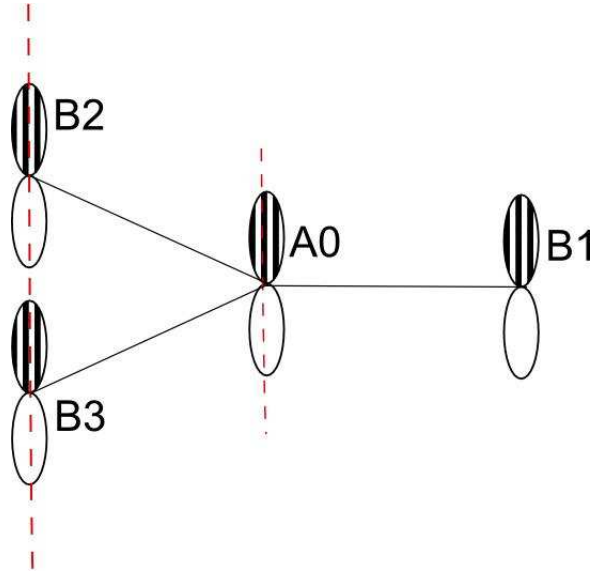
Figure 2.2: The orientations of p_y orbitals for nearest neighbor atoms $A0$, $B1$, $B2$, and $B3$

When there is no strain in the system, $\langle 2P_y^A|H|2P_y^B\rangle$ can be thought as a sum of $\langle 2P_y^{A0}|H|2P_y^{B1}\rangle$, $\langle 2P_y^{A0}|H|2P_y^{B2}\rangle$, and $\langle 2P_y^{A0}|H|2P_y^{B3}\rangle$, since atom type A labeled as "A0" in Figure 2.1 has only three nearest neighbors of atom type B. Since the p_x and p_y orbitals are oriented with some angle (α) with respect to each other due to the structure of the lattice as sketched in Figure 2.2, the individual matrix elements should be calculated by decomposing the orbitals into σ and π components. As an example the matrix element $\langle 2P_y^A|H|2P_y^B\rangle$ can be decomposed as follows:

$$
\begin{aligned}
\langle 2Py^{A0}|H|2Py^{B1}\rangle &= (-V_{pp\sigma}\cos^2\alpha_1 + V_{pp\pi}\sin^2\alpha_1)e^{i\vec{k}\cdot\vec{b}_1}\\
\langle 2Py^{A0}|H|2Py^{B2}\rangle &= (-V_{pp\sigma}\cos^2\alpha_2 + V_{pp\pi}\sin^2\alpha_2)e^{i\vec{k}\cdot\vec{b}_2}\\
\langle 2Py^{A0}|H|2Py^{B3}\rangle &= V_{pp\pi}e^{i\vec{k}\cdot\vec{b}_3} ,
\end{aligned}
\tag{2.13}
$$

where, $V_{pp\sigma}$ and $V_{pp\pi}$ are the interaction parameters between the σ and π orbitals, respectively, and $\vec{b}_1$ and $\vec{b}_2$ are the reciprocal lattice vectors. The general expressions for these interactions can be found in the References [45, 47]. The energy-band diagram of graphene can be viewed via Fig. 2.3, where all the orbitals are considered. We use the parameter set given in Table 2.1 for graphene.
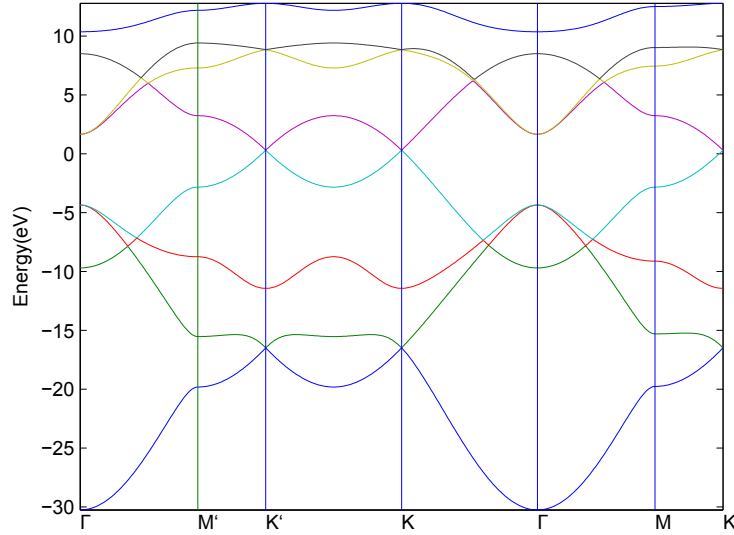
Figure 2.3: The energy-band diagram of graphene when all the orbitals are taken into account.

		Nearest neighbour interaction parameters		Next nearest neighbour interaction parameters	
On-site energies					
ϵ_{2s}	-7.3	V_{ss}	-4.30	V_{ss}^2	-0.18
ϵ_{2p}	0.0	V_{sp}	4.98	V_{sp}^2	0.0
		$V_{pp\sigma}$	6.38	$V_{pp\sigma}^2$	0.35
		$V_{pp\pi}$	-2.66	$V_{pp\pi}^2$	-0.10

Table 2.1: Tight–binding interaction parameters for graphene from Ref. [46]. All values are in eV. ϵ_{2s} and ϵ_{2p} are the self interactions of the s orbital and the p orbitals. V_{ss} and V_{sp} are the interactions of s orbital with the neighboring s orbital, s orbital with the neighboring p orbital, respectively. $V_{pp\sigma}$ and $V_{pp\pi}$ are the interactions of σ and π orbitals with the neighboring σ and π orbitals.

2.3   Calculation of the Fermi Level

In order to determine whether there is a band gap or not, one should be able to calculate the Fermi level. Fermi level is defined as the energy of the topmost filled level in the ground state of the N electron system [50]. For the most general case, we can define a density of levels per unit volume $g(\varepsilon)$ so that the general expression for a variable q can be written as:

$$q = \int d\varepsilon g(\varepsilon) Q(\varepsilon) \tag{2.14}$$

where, q can be defined for two separate cases. If q is the electronic number density n, then $Q(\varepsilon) = f(\varepsilon)$, where $f(\varepsilon)$ is the Fermi Dirac distribution function; if q is the electronic energy density u, then $Q(\varepsilon) = \varepsilon f(\varepsilon)$ [51]. The density of states (or levels) can be easily obtained from the band diagram. However, for this purpose the selection of the k points requires great importance. Rather than calculating the band diagram through a certain route composed of high symmetry points in the reciprocal lattice, one should sample all the k points located in the 1st Brillouin zone. The details about the sampling of the Brillouin zone can be found in Ref. [52]. After the calculation of the band diagram, the DOS (density of states) information can be obtained basically via the consideration of the number of states per unit volume and per unit energy window. With the number of electrons fixed at n and the assumption that the system is at 0 K, the equation 2.14 reduces to :

$$\int_{-\infty}^{Ef} D(\varepsilon) d\varepsilon = n, \tag{2.15}$$

with E_f is the Fermi level, since for 0 K $f(\varepsilon)$ is 1. The integration limits originate from the definition of the Fermi level. This numerical integral can be performed iteratively, and as a result the value for the Fermi level can be estimated, easily. In the band diagrams represented throughout the remaining pages, the Fermi level is set to 0 eV.

2.4   Imperfections in 2D Electronic Systems

The imperfections can be natural parts of solid state systems formed accidentally as well as ingredients introduced in the cold atomic systems intentionally by re-designing the optical lattice or by including several atomic species as in recent experiments [81, 82, 83]. We model both the square lattice and graphene with impurities to observe the changes in their magneto-transport properties under the influence of perpendicular magnetic field. The tight-binding method which is a sufficient tool both for the calculation of the energy spectrum (Hofstadter Butterflies) as a function of magnetic flux ϕ divided by flux quantum ϕ_0 and the Hall conductance still serves well for the systems with impurities. The method-ology is the same as with the one outlined in the previous sections except for some points. First, we define the imperfections as impurity atoms replaced by the original atoms of the basis and vacancies where there exists no atoms. These considerations bring regulations in the hopping parameters. For impurity atoms we simply change the first and the second nearest neighbor hopping parameter of the imperfection, and for the vacancy case they simply become 0. The second difference from the pure cases is that in order to achieve reasonable concentra-tions of impurities by forbidding the system to become an alloy, we enlarge the unitcell. By doing this we are able to work with systems which have arrays of imperfections distributed periodically as imperfection lattices over the remaining lattices. However since the system size is enlarged the calculation cost increases. The size of the Hamiltonian in the magnetic field increases in accordance with the number of atoms considered.

Chapter 3

Electronic Structure of Graphene under Uniaxial Strain

3.1 Tight-Binding Method under the influence of Uniaxial Strain

Since graphene has many independent electronic and mechanical properties which attract the interest of scientists around the world, an investigation into the unified electro-mechanical properties is of great interest. There have been many investigations about the mechanical properties such as elasticity [23] and resistance to elastic deformations both by *ab-initio* calculations and several experiments [21, 48]. In addition, the effects of strain were observed via the Raman Spectra, where with the application of strain the Raman peaks shift and may even be split into sub-peaks [20].

In our calculations, we concentrated on the effects of the uniaxial strain on the band diagram of mono-layer graphene. A simple sketch (Figure 3.1) for this was published in Reference [27]. In order to implement the strain information into the calculations, we first developed an algorithm for the change in the positions of the atoms with respect to the applied strain. This geometric algorithm contains
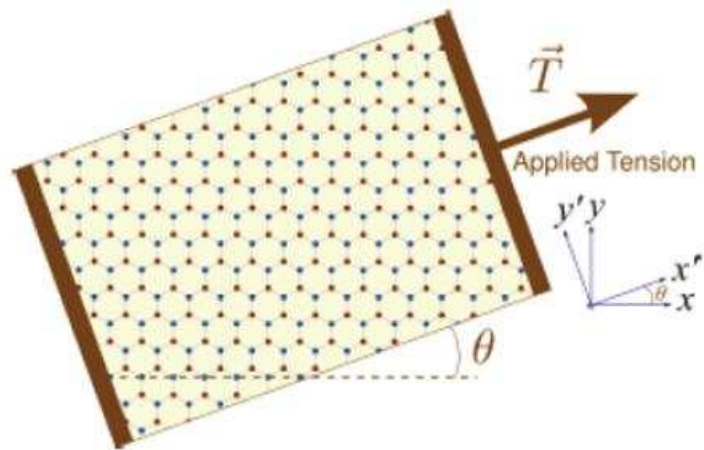
Figure 3.1: The schematic view of strain applied to graphene. The picture is taken from V. M. Pereira, A.H. Castro Neto, N.M. Peres, arXiv: 0811.4396v3 [cond-mat.mtrl-sci], 2009 (Ref. [27]).

the information of the amount of the strain and also the direction through the strain was applied. This re-scaling process basically depends on the change in the vectors under applied strain. The generalization of this fact can be done by considering a general vector $\vec{v_0}$ which is not initially under strain. This vector $\vec{v_0}$ transforms into a new vector $\vec{v}$ with the applied strain by:

$$
\begin{aligned}
\vec{v} &= (\bar{1} + \bar{\varepsilon}) \cdot \vec{v_0} \\
\bar{\varepsilon} &= \epsilon \begin{pmatrix} \cos^2\theta - \sigma\sin^2\theta & (1+\sigma)\cos\theta\sin\theta \\ (1+\sigma)\cos\theta\sin\theta & \sin^2\theta - \sigma\cos^2\theta \end{pmatrix} \quad ,
\end{aligned} \tag{3.1}
$$

where $\bar{1}$ is the unit matrix, $\bar{\varepsilon}$ is the strain tensor, ϵ is the amount of strain which is just a ratio of amount of elongation or compression divided by the initial length (ϵ being positive or negative, respectively), σ is Poisson's ratio, and θ is the angle between the plane of the atoms and the applied strain. All the vectors in the system were subjected to this strain transformation. Within this formulation strain has a first order effect on the bond lengths and the atomic distances. However, when we look at the interaction parameters between the orbitals, we can claim that strain has a second order influence on these parameters. In order to scale, we simply used two transformations, one is an exponential scaling given Ref. [27], and the other is simply square scaling;

$$
V_{pp\sigma}^{new} = V_{pp\sigma} e^{-\beta(\frac{l}{a_0}-1)}, \tag{3.2}
$$

$$
V_{pp\sigma}^{new} = V_{pp\sigma} (\frac{l}{a_0})^2, \tag{3.3}
$$

where l is the new bond length, a_0 is the initial one, β is the scaling parameter and decay rate extracted from the experimental results [49].

3.2   Energy Spectrum of Strained Graphene

When we consider graphene without strain it is easy to calculate the energy bands from tight-binding Hamiltonian. However when there is stress applied to system, the main Hamiltonian should be reconstructed in order to implement this stress information into the calculation. The easiest way to introduce stress to a system is

modifying the Hamiltonian and lattice parameter with strain. Strain is a unitless measure of stress, it is the amount of elongation or compression divided by the initial length. It changes sign due to being an elongation or compression strain. There are several consequences of uniaxial strain applied to a (2D) system:

- Due to the strain, all the vectoral quantities in the real space, including the primitive lattice vectors, the distance between the atoms should be re-arranged by the strain tensor as shown in Eq. 3.1. The atoms change their initial positions, and the bond-distances change as a result of that. Since the strain uniform and uniaxial, and we are studying the bulk electronic properties, the lattice vectors should also be modified to expand the calculations among the infinite surface.

- As a result of changes in real space, all the vectors and distances in the reciprocal space should be modified, too. Similarly, the reciprocal lattice vectors, the coordinates of high symmetry points are all altered due to strain.

- Due to the contraction or elongation in the inter-atomic distances, the interaction parameter must be subject to a scaling algorithm. The main scaling types are already given in Eq. 3.2 and Eq. 3.3.

- Due to the change of the positions of the atoms, the orientations of the atomic orbitals with respect to each other are also modified. The angles between the orbitals should be subjected to modifications as a function of strain.

In our analysis, we used the tight-binding method with the first and the also with the second order interactions. We also tested both the square scaling the exponential scaling of the orbital interaction parameter. We also considered the isotropic case, where the orbital interaction parameter are the same for all bond directions. In addition to that, we also studied the anisotropic case in which the orbital interaction parameter are different among the different bond directions.

The main calculations for this chapter involves the sets of parameter itemized below:

- Several strain values; "ϵ" the amount of strain percentage is scanned for 0, 5, 10, 15, 20, 25, 30 and 35 %.

- Different Poisson's ratios "σ" were used: -0.300, -0.250, -0.200, -0.180, -0.170, -0.165, -0.160, -0.150, -0.140, -0.130, -0.120, -0.110, -0.100, -0.05, 0, and 0.300, 0.250, 0.200, 0.180, 0.170, 0.165, 0.160, 0.150, 0.140, 0.130, 0.120, 0.110, 0.100, 0.05.

- And also several angles through which strain is applied to the plane of graphene: 0, $\pi/2$, $\pi/3$, $\pi/6$, $\pi/12$, $9\pi/180$, $17\pi/180$, $23\pi/180$.

3.2.1 Energy-Band Structure of Strained Graphene

As it is mentioned in section 3.1, we introduced uniaxial strain to the system. According to this information, all the vectoral quantities are transformed. When plotting the band diagram we also modified the coordinates of the high symmetry points and the distance between them which comes automatically as a consequence of the change in the coordinates. Secondly, due to change in the inter-atomic distances, the interaction parameter are also rescaled. There are two main scaling methods, one is exponential scaling, the other one is square scaling for which the explicit representations were given in Equations 3.2 and 3.3. We tested both of them. And also we tried two different conditions, one the scaling functions differ for each directions by the change of one variable β, and for the second condition we considered it to be the same for the all directions which corresponds to the isotropic case. In Ref. [1] β is reported to be 3, 3.14, and 4.

The angle θ which represents the angle of strain direction to the graphene surface, corresponds to 0 degrees for the armchair direction and the horizontal axis coincides with the armchair direction. We scanned the reported values for θ, the symmetric angles for graphene as well as some values for the chiral angles.

For the case of choice for the value of the Poisson's ratio σ, we performed a wide range of calculation between the values -0.300 and 0.300 since there is no strict information about the ratio for mono-layer graphene reported in the literature. The most common value for σ is 0.165 [84] but it is stated that this is the measured value for graphite [1, 85]. However, many researchers are using this value in their calculations. Also there is another reported range for graphene's Poisson's ratio which is said to be lie in between 0.10 and 0.14 [86]. In order to convince ourselves, we tested a wide range for the parameter.

Since we try to obtain a band gap opening as a result of strain, we test graphene for the strain amounts between 0 to 35 % through which the graphene is able to stay unbuckled.

The last point we concentrated on is to preserve the lattice structure through applying strain in the chiral angles, since the lattice may not be defined anymore. To check this condition, we defined chiral and translational vectors corresponding to the desired values for angles in other words for the pairs (m, n) commonly used by researchers working on nanotubes. For a net to define a lattice, these vectors should be perpendicular to each other. With the effect of strain these vectors change as well, but they should still be perpendicular to each other. We have written an algorithm which keeps the track of this information. It came out that in none of our calculations we are losing the lattice.

For the basic angles 0, 30, 60 and 90 degrees we obtain the following results: There is a band gap between 10 and 25% of strains for 30 and 60 degrees, as shown in Fig. 3.2. When the amount of strain is increased to 30%, the conduction and valance bands intersect the Fermi level which can be viewed via Fig. 3.3 . And this behavior is similar for all the Poisson's ratio in the neighborhood of 0.165 and -0.165 when 1st nearest neighbors are considered and the scaling scheme chosen to be as exponential. When we insert the 2nd nearest neighbors into the calculations there is no systematic behavior of a band gap opening and evolving with the increase of strain applied. Instead there is a random 0.5 eV gap opening due to the orientations of the bands for 30 degrees and for the 15% strain. For square scaling in both the 1st and the 2nd nearest neighbors interactions there is
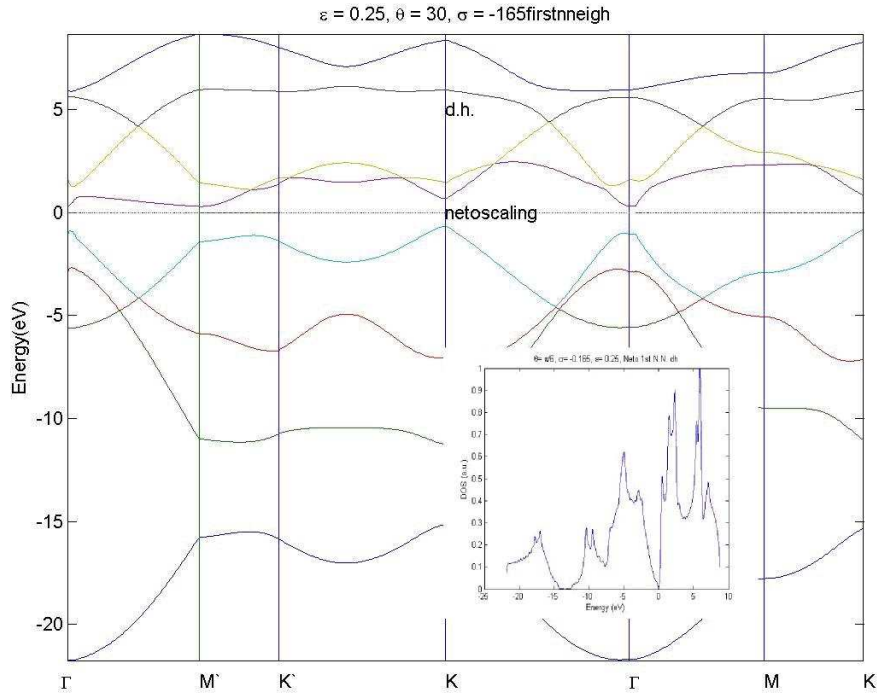
Figure 3.2: Energy-band diagram of graphene with 1st nearest neighbors tight-binding method under 25% strain applied with $\theta = 30^0$ with Poisson's ratio $\sigma = -0.165$ and the decay rates were scaled with exponential scaling to be the same for all directions.

no opening, either.

We also examined $9\pi/180$, $17\pi/180$, $23\pi/180$ degrees. For the 1st nearest neighbor interactions in the exponential scaling scheme, there is a band gap of almost $1.0\ eV$ up to 30% strain. At 30% the gap closes with the conduction band intersecting the Fermi Level. However, when the 2nd nearest neighbors calculated both with exponential and square scaling there is no band gap. These results are displayed in Fig. 3.4 through Fig. 3.17 on following pages.
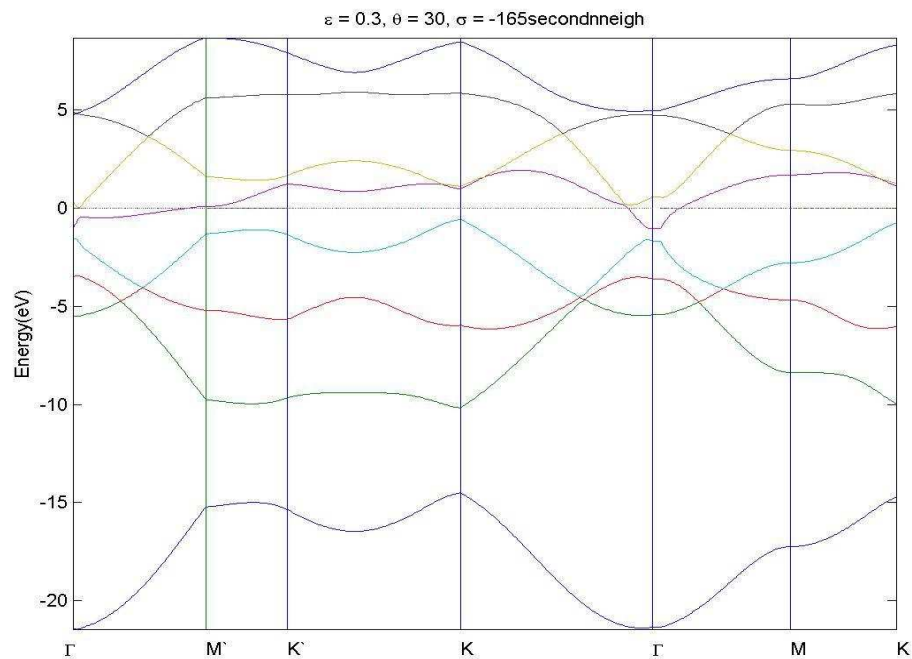
Figure 3.3: Energy-band diagram of graphene with 1st and the 2nd nearest neighbors tight-binding method under 30% strain applied with $\theta = 30^0$ with Poisson's ratio $\sigma = -0.165$ and the decay rates were scaled with exponential scaling to be the same for all directions.
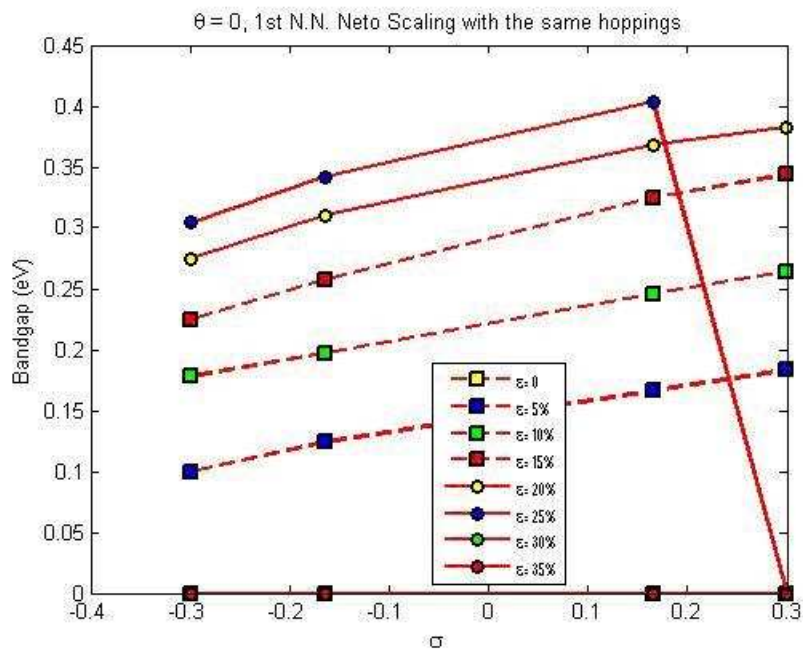
Figure 3.4: Poisson's ratio versus energy-band gap for $\theta = 0^0$, with exponential scaling and same hopping constants (decay rates) for all directions for the 1st nearest neighbors.

Although it has always been a dream for researchers to apply band gap engineering on graphene via tuning the uniaxial strain, it seems clearly that uniaxial strain is not able to generate a band gap opening in the monolayer graphene, unlike the case in bilayer graphene. With the scanning of the parameters like the amount and geometrical orientation of strain, and Poisson's ratio in the proper limits, we conclude that monolayer graphene is not a suitable candidate for the tuning of the gap energy via the application of uniaxial strain. However, under the strain, monolayer graphene remains semi-metallic, and the changes occur in band diagram can lead to exotic results in its electron transport properties.
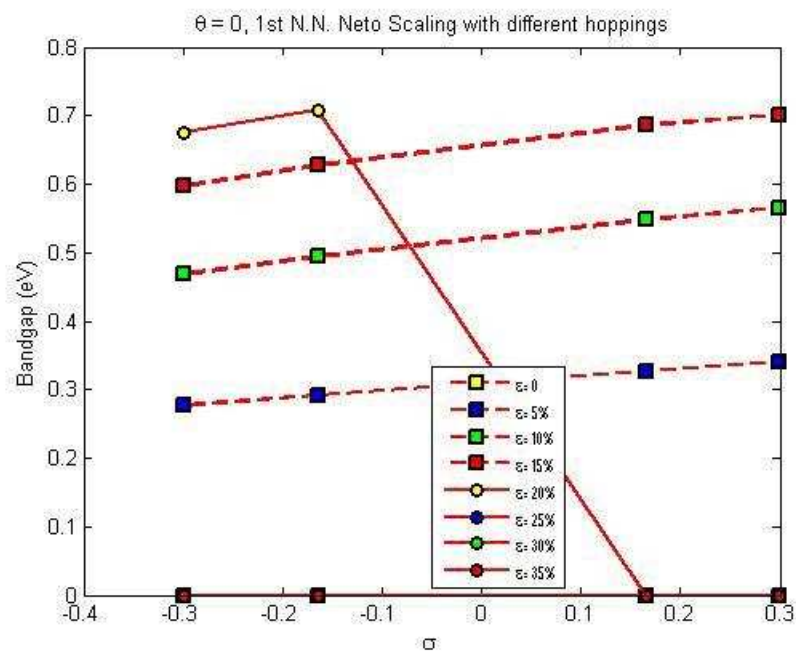
Figure 3.5: Poisson's ratio versus energy-band gap for $\theta = 0^0$, with exponential scaling and different hopping constants (decay rates) for all directions for the 1st nearest neighbors.
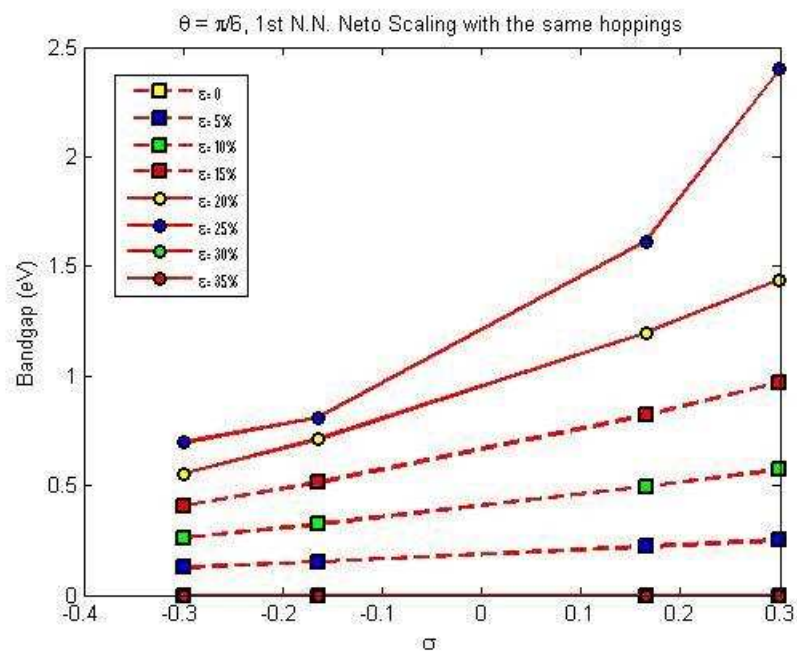
Figure 3.6: Poisson's ratio versus energy-band gap for $\theta = 30^0$, with exponential scaling and same hopping constants (decay rates) for all directions for the 1st nearest neighbors.
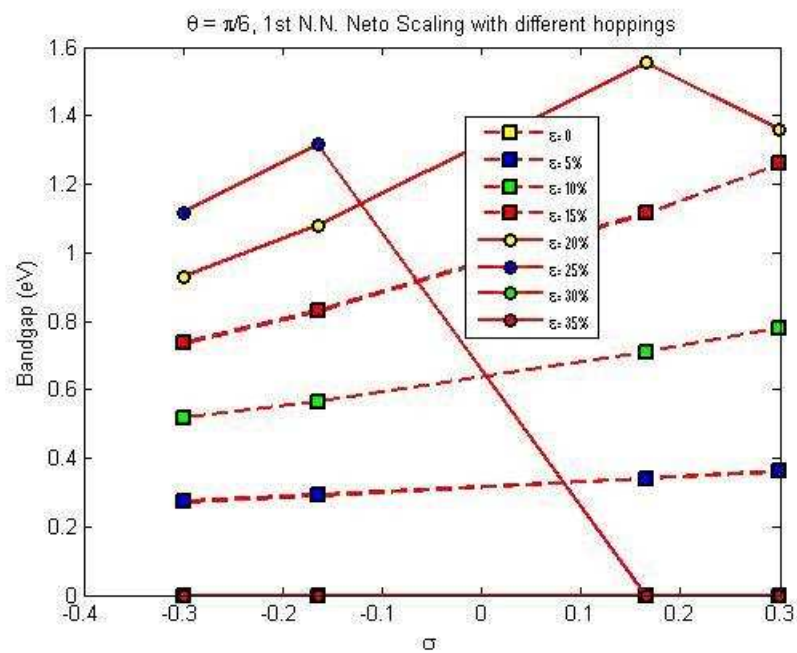
Figure 3.7: Poisson's ratio versus energy-band gap for $\theta = 30^0$, with exponential scaling and different hopping constants (decay rates) for all directions for the 1st nearest neighbors.
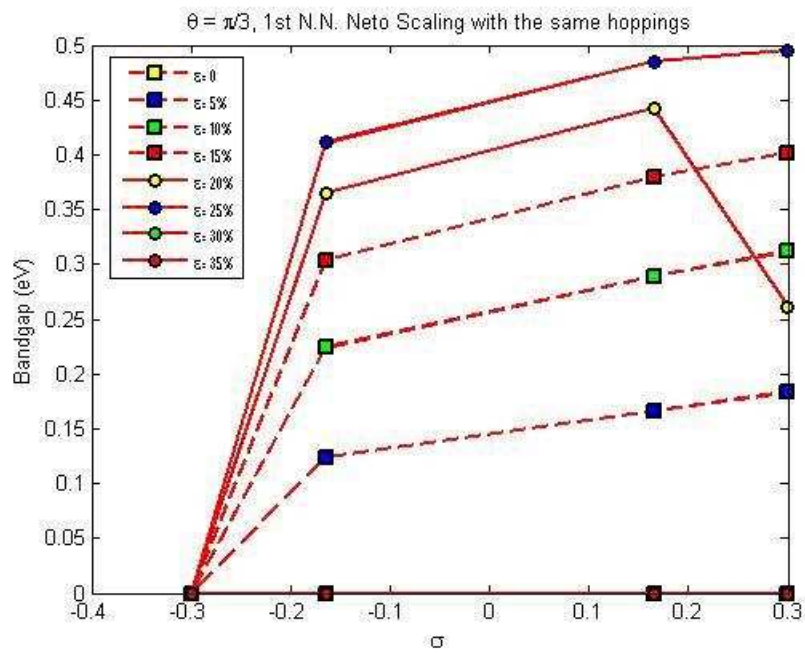
Figure 3.8: Poisson's ratio versus energy-band gap for $\theta = 60^0$, with exponential scaling and same hopping constants (decay rates) for all directions for the 1st nearest neighbors.
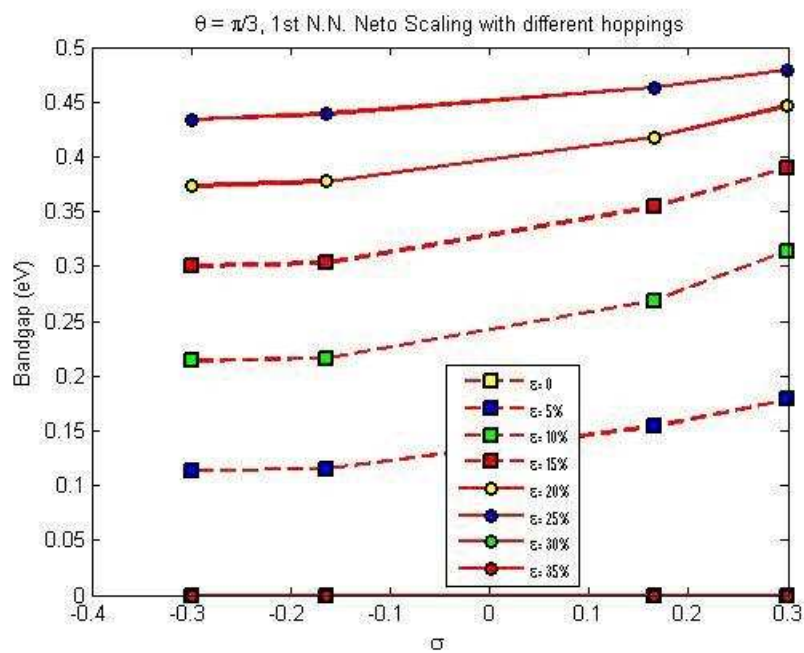
Figure 3.9: Poisson's ratio versus energy-band gap for $\theta = 60^0$, with exponential scaling and different hopping constants (decay rates) for all directions for the 1st nearest neighbors.
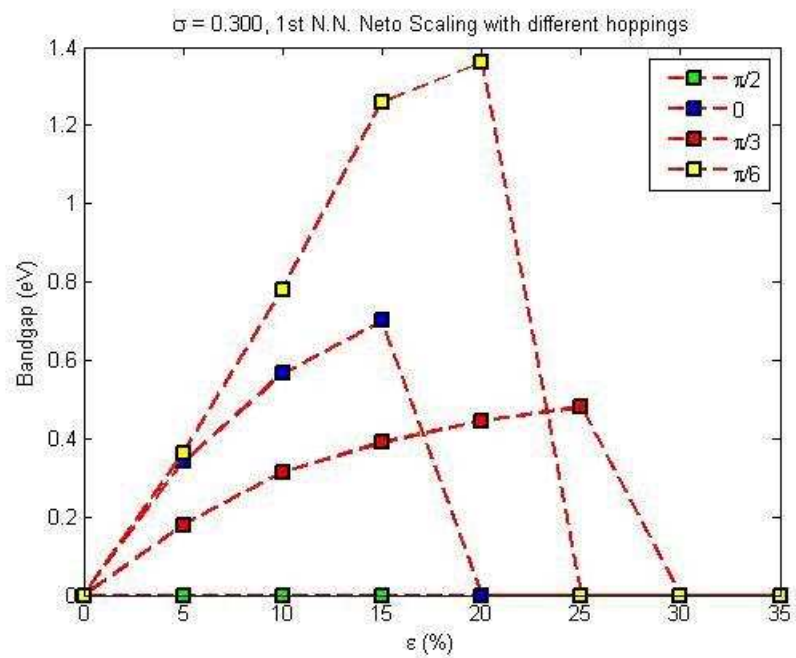
Figure 3.10: Strain versus energy-band gap for $\sigma = 0.300$, with exponential scaling and different hopping constants (decay rates) for all directions for the 1st nearest neighbors tabulated for several angles.
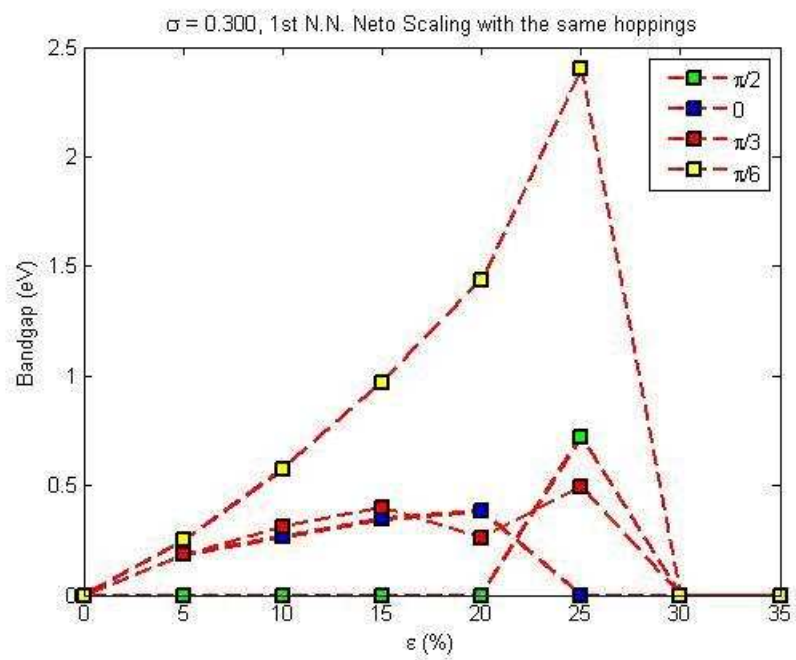
Figure 3.11: Strain versus energy-band gap for $\sigma = 0.300$, with exponential scaling and same hopping constants (decay rates) for all directions for the 1st nearest neighbors tabulated for several angles.
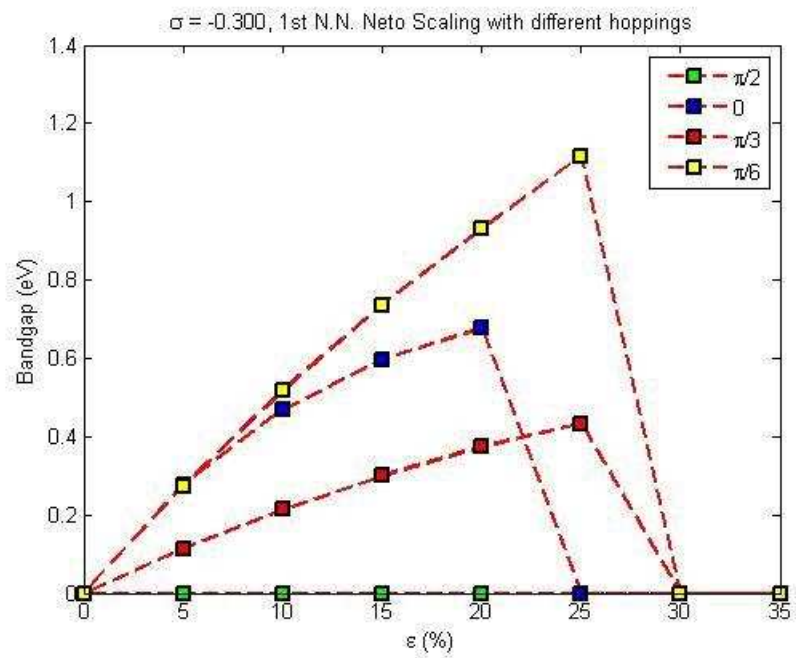
Figure 3.12: Strain versus energy-band gap for $\sigma = -0.300$, with exponential scaling and different hopping constants (decay rates) for all directions for the 1st nearest neighbors tabulated for several angles.
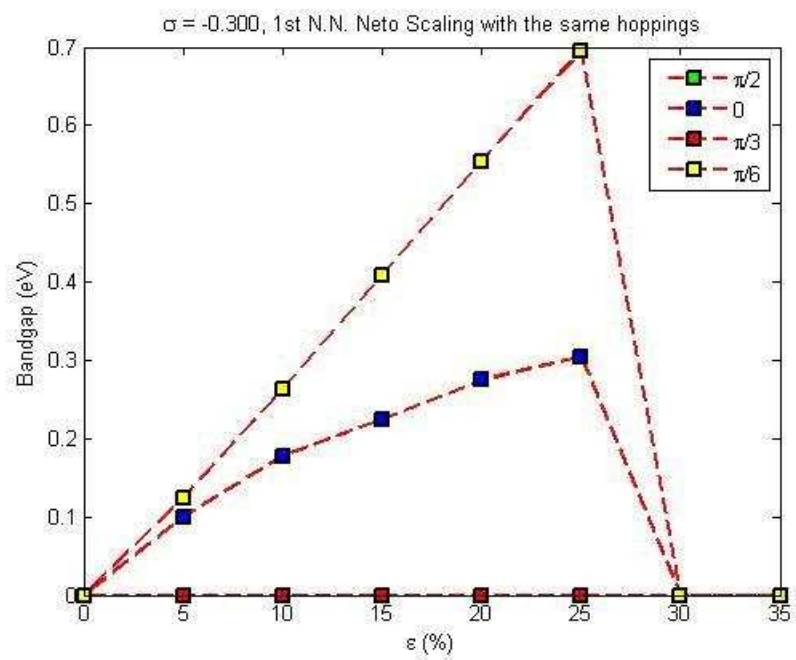
Figure 3.13: Strain versus energy-band gap for $\sigma = -0.300$, with exponential scaling and same hopping constants (decay rates) for all directions for the 1st nearest neighbors tabulated for several angles.
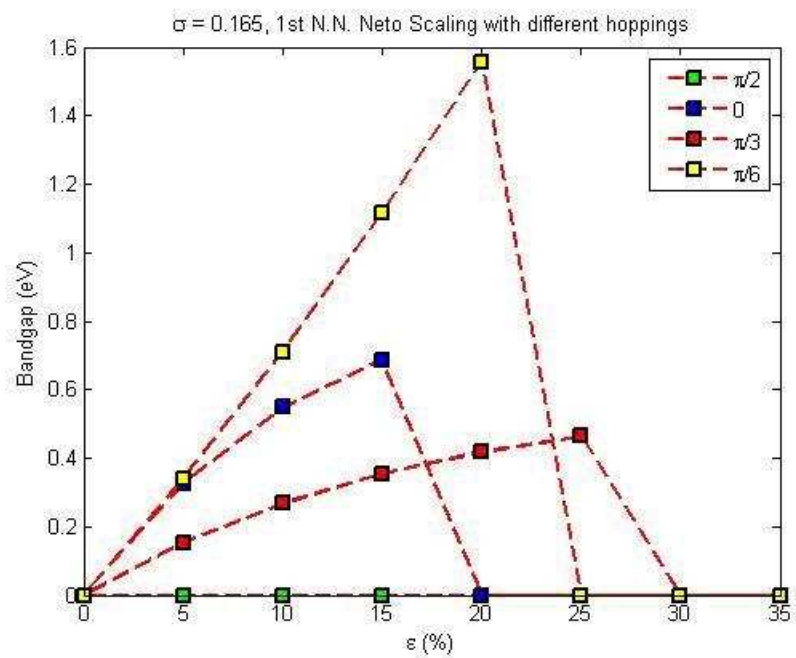
Figure 3.14: Strain versus energy-band gap for $\sigma = 0.165$, with exponential scaling and different hopping constants (decay rates) for all directions for the 1st nearest neighbors tabulated for several angles.
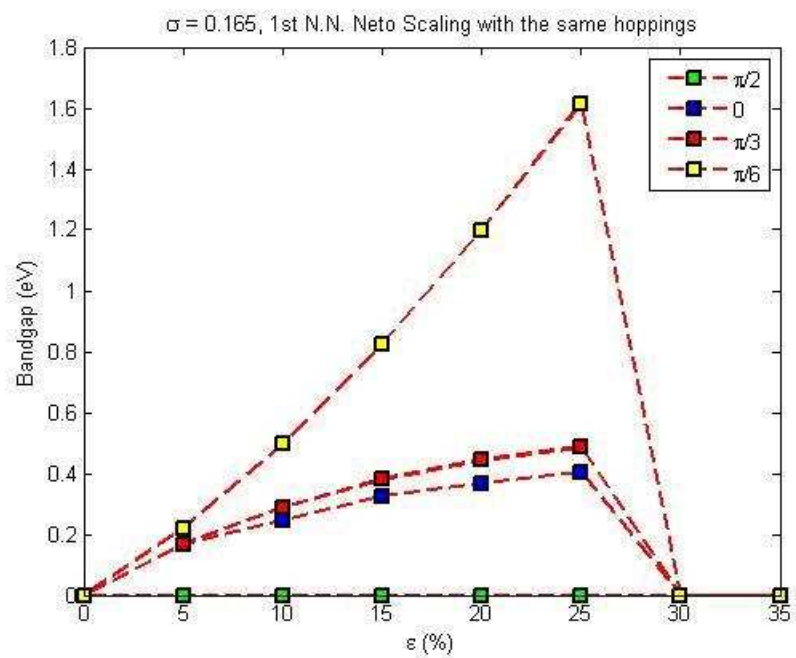
Figure 3.15: Strain versus energy-band gap for $\sigma = 0.165$, with exponential scaling and same hopping constants (decay rates) for all directions for the 1st nearest neighbors tabulated for several angles.
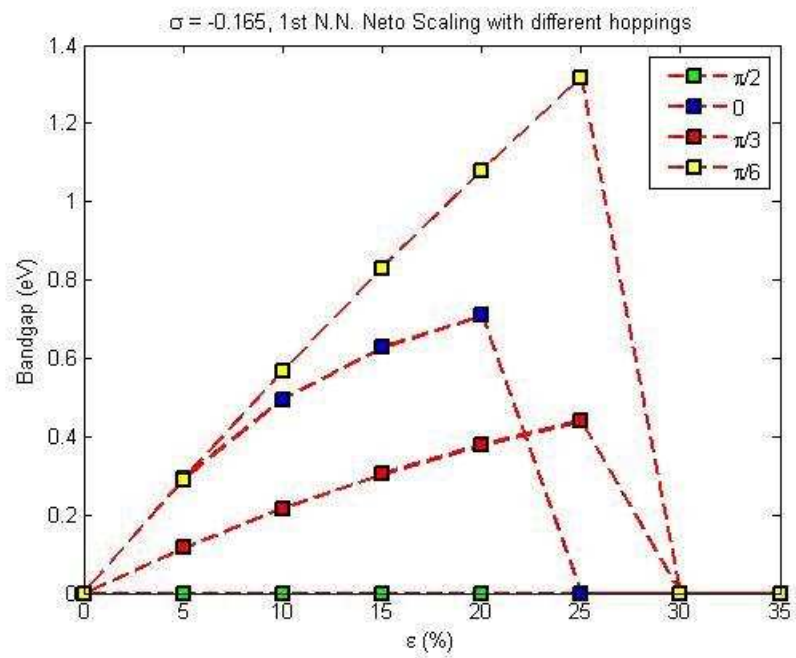
Figure 3.16: Strain versus energy-band gap for $\sigma = -0.165$, with exponential scaling and different hopping constants (decay rates) for all directions for the 1st nearest neighbors tabulated for several angles.
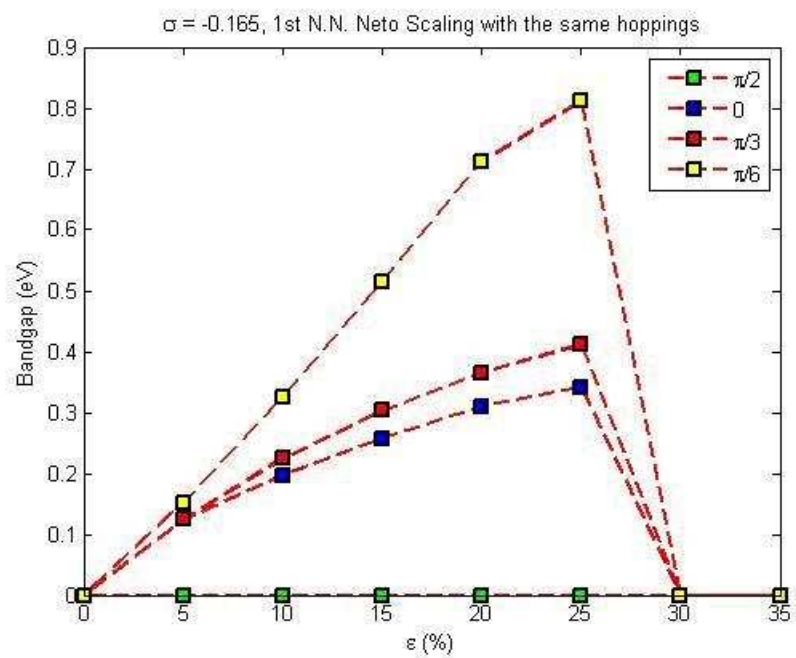
Figure 3.17: Strain versus energy-band gap for $\sigma = -0.165$, with exponential scaling and same hopping constants (decay rates) for all directions for the 1st nearest neighbors tabulated for several angles.

Chapter 4

Hofstadter Butterflies of Square Lattice and Defective Square Lattice

4.1 Energy Spectrum Under the Influence of Perpendicular Magnetic Field

The Tight-binding method also acts as a sufficient and viable tool for monitoring the electronic behavior of the systems under the influence of perpendicular magnetic field. The energy spectrum of a 2D system displays a variety of properties when subjected to magnetic field. The most famous work for the energy spectrum of 2D electrons in a square lattice was performed by D. R. Hofstadter in 1976 [36]. He used the tight-binding method in order to calculate the energy spectrum. In his work he modified the momentum through the *Peierls Substitution* [53], and as a result of that the wavefunctions are also modified in terms of new magnetic field oriented phases. The magnetic field brings nothing new to the usual tight binding method but it introduces interactions between the atoms in the magnetic unit cell, not only through the unit cell. In the subsections below, both the pure square lattice and the defected square lattice are subjected to a perpendicular

36
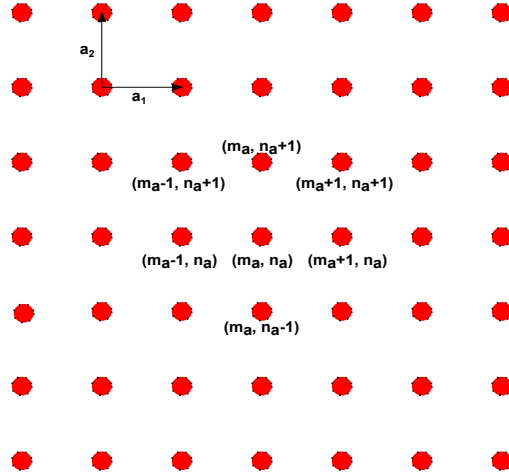
Figure 4.1: Square Lattice with 1 atom in its basis. The lattice vectors are given by $a_1 = a\vec{x}$ and $a_2 = a\vec{y}$. Each atom is identified by (m, n) pair of indices.

magnetic field. The energy spectrum of both display intriguing unique butterfly like structures so called the *Hofstadter Butterflies*.

4.1.1 Square Lattice with a Single Atom in the Basis

We start by reviewing the pure case which was first discussed by Hofstadter [36]. Within the tight-binding approximation, the single band Hamiltonian for the Schrödinger equation of a square lattice with lattice constant a, for one atom in the unit cell is equal to:

$$H = t\{e^{-ik_x a} + e^{ik_x a} + e^{-ik_y a} + e^{ik_y a}\}, \tag{4.1}$$

where the exponential factors arise due to the interactions of the first nearest neighbors. The coefficient t is the hopping (orbital interaction) term which has units of energy. Henceforth, we will express all energies in units of t, effectively setting $t = 1$. The geometric configuration can be viewed from Fig. 4.1 where one can observe that the atom with label (m_a, n_a) interacts with the atoms of labels (m_a+1, n_a), (m_a-1, n_a), (m_a, n_a+1), and (m_a, n_a-1). The corresponding lattice vectors $\vec{a_1}$ and $\vec{a_2}$ satisfy the equation $\vec{R}_{(m_a,n_a)} = m_a\vec{a_1} + n_a\vec{a_2}$, where $\vec{R}_{(m_a,n_a)}$ is
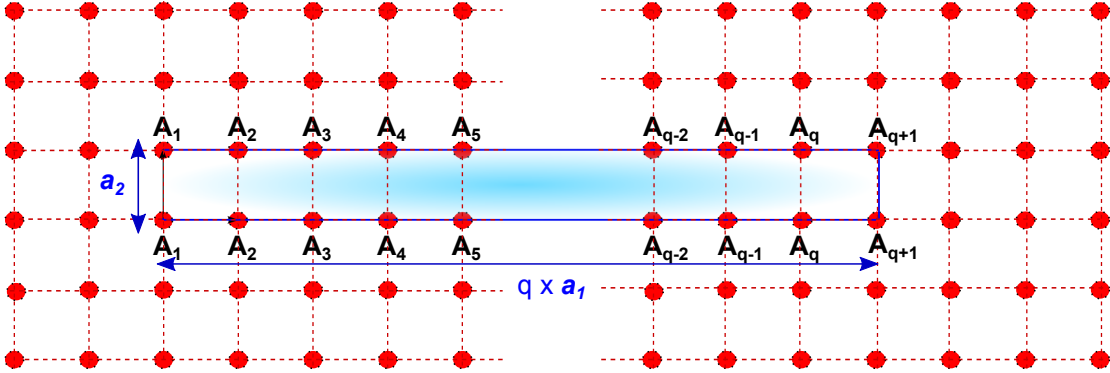
Figure 4.2: The magnetic unit cell of the square lattice where q atoms are connected.

the position vector of the atom labelled by (m_a, n_a). When we introduce the magnetic field into the system, we use the *Peierls Substitution* which shifts the momentum by the vector potential of the magnetic field:

$$\hbar\mathbf{k} \rightarrow \hbar\mathbf{k} - \frac{e\vec{\mathbf{A}}}{c}.$$

For a perpendicular magnetic field, we choose the Landau gauge which gives a vector potential in the y direction as a function of x, $\vec{\mathbf{A}} = (0, Bx, 0)$. With this choice of gauge, only the hopping strengths in the y direction gain additional phase factors $e^{-2\pi i \frac{e}{\hbar} \int \vec{\mathbf{A}} \cdot \vec{dl}}$, where the integral is evaluated along the line connecting the two atoms. With the addition of the phase factors originating from the magnetic field, we have a new Hamiltonian:

$$
\begin{aligned}
H' &= t\{e^{-ik_x a} + e^{ik_x a} \\
&+ e^{-ik_y a} e^{2i\pi m_a \frac{\phi}{\phi_0}} + e^{ik_y a} e^{-2i\pi m_a \frac{\phi}{\phi_0}}\},
\end{aligned}
$$

with $\phi = Ba^2$, magnetic field times the area of the unit cell, and ϕ_0 is the flux quanta h/e. Now, the Schrödinger equation becomes:

$$
\begin{aligned}
H'\psi &= t\{\psi(m_a - 1, n_a) + \psi(m_a + 1, n_a) \\
&+ \psi(m_a, n_a - 1)e^{2i\pi m_a \frac{\phi}{\phi_0}} \\
&+ \psi(m_a, n_a + 1)e^{-2i\pi m_a \frac{\phi}{\phi_0}} \\
&= \varepsilon\psi(m_a, n_a).
\end{aligned}
$$
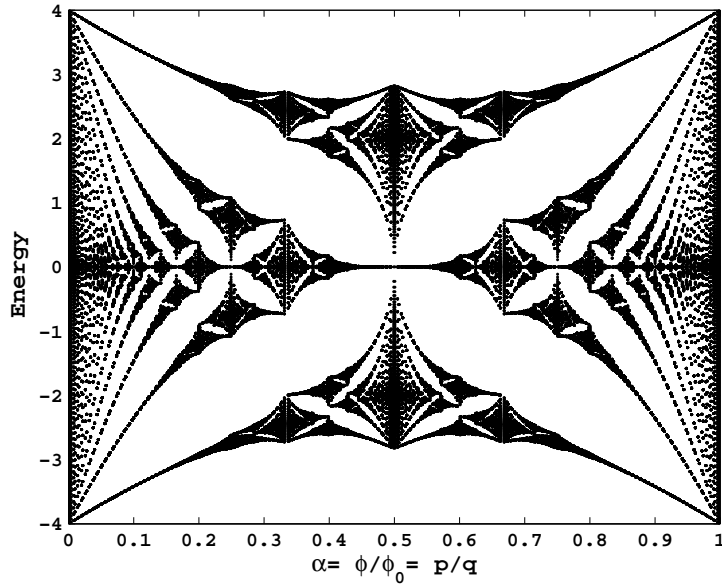
Figure 4.3: The Hofstadter Butterfly spectrum for square lattice with $q = 501$, and $t = 1.0$ [43]

If we make the substitution $\psi(m_a, n_a) = \varphi(m_a)e^{ik_y a n_a}$, we get a new equation known as *Harper's equation* [54]:

$$
\begin{aligned}
\varepsilon\varphi(m_a) &= t\varphi(m_a - 1) + t\varphi(m_a + 1) \\
&+ 2t\varphi(m_a)cos(2\pi m_a\frac{\phi}{\phi_0} - k_y a)
\end{aligned}
\tag{4.2}
$$

We set the ratio between the amount of flux through a plaquette and the flux quanta to be equal to α, and let this α to be represented as a fraction of two co-prime integers such that $\alpha = \phi/\phi_0 = p/q$. The values of m_a ranges from 1 to q as a result of q atoms being connected to each other in the magnetic unit cell. This magnetic unit cell for square lattice can be visualized via Fig. 4.2, where the magnetic unitcell vectors are expressed in terms of the unitcell vectors and the integer q.

However, when we try to solve this recursive equation for $\varphi(1)$, we have $\varphi(0)$

term on the right-hand side. Similarly, as we set m_a to be $m_a = q$, we have $\varphi(q+1)$ term on the right hand side. In order to obtain solutions to this equation, we have to stay within the boundaries we decided for m_a which spans the values from 1 to q. For this purpose, we apply the *Bloch* condition which can be expressed as; $\varphi(m+q) = \varphi(m)e^{iqk_x a}$. By use of this boundary condition, we end up with a matrix equation. This supercell matrix is called the A_m matrix;

$$
\begin{bmatrix}
\varphi_1 \\
\varphi_2 \\
\vdots \\
\varphi_{q-1} \\
\varphi_q
\end{bmatrix}
=
\begin{bmatrix}
2t\cos(2\pi\frac{\phi}{\phi_0}) & t & 0 & \cdots & te^{-iqk_x a} \\
t & 2t\cos(4\pi\frac{\phi}{\phi_0}) & t & \cdots & 0 \\
0 & t & 2t\cos(6\pi\frac{\phi}{\phi_0}) & t & \vdots \\
\vdots & \vdots & \ddots & \ddots & t \\
te^{iqk_x a} & 0 & \cdots & t & 2t\cos(2q\pi\frac{\phi}{\phi_0})
\end{bmatrix}
\begin{bmatrix}
\varphi_1 \\
\varphi_2 \\
\vdots \\
\varphi_{q-1} \\
\varphi_q
\end{bmatrix},
$$

$$(4.3)$$

and the eigenvalues of this matrix has the famous butterfly shape given in Fig. 4.3.

4.2 Defective Square Lattice

We use the tight-binding method for the square lattice where the 1st and the 2nd nearest neighbor interactions are both included in order to model the (2D) electronic system in a magnetic field, with impurities or vacancies. The perpendicular magnetic field applied to the (2D) system brings out additional phase factors [53] to the usual tight-binding terms. In addition, the magnetic field changes the periodicity of the system leading to a larger "magnetic unit cell". Once the tight-binding system is revised with the magnetic field, we end up with a new magnetic field tight-binding Hamiltonian, which is described by the A_m matrix [36]. Its eigenvalues and the eigenvectors give the desired energies and wavefunctions, respectively.

For a pure system, square lattice with a single atom basis works well, and it produced many results about the Hofstadter Butterflies and the Hall conductances [77, 80, 87]. There are also studies [88] on the effect of 2nd nearest neighbor
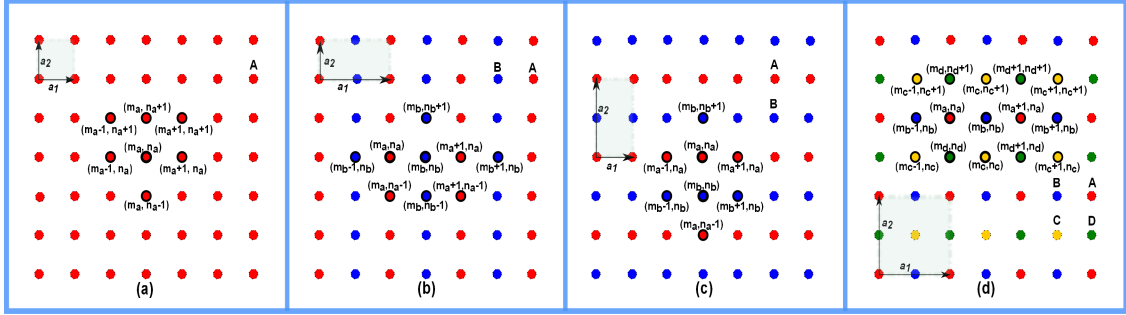
Figure 4.4: The unit cells for the configurations: **(a)** One atom in the basis. The corresponding lattice vectors are $\vec{a_1}=\hat{x}a$ and $\vec{a_2}=\hat{y}a$, where $a=1$ is the lattice constant. **(b)** *Rectangular unit cell aligned horizontally*: Two atoms in the basis with an asymmetric choice of unit cell. The corresponding lattice vectors are $\vec{a_1}=2a\hat{x}$ and $\vec{a_2}=a\hat{y}$. **(c)** *Rectangular unit cell aligned vertically*: Asymmetric unit cell choice of square lattice which contains again two atoms but with different unit vectors. The corresponding lattice vectors are $\vec{a_1}=\hat{x}a$ and $\vec{a_2}=\hat{y}2a$. **(d)** Square lattice which contains four different atoms in the unit cell. The lattice vectors are $\vec{a_1}=\hat{x}2a$ and $\vec{a_2}=\hat{y}2a$ [43]

interactions which breaks the bipartite symmetry, and as a result of that the Hofstadter Butterfly is no longer symmetric around $E=0$.

For the impurity and vacancy cases the tight-binding method with single atom in the basis is not enough to realistically model the case. One has to have at least two atoms in order to treat one of them as an impurity or vacancy. However for this scenario, we get a 50% of impurity or vacancy in terms of concentration which is similar to a super lattice rather than impurity. In order to overcome this obstacle, one should choose the unit cell as large as possible. In this thesis, we propose a method which enables direct access to the A_m matrix. This matrix is obtained by the tight-binding method under the perpendicular magnetic field, which can be written in the form of the well-known *Harper's* equation [54]. We show how to generate the A_m matrix efficiently for enlarged supercells of square lattice. In order to establish the method for enlarged systems which include a point defect with reasonable density, we present the cases starting from a small single atom unit cell to an enlarged unit cell including nine atoms. Although we are discussing the specific case for the square lattice, our methods are applicable

to all kinds of lattice geometries.

4.2.1   Enlarged Unit Cell

Assume that, we have a square lattice with 2 atoms in its basis, labelled by **A** and **B** are arranged as shown in Fig. 4.4(b). For this case, different from Eq. (4.1), we have the matrix representation for the Hamiltonian:

$$H = \begin{bmatrix} H^{AA} & H^{AB} \\ H^{BA} & H^{BB} \end{bmatrix} \quad ,$$

These independent matrices have the information for the orbital interactions between the types of atom located at the nearest neighboring sites. For example, H^{AA} has three terms; the self interaction term of type A atom, and plus two terms for the interaction of neighboring type A atoms. Due to the addition of the magnetic field, there will be phase factors for only those interactions which are aligned with the vector potential in the y direction. We can expand the Hamiltonian with the phase factors arising from the magnetic field under these circumstances;

$$\begin{aligned} H^{AA} &= t\{e^{ik_y a}e^{-i\theta} + e^{-ik_y a}e^{i\theta}\} + \varepsilon_{2p}, \\ H^{AB} &= t\{e^{ik_x a} + e^{-ik_x a}\}, \end{aligned}$$

where ε_{2p} is the self interaction term of p_z orbitals. Since the Hamiltonian must be a *Hermitian* matrix, H^{BA} is the complex conjugate of H^{AB}. The extra exponential terms in H^{AA} can be defined as follows;

$$\begin{aligned} e^{i\theta} &= e^{-2\pi i \int_{R_{m_a,n_a-1}}^{R_{m\vec{a},n_a}} \vec{\mathbf{A}} \cdot \vec{dl}}, \\ &= e^{2\pi i (2a^2 B m_a)\frac{e}{\hbar}} = e^{2\pi i \frac{\phi}{\phi_0} m_a}, \end{aligned}$$

Due to the change in the area of the unit cell, now we have $\phi = 2Ba^2$, which is doubled compared to the square lattice with one atom in its unit cell. Another difference from the previous calculation is, we have a column vector for the $\varphi(m_a)$ which we prefer to denote as

$$\Psi(m) = \begin{bmatrix} \varphi(m_a) \\ \varphi(m_b) \end{bmatrix}$$

According to these considerations, the Eq. (4.2) is now a matrix equation:

$$\Psi(m) = U_m \Psi(m) + W_m \Psi(m-1) + V_m \Psi(m+1), \tag{4.4}$$

with U_m, W_m, and V_m are all matrices, instead of single coefficients in the pure case. Explicitly,

$$U_m = \begin{bmatrix} 2t\cos(2\pi\alpha m - k_y a) & t \\ t & 2t\cos(2\pi\alpha(m+1/2) - k_y a) \end{bmatrix},$$

$$W_m = \begin{bmatrix} 0 & t \\ 0 & 0 \end{bmatrix}, V_m = \begin{bmatrix} 0 & 0 \\ t & 0 \end{bmatrix}$$

We apply the *Bloch* condition to the wavefunctions, and as a result, we have the A_m matrix as follows:

$$A_m = \begin{bmatrix} U_1 & V_1 & 0 & 0 & \cdots & 0 & W_1^* \\ W_2 & U_2 & V_2 & 0 & 0 & \cdots & 0 \\ 0 & W_3 & U_3 & V_3 & 0 & \cdots & 0 \\ \vdots & \vdots & \ddots & \ddots & \ddots & \ddots & \vdots \\ V_q^* & 0 & 0 & \cdots & 0 & W_q & U_q \end{bmatrix}. \tag{4.5}$$

Rectangular unit cell aligned horizontally

For a system of atoms arranged as in Fig. 4.4(b), it is somehow easy to perform this calculation, however we are offering a simple and compact method in order to construct the A_m matrix just from the geometry. Therefore, it is enough to calculate the phase factors due to the perpendicular magnetic field on top of the simple tight-binding methodology. As pointed out previously, only the hopping in y-direction is modified by the magnetic field. Since we have two types of atoms in the unit cell, and the periodicity of the phase factors in the m direction is q, the dimensions of the A_m matrix is $2q \times 2q$. We start by generating the A_m matrix as a $2q \times 2q$ null matrix. The first element $(1,1)$ of the matrix A_m will be due to the interaction of A atom labelled by $(m_a = 1)$ with the A atoms with the same label $(m_a = 1)$. As there are two A type atoms with labels $(m_a = 1)$ in the first nearest neighborhood there is a term $2t\cos(2\pi\frac{\phi}{\phi_0} - k_y a)$ in the $A_m(1,1)$. Our

next term will be $A_m(1, 2)$, which have the value t due to the interaction between atom type A labelled with $(m_a = 1)$ and atom type B labelled by $(m_b = 1)$. The element of matrix A_m with index $(1, 3)$ is equal to 0, since we do not consider such a long range interaction. Similarly, $A_m(1, 4)$ is equal to 0, as well as the rest of this row. In order to include the 2nd nearest neighbors or even higher order hopping, we would have to calculate longer range tight-binding terms. In the next row, the same procedure is repeated but for this case we are concentrating on the interactions between the atom $B(m_b = 1)$ and $A(m_a = 1)$, $B(m_b = 1)$, $A(m_a + 1) = A(2)$, $B(m_b + 1) = B(2)$. So we have

$$A_m(2, 1) = t, A_m(2, 2) = 2t\cos(2\pi\frac{\phi}{\phi_0}(1 + 1/2) - k_y a),$$

$$A_m(2, 3) = t, A_m(2, 4) = 0.$$

Again this row spans all the values between $m = 1, 2, ..., q$. The rest of the rows can be calculated by carrying out the same steps from m_a to $m_a + q$, and we end up with:

$$A_m = \begin{bmatrix} 2t\cos(2\pi\frac{\phi}{\phi_0} - k_y a) & t & 0 & 0 & 0 & \cdots & 0 \\ t & 2t\cos(2\pi\frac{\phi}{\phi_0}(1 + 1/2) - k_y a) & t & 0 & 0 & \cdots & 0 \\ 0 & t & 2t\cos(4\pi\frac{\phi}{\phi_0} - k_y a) & t & 0 & \cdots & 0 \\ \vdots & \vdots & & \ddots & \ddots & \ddots & \vdots \\ 0 & 0 & 0 & \cdots & 0 & t & 2t\cos(2\pi\frac{\phi}{\phi_0}(q + 1/2) - k_y a) \end{bmatrix}.$$

(4.6)

Now we have to apply the *Bloch* condition to the wavefunctions $\psi(m_a + q - 1) = e^{ik_x qa}\psi(m_a - 1)$, through which we determine the topmost right-hand side and the bottommost left-hand side of the matrix A_m. Let us start with the bottommost entries $A_m(2q - 1, 1)$, $A_m(2q - 1, 2)$, $A_m(2q, 1)$, and $A_m(2q, 2)$, which represent the interactions of $A(m_a + q - 1)$ with $A(m_a)$ and $B(m_b)$; and $B(m_b + q - 1)$ with $A(m_a)$ and $B(m_b)$, since we have to have q elements in each row and column. Thus,

$$A_m(2q - 1, 1) = 0 \cdot e^{ik_x qa}, A_m(2q - 1, 2) = 0 \cdot e^{ik_x qa},$$

$$A_m(2q, 1) = t.e^{ik_x qa}, A_m(2q, 2) = 0 \cdot e^{ik_x qa}.$$

The eigenvalues of the A_m give the energy as function of flux which is a real physical observable, so A_m is Hermitian, i.e $A_m(i, j) = A_m^*(j, i)$, so we obtain the resulting A_m:

$$A_m = \begin{bmatrix} 2t\cos(2\pi\frac{\phi}{\phi_0} - k_y a) & t & 0 & 0 & 0 & \cdots & te^{-ik_x qa} \\ t & 2t\cos(2\pi\frac{\phi}{\phi_0}(1 + 1/2) - k_y a) & t & 0 & 0 & \cdots & 0 \\ 0 & t & 2t\cos(4\pi\frac{\phi}{\phi_0} - k_y a) & t & 0 & \cdots & 0 \\ \vdots & \vdots & & \ddots & \ddots & \ddots & \vdots \\ te^{ik_x qa} & 0 & 0 & \cdots & 0 & t & 2t\cos(2\pi\frac{\phi}{\phi_0}(q + 1/2) - k_y a) \end{bmatrix}.$$

(4.7)
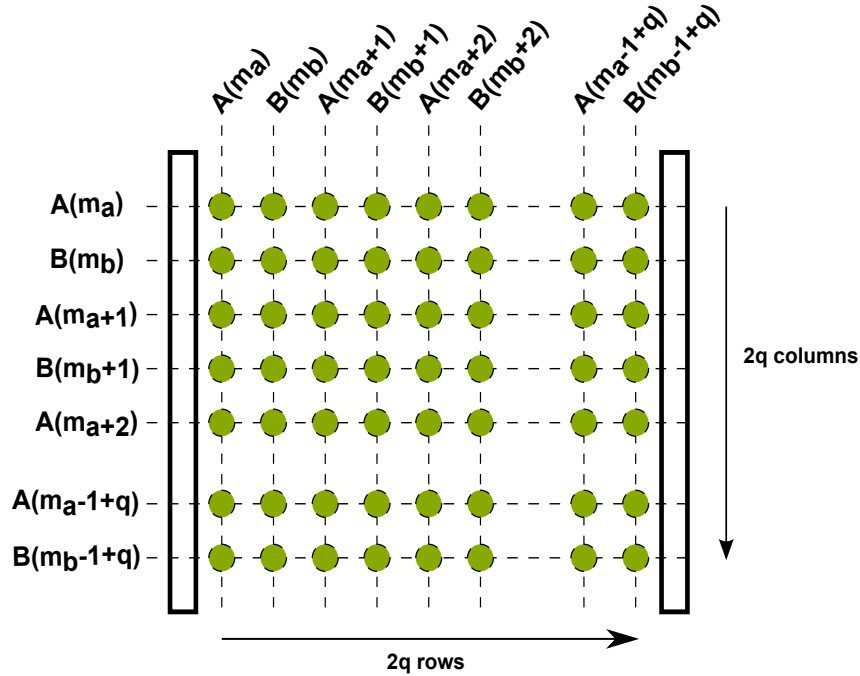
Figure 4.5: The organization scheme for A_m matrix shown for two kinds of atoms in the unit cell [43].

This scheme for the generation of the A_m matrix can be viewed via Fig. 4.5, which is suitable for our case of enlarged unitcell aligned horizontally. The rows and the columns are reserved for the atoms of corresponding labels. The entries of the A_m matrix are the interactions of the atoms which has the index correlated with the labels of the atoms.

Rectangular unit cell aligned vertically

If we have a similar geometric alignment seen in the Fig. 4.4(c), we can easily generate the A_m matrix by following the steps as we did for Fig. 4.4(b). The only things we should know additionally are the phase factors. We have $t e^{\pi \frac{\phi}{\phi_0} - k_y a}$ terms in addition to the tight-binding terms between the atom $A(m_a)$ and atoms $B(m_b)$, and also in between the atom $B(m_b)$ and atoms $A(m_a)$. Different from the previous example, here we have a $4q \times 4q$ A_m matrix because of the periodicity

Table 4.1: The scheme for the interactions between the atoms [43].

| | 1st N. N. | 2nd N. N. |
Atom Label	Interactions	Interactions
Atom A	B,D	C
Atom B	A,C	D
Atom C	B,D	A
Atom D	A,C	B

of the exponential factor with $2q$, and we have two different types of atoms.

$$
A_m = \begin{bmatrix}
0 & 2tcos(\pi\frac{\phi}{\phi_0} - k_y a) & t & 0 & \cdots & te^{-ik_x 2qa} & 0 \\
2tcos(\pi\frac{\phi}{\phi_0} - k_y a) & 0 & 0 & t & \cdots & & te^{-ik_x 2qa} \\
t & 0 & 0 & 2tcos(2\pi\frac{\phi}{\phi_0} - k_y a) & 0 & \cdots & 0 \\
0 & t & 2tcos(2\pi\frac{\phi}{\phi_0} - k_y a) & 0 & 0 & \cdots & 0 \\
& & \vdots & \ddots & \ddots & \ddots & \vdots \\
te^{ik_x 2qa} & & & & & & \\
0 & te^{ik_x 2qa} & 0 & \cdots & t & 2tcos(4q\pi\frac{\phi}{\phi_0} - k_y a) & 0
\end{bmatrix},
$$

$$(4.8)$$

A more general example: Square lattice of 4 atoms in the unit cell with the second nearest neighbor interactions

Now, suppose that we have a square lattice in which we have four different atoms oriented as shown in Fig. 4.4(d). For this case, since we have four different atoms, we have the wave vectors as;

$$
\Psi(m) = \begin{bmatrix} \varphi(m_a) \\ \varphi(m_b) \\ \varphi(m_c) \\ \varphi(m_d) \end{bmatrix},
$$

and also we have a 4x4 block Hamiltonian;

$$
H = \begin{bmatrix}
H^{AA} & H^{AB} & H^{AC} & H^{AD} \\
H^{BA} & H^{BB} & H^{BC} & H^{BD} \\
H^{CA} & H^{CB} & H^{CC} & H^{CD} \\
H^{DA} & H^{DB} & H^{DC} & H^{DD}
\end{bmatrix},
$$

If we consider both the first and the second nearest neighbor interactions, we have the interaction scheme showed in the Table 4.1. For example, the atom A will have the 1st order interactions with two atoms labelled by B and two atoms labelled by D; and also it will have the second order interaction with 4 atoms all labelled by C. We have the phase factors due to the magnetic field through the interactions which align in the y direction as well as the ones which have a non-zero y direction component. As as result, to speak in terms for the atom $A(m_a)$, we will have:

$$2cos(\pi\frac{\phi}{\phi_0}m_a - k_y a) = \theta(AD_1)$$

for the interaction with D atoms, and

$$2cos(\pi\frac{\phi}{\phi_0}(m_a - 1/4) - k_y a) = \theta(AC_2)$$

for the interaction with the atoms labelled by $C(m_c - 1)$, and in addition

$$2cos(\pi\frac{\phi}{\phi_0}(m_a + 1/4) - k_y a) = \theta(AC_1)$$

due to the interaction with the atoms labelled by $C(m_c)$. In addition, let us denote the second order tight-binding interaction coefficient as t'. After incorporating the Bloch condition, and calculating the magnetic phase factors for the rest of the atoms, we can write the A_m matrix:

$$A_m = \begin{bmatrix} 0 & t & t'\theta(AC_1) & t\theta(AD_1) & 0 & 0\cdots & 0 & 0 & te^{-ik_x 2qa} & t'\theta(AC_2)e^{-ik_x 2qa} \\ t & 0 & t\theta(BC_1) & t'\theta(BD_1) & t & 0\cdots & 0 & t'\theta(BD_2) & 0 & 0 \\ \vdots & \vdots & \vdots & \vdots & \vdots & \cdots & 0 & \cdots & \vdots & \vdots \\ 0 & 0 & 0 & 0 & 0 & \cdots & 0 & \cdots & & \\ t'\theta(CA_1)e^{ik_x 2qa} & 0 & 0 & te^{ik_x 2qa} & 0 & \cdots & \ddots & \ddots & \vdots & \vdots \\ 0 & 0 & 0 & 0 & \cdots & t'\theta(BD_2) & t\theta(DA1) & t'\theta(DB1) & t & 0 \end{bmatrix}$$

$$(4.9)$$
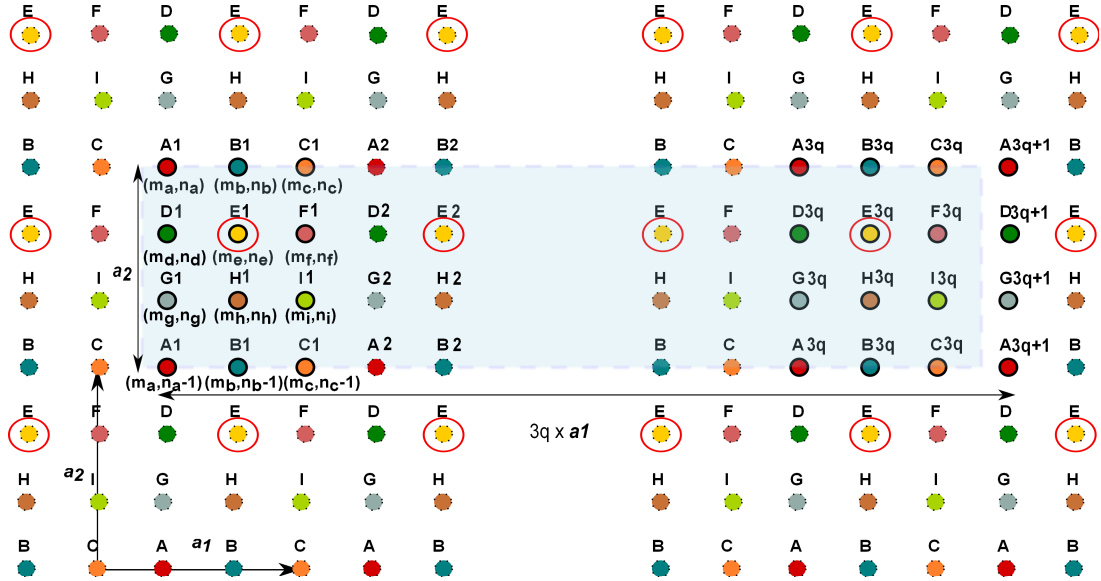
Figure 4.6: Magnetic unit cell of square lattice with 9 atoms in the basis of the unit cell, and $27q$ atoms in the basis of the magnetic unit cell. The encircled atoms with label "E" are treated as impurity or vacancy [43].

4.2.2   Square Lattice of 9 Atoms in the Basis

With the scheme outlined above, we can expand our unit cell as needed. We use an enlarged unit cell composed of 9 atoms to model impurities or vacancies, corresponding to a point defect concentration of $1/9 \simeq 11\%$. We label the atoms with the letters "A,B,...,E,...,H,I". We pick the fifth one with label "E" and treat it as a vacancy or impurity by modifying its hopping constants. We leave the remaining atoms with the usual square lattice 1st order hopping constant $t = 1.0$, and the 2nd order hopping constant is set to 0.05 which is almost on the same order with the 2nd nearest neighbor calculations done by Y. Hatsugai and M. Kohmoto [88].

Due to the change in the magnetic phase factors, now our system is $3q$ periodic, and since we have 9 atoms in the basis, the resulting A_m matrix has the dimension of $27q \times 27q$. The magnetic unit cell for the corresponding case is given in Fig. 4.6. With the similar procedure performed in subsection 4.2.1, we easily generate the A_m matrix, with or without the next nearest neighbor hopping. We alter
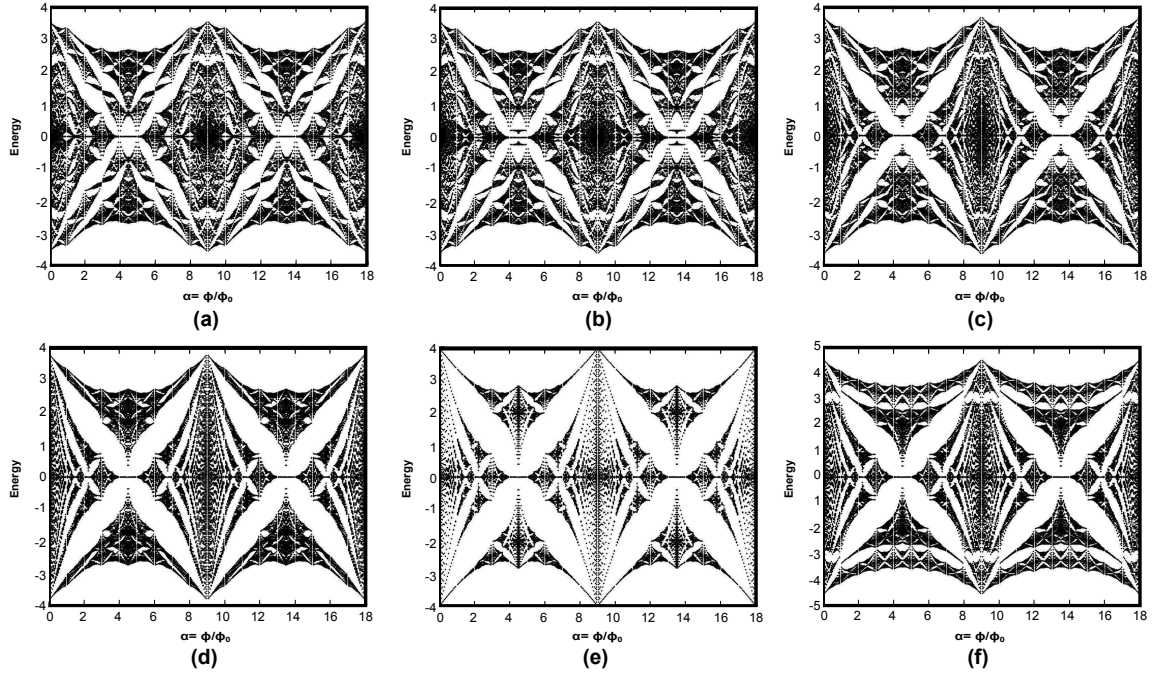
Figure 4.7: Energy (in the units of "t") versus $\alpha = p/q = \phi/\phi_0$ defined as the flux per enlarged unitcell, results in the Hofstadter Butterflies for the corresponding cases: **(a)** "E" is a vacancy with $t_E = 0.0$. **(b)** "E" is an impurity with $t_E = 0.25$. **(c)** "E" is an impurity with $t_E = 0.50$. **(d)** "E" is an impurity with $t_E = 0.75$. **(e)** All of the atoms are the same with $t_E = 1.00$. **(f)** "E" is an impurity with $t_E = 1.50$ [43].
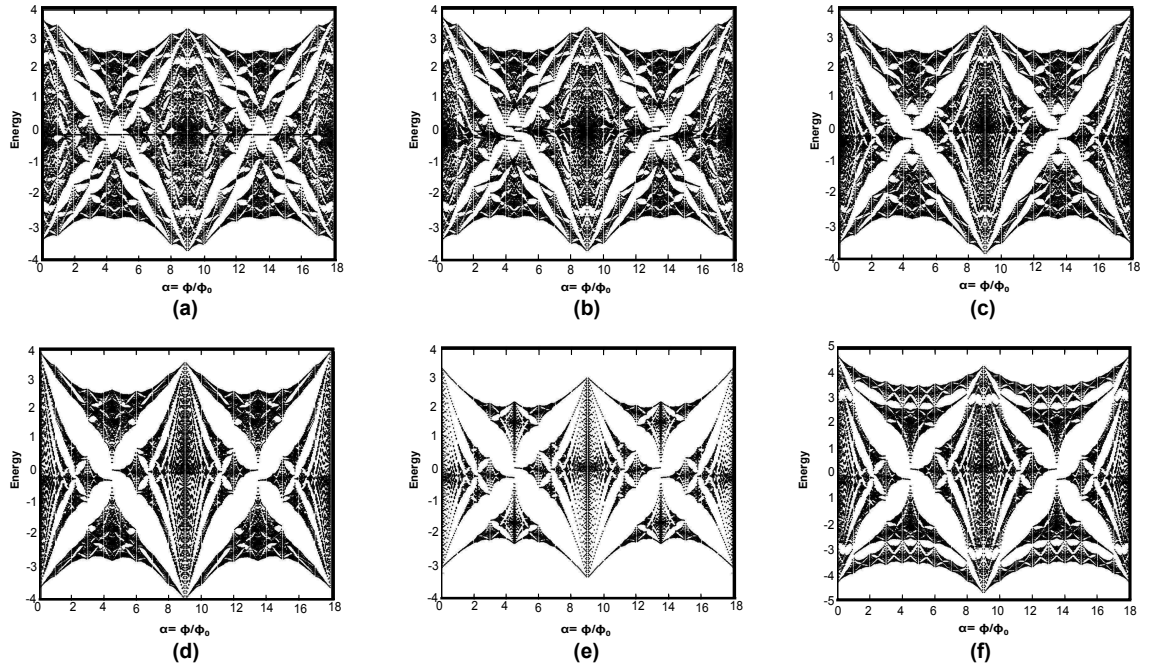
Figure 4.8: Energy (in the units of "t") versus $\alpha = p/q = \phi/\phi_0$ defined as the flux per enlarged unitcell, results in the Hofstadter Butterflies. Both the 1st and the 2nd nearest neighbor interactions are considered, for the corresponding impurity and vacancy cases: **(a)** "E" is a vacancy with $t_E = 0.0$ and $tt_E = 0.0$. **(b)** "E" is an impurity with $t_E = 0.25$ and $tt_E = 0.025$. **(c)** "E" is an impurity with $t_E = 0.50$ and $tt_E = 0.025$. **(d)** "E" is an impurity with $t_E = 0.75$ and $tt_E = 0.025$. **(e)** All of the atoms are the same with $t_E = t = 1.00$ and $tt_E = tt = 0.05$. **(f)** "E" is an impurity with $t_E = 1.50$ and $tt_E = 0.075$ [43].

the hopping constant of the interactions involving atom labelled "E" in the A_m matrix. The eigenvalues of the A_m matrix for all the k-points in the magnetic Brillouin zone as a function of $\alpha = \phi/\phi_0$ gives the Hofstadter Butterfly in the presence of the point defects.
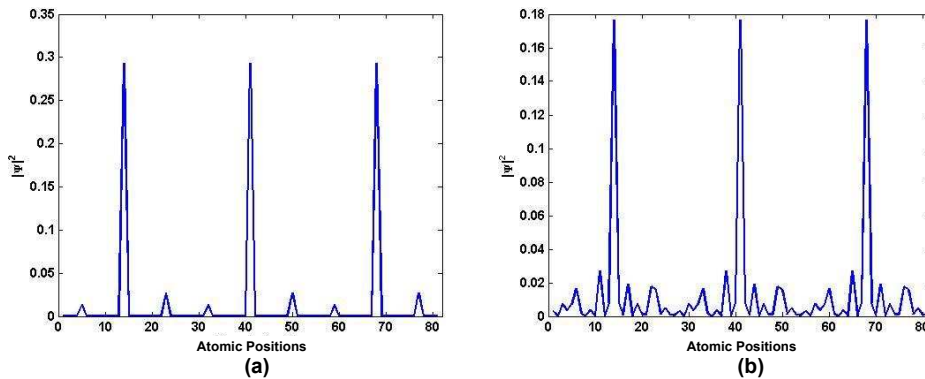
Figure 4.9: (Color online) $| \psi |^2$ plots of the localized state wavefunction as a function of atomic positions of the atoms whose labels are within the boundaries of the magnetic unit cell. The first plot is for the atom "E" which is close to being a vacancy, i.e. $t_E = 0.005$. The dirac delta like shaped peaks correspond to the positions of the atom "E". Since $q = 3$, there are 9 atoms with label "E" in the magnetic unit cell. The second one has $t_E = 0.50$. As the hopping constant increases, the wavefunction expands more among the other atoms [43].

4.3 Hofstadter Butterflies of Defective Square Lattice

We follow the procedure that we described in the Subsection 4.2.1 for the modelling of an impurity or a vacancy located on a lattice point (substitutional positions) of the square lattice. The unit cell as well as the magnetic unit cell can be viewed in Fig. 4.6. In this figure, the atom treated as an impurity or a vacancy is labelled with "E". As a first step, we consider only the 1st nearest neighbor interactions. We label the nearest neighbor hopping constant for atom "E" as t_E, again measured in units of t. We alter this parameter, t_E, in the range from 1.5 to 0.001 for the impurity cases, while we obtain the vacancy case for $t_E = 0$. Note that, we get the pure case when $t_E = 1.0$, corresponding to the case where all the atoms are the same. The impurity or the vacancy case replacing 1 atom out of 9 atoms corresponds to a defect concentration on the order of 11%.

After diagonalizing the A_m matrix we get the energy eigenvalues as a function

of $\alpha = \phi/\phi_0$. The Hofstadter butterflies for selected values of parameter t_E are plotted in Fig. 4.7. The range of α defined as the flux per enlarged unitcell is set from 0 to 18, in accordance with the results where we include the 2nd order interactions. As displayed in Fig. 4.8 for the latter case, there is an extra envelope like periodicity within the butterflies. The pure case with $t_E = 1.0$ labelled by **(f)** is the same spectrum plotted for a single atom in Fig. 4.3. The only difference between these two plots is the periodicity in α because α in our notation is the magnetic flux per *enlarged* unitcell. In both of the spectra, there is a zero energy band which divides up the graph horizontally in two identical parts. This is a consequence of the bipartite symmetry of the square lattice. When we set $t_E = 0.75$, we see a different spectrum with new gaps and bands formed as shown in Fig. 4.7(d). For the case where we reduce t_E to 0.50, we see the emerging of dome shaped gaps around $\alpha = 4.5$ and $\alpha = 13.5$ with an energy value of ± 0.8 as plotted in frame **(c)**. Within these gaps, Hall conductance is zero as discussed in the next section. A sequence of bands are formed between the dome shaped gaps which are symmetric about $E = 0$. These bands are clearly related to states localized around the impurity. As we continue to reduce t_E, i.e. $t_E = 0.25$ showed in Fig. 4.7(b), we see that these gaps become more elliptic compared to Fig. 4.7(c). We also note that the "impurity bands" between the domes approach to the horizontal energy line $E = 0$. One limit of impurity case is the vacancy, where $t_E = 0$, and its spectrum displayed in Fig. 4.7(a), show elliptic gaps around $E = 0$. Moreover, the "impurity bands" now collapse to the $E = 0$ line, signifying that the impurity is decoupled from the rest of the system. In the opposite limit we also consider the impurity with a stronger hopping constant. We examine this situation for $t_E = 1.50$ and display the corresponding Hofstadter Butterfly in Fig. 4.7(f). For this strongly coupled impurity, the spectrum is modified near the maximum and the minimum energy values. Hence, the bands due to the impurity states appear near $E = \pm 4$ as clearly seen in the Fig. 4.7(f). The low energy structure ($E \sim 0$) remains mostly unmodified by the presence of strongly coupled impurity.

The effect of the 2nd nearest neighbor interactions on the Hofstadter Butterfly was thoroughly examined in Ref. [88]. Inclusion of the next nearest neighbor

interactions are important for two reasons: First they would be present in a solid state system and also in a cold atom system as long as the optical lattice is not too deep. Second, even if they are weak, such interactions break the bipartite symmetry of the lattice. As a result the spectrum is no longer symmetric about $E = 0$. Thus by including the next nearest neighbor interactions, we make sure that the results for our impurities are robust with respect to the breaking of the bipartite symmetry. As we introduce second order hoppings, the butterfly loses its mirror symmetry around $\alpha = 4.5$ and $\alpha = 13.5$ lines. The gaps and bands gain positive (negative) shifts for $\alpha > 4.5$ ($\alpha < 4.5$). This shift is reversed near the $\alpha = 13.5$ line. As a result of the self similar structure of the butterfly, similar shifts appear at other principal rational fractions with even denominators. In addition to that, the spectrum gains a new envelope like periodicity. In order to display this new periodicity, we plotted our butterflies as a function of α from 0 to 18. The corresponding spectra for different impurity cases is presented in Fig. 4.8. While the width of gaps and bands change, there is no qualitative difference in the number and the location of the gaps when compared to Fig. 4.7. Most importantly, the dome shaped gaps and impurity bands observed with only first order interactions are robust with respect to second order hopping. These structures are shifted in accordance with the general spectrum, nonetheless their general properties remain unaltered.

Chapter 5

Hofstadter Butterflies of Graphene and Defective Graphene

5.1 Graphene in Perpendicular Magnetic Field

In Section 2.2, we have given a brief description of tight-binding method for graphene , which is in a neutral state such that there is no external field perturbation to the system. Since we are working with magnetic field, we should introduce this external field to our algebra. We assume that, we have a magnetic field $\vec{\mathbf{B}}$ acting in the z direction which is perpendicular to the plane of consideration. The magnetic field will act in a manner to modify the momentum and also the wave vector; $\hbar\mathbf{k} \rightarrow \hbar\mathbf{k} - \frac{e\vec{\mathbf{A}}}{c}$ which is called the *Peierl's substitution*. In order to simplify the calculations, we chose the Landau gauge with the vector field $\vec{\mathbf{A}} = (0, Bx, 0)$. If we rearrange our terms of the Hamiltonian for graphene which has 4 atoms shown in Fig. 5.1 we will get;

$$
\begin{aligned}
H^{AC} &= V_{pp\pi}e^{ik_x a/2}e^{-ik_y a\sqrt{3}/2}e^{-2\pi i\frac{e}{\hbar}\int_{\vec{R}_{m_a,n_a}}^{\vec{R}_{m_c,n_c}} \vec{\mathbf{A}}\cdot\vec{dl}}, \\
H^{AD} &= V_{pp\pi}e^{ik_x a/2}e^{ik_y a\sqrt{3}/2}e^{-2\pi i\frac{e}{\hbar}\int_{\vec{R}_{m_a,n_a}}^{\vec{R}_{m_d,n_d+1}} \vec{\mathbf{A}}\cdot\vec{dl}}
\end{aligned}
\tag{5.1}
$$
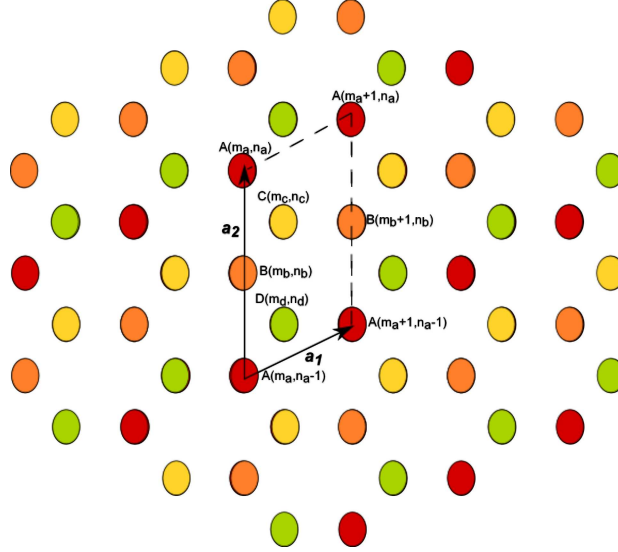
Figure 5.1: Asymmetric unitcell choice of graphene which contains 4 atoms. The corresponding lattice vectors are $\vec{a}_1 = \hat{x}3a/2 + \hat{y}a\sqrt{3}/2$ and $\vec{a}_2 = \hat{y}2a\sqrt{3}$

$$+ \quad V_{pp\pi} e^{-ik_x a} e^{-2\pi i \frac{e}{\hbar} \int_{\vec{R}_{m_a,n_a}}^{\vec{R}_{md-1,n_d+1}} \vec{A}\cdot\vec{dl}} \quad , \tag{5.2}$$

where the integrals are taken through the smallest geometric distance between the atoms. The vector $\vec{R}_{m_\alpha,n_\alpha}$ with $\alpha = a, b, c, d$ is the vector denoting the distance of atom labelled by the usual graphene and CNT indices (m_α, n_α) from the origin. For instance,

$$\vec{R}_{m_a,n_a} = m_a \vec{a_1} + n_a \vec{a_2}; \tag{5.3}$$

These exponentials containing line integrals bring phase factors originating from the magnetic field applied. As a result, after integrating over the lines joining the atoms and also converting all the (m_α, n_α) pairs into (m_a, n_a) pairs, we obtain exponential terms as a function of m_a -as a result of chosen gauge- and directly proportional to the magnetic field.

$$H^{AC} \quad = \quad V_{pp\pi} e^{ik_x a/2} e^{-ik_y a\sqrt{3}/2} e^{i\frac{e}{\hbar}\pi B a^2 \frac{3\sqrt{3}}{2}(m_a+1/6)},$$

$$H^{AD} \;\; = \;\; V_{pp\pi}e^{ik_x a/2}e^{ik_y a\sqrt{3}/2}e^{-i\frac{e}{\hbar}\pi Ba^2\frac{3\sqrt{3}}{2}(m_a+1/6)} + V_{pp\pi}e^{-ik_x a} \qquad (5.4)$$

If we introduce the flux quanta $\phi_0 = h/e$ and the magnetic flux $\phi = 3\sqrt{3}Ba^2$ magnetic field times the area of the unitcell, then we get a neater expression:

$$H^{AC} \;\; = \;\; V_{pp\pi}e^{ik_x a/2}e^{-ik_y a\sqrt{3}/2}e^{i\frac{\pi}{2}\frac{\phi}{\phi_0}(m_a+1/6)},$$
$$H^{AD} \;\; = \;\; V_{pp\pi}e^{ik_x a/2}e^{ik_y a\sqrt{3}/2}e^{-i\frac{\pi}{2}\frac{\phi}{\phi_0}(m_a+1/6)} + V_{pp\pi}e^{-ik_x a} \qquad (5.5)$$

The term $e^{ik_x a/2}e^{-ik_y a\sqrt{3}/2}$ can be written as a representation of the atomic wave-function $\varphi(m_c, n_c)$. If we assume that $\varphi(x, y) = \varphi(x)e^{ik_y y}$,and we rewrite the Schödinger equation in terms of the modified elements of the Hamiltonian by unifying the exponential expressions and changing them into the form of the wavefunctions, we end up with Harper's equation [54] which implies the matrix equation;

$$\Psi_m = U_m\Psi_m + V_m\Psi_{m+1} + W_m\Psi_{m-1}, \qquad (5.6)$$

where Ψ_m is a column vector with:

$$\Psi_m = \begin{bmatrix} \psi(m_a) \\ \psi(m_b) \\ \psi(m_c) \\ \psi(m_d) \end{bmatrix} \qquad (5.7)$$

The Harper's equation is a recursive matrix equation, which can be expressed by three main matrices U_m, W_m and V_m, where we have used a short-hand notation for the exponential factors. For instance, ϑ_{AC} is equal to $e^{-ik_y a\sqrt{3}/2}e^{i\frac{\pi}{2}\frac{\phi}{\phi_0}(m_a+1/6)}$. The explicit form of the matrices is given below:

$$U_m = \begin{bmatrix} 0 & 0 & V_{pp\pi}e^{i\vartheta_{AC}} & V_{pp\pi}e^{i\vartheta_{AD}} \\ 0 & 0 & V_{pp\pi}e^{i\vartheta_{BC}} & V_{pp\pi}e^{i\vartheta_{BD}} \\ V_{pp\pi}e^{i\vartheta_{CA}} & V_{pp\pi}e^{i\vartheta_{CB}} & 0 & 0 \\ V_{pp\pi}e^{i\vartheta_{DA}} & V_{pp\pi}e^{i\vartheta_{DB}} & 0 & 0 \end{bmatrix}, \qquad (5.8)$$

$$
W_m = \begin{bmatrix} 0 & 0 & 0 & V_{pp\pi} \\ 0 & 0 & V_{pp\pi} & 0 \\ 0 & 0 & 0 & 0 \\ 0 & 0 & 0 & 0 \end{bmatrix} \qquad V_m = \begin{bmatrix} 0 & 0 & 0 & 0 \\ 0 & 0 & 0 & 0 \\ 0 & V_{pp\pi} & 0 & 0 \\ V_{pp\pi} & 0 & 0 & 0 \end{bmatrix}
$$

Let us assume that the ratio of flux over flux quanta ϕ/ϕ_0 is equal to p/q, where p and q are two integers and their ratio is equal to α. The terms like $e^{i\frac{\pi}{2}\frac{p}{q}(m_a+1/6)}$ are periodic with m_a with the periodicity $4q$. Since if we have $m_a = m_a + 4q$, then $e^{i\frac{\pi}{2}\frac{p}{q}(m_a+1/6)} \rightarrow e^{i\frac{\pi}{2}\frac{p}{q}(m_a+1/6)}e^{2\pi i}$ where $e^{2\pi i}$ is equal to 1. So the index, m_a runs over all the numeric values of $4q$. For m_a is equal to 1, Eq. 5.6 becomes a recursive equation $\Psi_1 = U_1\Psi_1 + V_1\Psi_2 + W_1\Psi_0$, and for m_a is equal to $4q$ it becomes $\Psi_{4q} = U_{4q}\Psi_{4q} + V_{4q}\Psi_{4q+1} + W_{4q}\Psi_{4q-1}$. Since we have $4q$ lattice points i.e. $16q$ atoms are connected, we can apply Bloch condition onto the wavefunctions in the x direction;

$$
\psi(m_a + 4q) = e^{ik_x a_{1x} 4q}\psi(m_a). \tag{5.9}
$$

According to the equation 5.9, we obtain $\psi(0) = e^{-ik_x a_{1x} 4q}\psi(4q)$ when we set m_a to be 0. Similarly, if we set $m_a = 1$ we find the value for $\psi(4q+1)$ which is equal to $e^{ik_x a_{1x} 4q}\psi(1)$. As a result, we have a new matrix equation;

$$
\begin{bmatrix} \Psi_1 \\ \Psi_2 \\ \vdots \\ \Psi_{4q-1} \\ \Psi_{4q} \end{bmatrix} = \begin{bmatrix} U_1 & V_1 & 0 & 0 & \cdots & 0 & W_1^* \\ W_2 & U_2 & V_2 & 0 & 0 & \cdots & 0 \\ 0 & W_3 & U_3 & V_3 & 0 & \cdots & 0 \\ \vdots & \vdots & \ddots & \ddots & \ddots & \ddots & \vdots \\ V_{4q}^* & 0 & 0 & \cdots & 0 & W_{4q} & U_{4q} \end{bmatrix} \begin{bmatrix} \Psi_1 \\ \Psi_2 \\ \vdots \\ \Psi_{4q-1} \\ \Psi_{4q} \end{bmatrix}, \tag{5.10}
$$

with $W_1^* = e^{-ik_x a_{1x} 4q}W_1$ and $V_{4q}^* = e^{ik_x a_{1x} 4q}V_{4q}$. The huge matrix is called the A_m matrix which has the dimensions of $16q \times 16q$. Since this is a eigenvalue equation, the eigenvalues will give the desired energies as a function of flux (ϕ/ϕ_0). For irrational values of $\alpha = \phi/\phi_0$, the spectrum takes the form of the *Hofstadter Butterfly*. This irrational case corresponds to the case in which p and q are mutually prime.
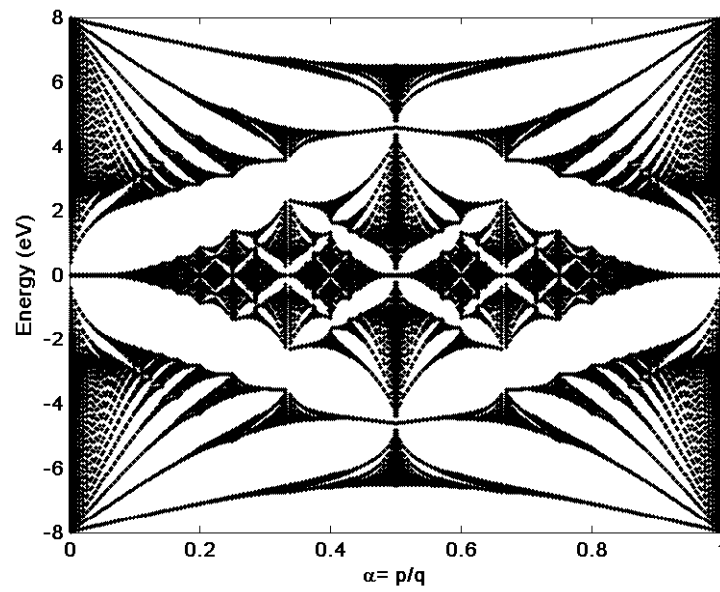
Figure 5.2: The Hofstadter Butterfly spectrum for graphene with the p_z orbitals. Only the 1st nearest neighbor interactions are included. The tight-binding parameter are displayed in Table 2.1 and $q = 501$.

The Hofstadter Butterfly of graphene with only the p_z orbitals are displayed in Fig. 5.2 which is the solution of Eq. 5.2.1. The spectrum shows a self similar character with infinite number of bands and gaps.

All-orbital calculations

Up to know, we have discussed the well-known tight binding approximation for graphene under perpendicular magnetic field. We only included the p_z orbitals in our calculations in accordance with the literature. In order to obtain more accurate results for the energy flux dependence, we have to consider all the orbitals (s, p_x, p_y, p_z) since they all contribute to the band structure. The difference between the all orbits calculation and the only p_z orbitals calculation is, we do not have single values for the elements of the Hamiltonian matrix given in equation (2.12), instead we have sub-matrices for which we have given two examples in equations 2.13 and 2.13. For this case, we have sub-matrix elements in the form of $\langle 2P^\beta|H|2P^\beta\rangle$ where P stands for all s, p_x, p_y and p_z orbitals; and β denotes the letter index of the atoms (A, B, C, and D). As an example the matrix element $\langle 2P_x^A|H|2P_y^D\rangle$ is given by:

$$
\begin{aligned}
\langle 2P_x^A|H|2P_y^D\rangle &= -(V_{pp\pi} + V_{pp\sigma})sin(\pi/6)cos(\pi/6)e^{ik_x a/2}e^{ik_y a\sqrt{3}/2} \\
&+ 0.e^{-ik_x a}.
\end{aligned} \tag{5.11}
$$

The energy spectrum for graphene under the influence of perpendicular magnetic field with all orbitals are considered is displayed in Fig. 5.3.

5.2   Defective Graphene

Although the Hofstadter Butterfly for perfect graphene is well understood, the effect of impurities on this spectrum is less investigated. As any real sample would contain a concentration of point defects, it is important to systematically study their influence on electronic structure. The first study of such point defects considered the effect of vacancies on the Landau Levels of graphene [89]. It has
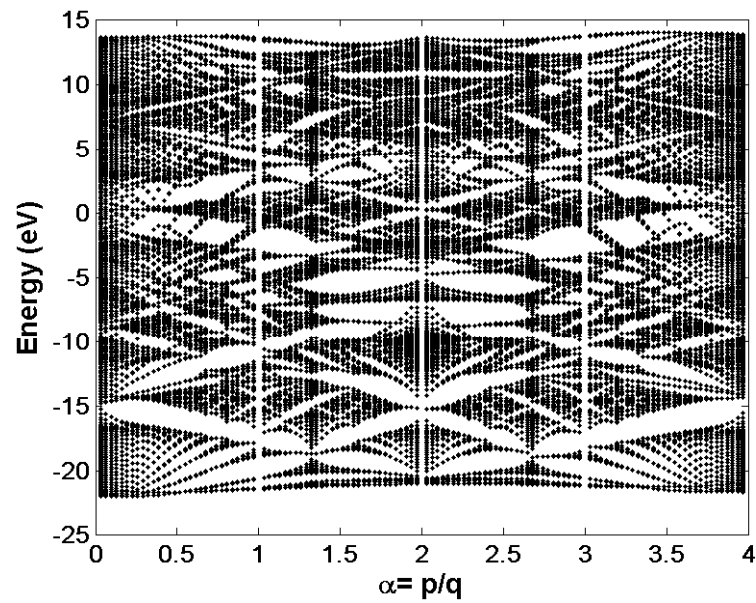
Figure 5.3: The Hofstadter Butterfly spectrum for graphene with all of the orbitals [42]. Both the 1st and the 2nd nearest neighbor interactions are included. The tight-binding parameter are displayed in Table 2.1.

been shown that vacancies introduce new states between the Landau Levels and the presence of a vacancy lattice introduces extra bands to the spectrum. In this thesis, we present a systematic study in which both vacancies and impurities are considered. Furthermore, we investigate the evolution of impurity bands with coupling strength.

The tight-binding methodology works well for the energy spectrum calculation of graphene as a function of magnetic flux [40]. In the case of the Hofstadter Butterflies, the usual unit cell of graphene with two atoms in the basis is enough to model the fractal energy spectrum. In this study, we investigate the effects of substitutional point defects such as vacancy or impurity on the electronic structure. We treat one of the atoms in the unit cell as a vacancy with zero hopping constants, or an impurity atom with different hopping constants from rest of the lattice. The effect of impurities can be modelled by introducing a dilute impurity lattice which requires the study of larger unit cell. In order to study defects with low concentration, in this paper, we use an enlarged unit cell which has 8 atoms in the basis. For this case, we obtain an impurity concentration of $1/8 = 12.5\%$. In such a large unit cell there is no direct hopping between impurities even in the presence of second order interactions. We also point out that our method is applicable to any general defect concentration.

The section is organized as follows: First, we outline the adoption of the tight-binding methodology to graphene described within an enlarged unit cell. Then, we label one of the atoms in the enlarged unit cell as an impurity or vacancy as was briefly outlined in Chapter 2. We change the hopping constant(s) of this defect atom and present the resulting butterflies as two main sets of different imperfection scenarios: Only the first nearest neighbor interactions are considered, and both the first and the second nearest neighbor interactions are considered.

5.2.1   Enlarged Unit Cell of Graphene

Since we have 8 atoms in the unit cell, as shown in Fig.5.4, the tight-binding Hamiltonian is an 8×8 matrix:
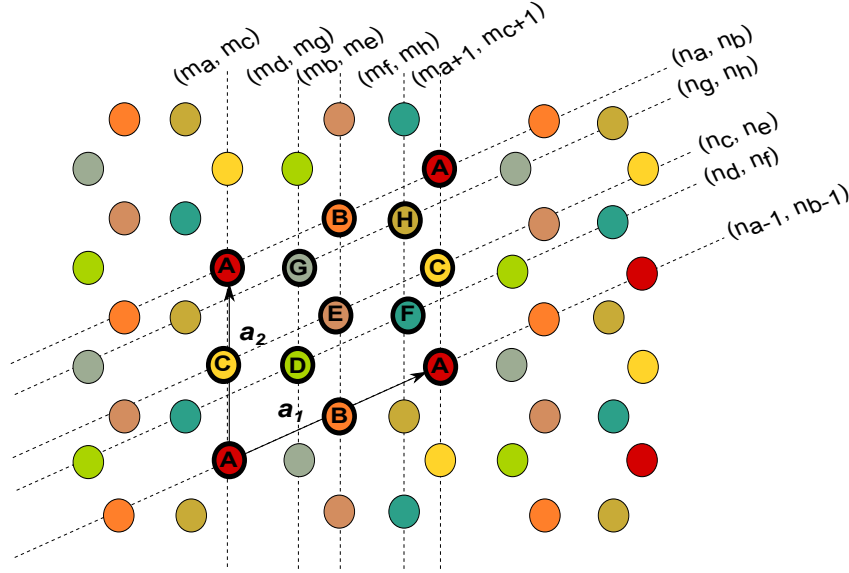
Figure 5.4: Enlarged unit cell for graphene which is suitable for point defect calculations. The lattice vectors are: $\vec{a_1}=\hat{x}3a + \hat{y}a\sqrt{3}$ and $\vec{a_2}=\hat{y}2a\sqrt{3}$ [42].

$$
H = \begin{bmatrix}
H^{AA} & H^{AB} & H^{AC} & H^{AD} & H^{AE} & H^{AF} & H^{AG} & H^{AH} \\
H^{BA} & H^{BB} & H^{BC} & H^{BD} & H^{BE} & H^{BF} & H^{BG} & H^{BG} \\
H^{CA} & H^{CB} & H^{CC} & H^{CD} & H^{CE} & H^{CF} & H^{CG} & H^{CH} \\
H^{DA} & H^{DB} & H^{DC} & H^{DD} & H^{DE} & H^{DF} & H^{DG} & H^{DH} \\
H^{EA} & H^{EB} & H^{EC} & H^{ED} & H^{EE} & H^{EF} & H^{EG} & H^{EH} \\
H^{FA} & H^{FB} & H^{FC} & H^{FD} & H^{FE} & H^{FF} & H^{FG} & H^{FH} \\
H^{GA} & H^{GB} & H^{GC} & H^{GD} & H^{GE} & H^{GF} & H^{GG} & H^{GH} \\
H^{HA} & H^{HB} & H^{HC} & H^{HD} & H^{HE} & H^{HF} & H^{HG} & H^{HH}
\end{bmatrix}.
$$

Each element of this matrix gives the interaction terms between the atoms with corresponding labels. The elements of the tight-binding matrix are scalar expressions when we consider only the p_z orbitals. If we take all the orbitals into account, then each of the elements is a matrix itself rather than a scalar expression. We introduce the magnetic field to the system by the Peierls substitution:

$$
\hbar\mathbf{k} \rightarrow \hbar\mathbf{k} - \frac{e\vec{\mathbf{A}}}{c}.
$$

For convenience, we use Landau Gauge to describe the perpendicular magnetic field with a vector potential $\vec{\mathbf{A}} = (0, Bx, 0)$. Since the wave vectors are modified,

we have new phase factors due to the magnetic field which are in the line integral form:

$$e^{i\vartheta_{magnetic}} = e^{-2\pi i \frac{e}{\hbar} \int_{\vec{R}_{m_\beta,n_\beta}}^{\vec{R}_{m_\alpha,n_\alpha}} \vec{\mathbf{A}}\cdot \vec{dl}},$$

where $\vec{R}_{m_\alpha,n_\alpha} = m_\alpha \vec{a_1} + n_\alpha \vec{a_2}$ with α, β are the labels of the atoms in the enlarged unit cell, and the integral is to be evaluated through the line connecting the neighboring atoms. We introduce the flux quanta as $\phi_0 = h/e$ and the amount of flux passing through the enlarged unit cell as $\phi = 6\sqrt{3}Ba^2$. So, the normalized magnetic flux can be expressed as $\phi/\phi_0 = p/q$, with two co-prime integers p and q. By rewriting the atomic wavefunctions in the separable form along x and y directions i.e. $\varphi(x,y) = \varphi(x)e^{ik_y y}$ we end up with the phase factors in new and neater forms. For instance:

$$e^{i\vartheta_{BG}} = e^{-ik_y|\vec{a_2}| + i\frac{\pi}{2}\frac{\phi}{\phi_0}(m_a + 5/12)}.$$

All the phase factors due to the 1st order interactions are in the same form, except the additive fractions to m_a in the parenthesis. This occurs due to conversion of all the other labelled indices to the ones of atom labelled "A". Under these circumstances, we have a new matrix equation which can be called generalized Harper's equation [54] involving three matrices:

$$\Psi_m = U_m \Psi_m + V_m \Psi_{m+1} + W_m \Psi_{m-1}, \tag{5.12}$$

where Ψ_m is a vector:

$$\Psi_m = \begin{bmatrix} \psi(m_a) \\ \psi(m_b) \\ \psi(m_c) \\ \psi(m_d) \\ \psi(m_e) \\ \psi(m_f) \\ \psi(m_g) \\ \psi(m_h) \end{bmatrix},$$

and U_m, W_m, V_m are the matrices shown below when we consider only the first order interactions and the p_z orbitals:

$$U_m = \begin{bmatrix} 0 & 0 & 0 & 0 & 0 & 0 & V_{pp\pi} & 0 \\ 0 & 0 & 0 & V_{pp\pi}e^{i\vartheta_{BD}} & 0 & 0 & V_{pp\pi}e^{i\vartheta_{BG}} & V_{pp\pi} \\ 0 & 0 & 0 & V_{pp\pi} & 0 & 0 & 0 & 0 \\ 0 & V_{pp\pi}e^{i\vartheta_{DB}} & V_{pp\pi} & 0 & V_{pp\pi}e^{i\vartheta_{DE}} & 0 & 0 & 0 \\ 0 & 0 & 0 & V_{pp\pi}e^{i\vartheta_{ED}} & 0 & V_{pp\pi} & V_{pp\pi}e^{i\vartheta_{EG}} & 0 \\ 0 & 0 & 0 & 0 & V_{pp\pi} & 0 & 0 & 0 \\ V_{pp\pi} & V_{pp\pi}e^{i\vartheta_{GB}} & 0 & 0 & V_{pp\pi}e^{i\vartheta_{GE}} & 0 & 0 & 0 \\ 0 & V_{pp\pi} & 0 & 0 & 0 & 0 & 0 & 0 \end{bmatrix},$$

$$W_m = \begin{bmatrix} 0 & 0 & 0 & 0 & 0 & V_{pp\pi}e^{i\vartheta_{AF}} & 0 & V_{pp\pi}e^{i\vartheta_{AH}} \\ 0 & 0 & 0 & 0 & 0 & 0 & 0 & 0 \\ 0 & 0 & 0 & 0 & 0 & V_{pp\pi}e^{i\vartheta_{CF}} & 0 & V_{pp\pi}e^{i\vartheta_{CH}} \\ 0 & 0 & 0 & 0 & 0 & 0 & 0 & 0 \\ 0 & 0 & 0 & 0 & 0 & 0 & 0 & 0 \\ 0 & 0 & 0 & 0 & 0 & 0 & 0 & 0 \\ 0 & 0 & 0 & 0 & 0 & 0 & 0 & 0 \\ 0 & 0 & 0 & 0 & 0 & 0 & 0 & 0 \end{bmatrix},$$

$$V_m = \begin{bmatrix} 0 & 0 & 0 & 0 & 0 & 0 & 0 & 0 \\ 0 & 0 & 0 & 0 & 0 & 0 & 0 & 0 \\ 0 & 0 & 0 & 0 & 0 & 0 & 0 & 0 \\ 0 & 0 & 0 & 0 & 0 & 0 & 0 & 0 \\ V_{pp\pi}e^{i\vartheta_{FA}} & 0 & V_{pp\pi}e^{i\vartheta_{FC}} & 0 & 0 & 0 & 0 & 0 \\ 0 & 0 & 0 & 0 & 0 & 0 & 0 & 0 \\ 0 & 0 & 0 & 0 & 0 & 0 & 0 & 0 \\ V_{pp\pi}e^{i\vartheta_{HA}} & 0 & V_{pp\pi}e^{i\vartheta_{HC}} & 0 & 0 & 0 & 0 & 0 \end{bmatrix}.$$

The index m_a is periodic in q with a period of $4q$. Hence, our new Hamiltonian is a $32q \times 32q$ matrix with 8 atoms in the enlarged unit cell and each is connected to $4q$ atoms. Eq. 5.6 is a periodic equation where m runs from 1 to $4q$. However, when $m = 1$ we have Ψ_0, and similarly when $m = 4q$ we get Ψ_{4q+1}. Since we have

the periodic boundary conditions, we have to retain these wavefunctions within the magnetic unit cell via Bloch's condition:

$$\psi(m_a + 4q) = e^{ik_x a_{1x} 4q} \psi(m_a).$$

As a result, we have a new matrix called A_m matrix which is our new Hamiltonian:

$$\begin{bmatrix} \Psi_1 \\ \Psi_2 \\ \vdots \\ \Psi_{4q-1} \\ \Psi_{4q} \end{bmatrix} = \begin{bmatrix} U_1 & V_1 & 0 & 0 & \cdots & 0 & W_1^* \\ W_2 & U_2 & V_2 & 0 & 0 & \cdots & 0 \\ 0 & W_3 & U_3 & V_3 & 0 & \cdots & 0 \\ \vdots & \vdots & \ddots & \ddots & \ddots & \cdots & \vdots \\ V_{4q}^* & 0 & 0 & \cdots & 0 & W_{4q} & U_{4q} \end{bmatrix} \begin{bmatrix} \Psi_1 \\ \Psi_2 \\ \vdots \\ \Psi_{4q-1} \\ \Psi_{4q} \end{bmatrix}.$$

The eigenvalues of this A_m matrix generate the Hofstadter-Rammal Butterfly when plotted as a function of $p/q = \alpha$. A similar procedure can be carried out in order to introduce the second order interactions. The second order interactions produce new phase factors and alter the U_m, W_m, and V_m matrices by modifying the phase factors for previous elements and generating new non zero entries. For a more accurate description, the second order interactions are important even though their values are small. To go one step further, we can also take all the orbitals $(s, p_x, p_y$ and $p_z)$ into account. This will enlarge A_m matrix to a $128q \times 128q$ matrix due to having four orbitals for each of the 8 atoms. The resulting butterfly with the second order interactions is presented in Fig. 5.3, which includes many bands, so it is more complicated than the one with only p_z orbitals. Note that in this study, we use the well established tight-binding parameter for graphene listed in Table 2.1. This complicated energy spectrum is not transparent enough to study the effects of the impurities. Since the aim of this paper is to understand the effects of the point defects, from now on we just concentrate on the p_z orbitals as in previous studies.

5.3   Hofstadter Butterflies of Defective Graphene

The energy spectrum for pure graphene is obtained in the previous section. Now, we concentrate on the effects of the impurities by modifying the A_m matrix. The

Hofstadter butterflies for the range of impurity hopping strengths are displayed in Figures 5.5 and 5.6 which constitute the results of this work.

The pure cases for up to first and second nearest neighbor interactions are displayed in panel **(c)** of both figures. The horizontal axes denotes the magnetic flux α which is from 0 to 24. This difference in α range occurs for two reasons. First of all, we enlarged our unit cell, as a result of that the amount of magnetic flux per unit cell is increased. Secondly, the 2nd order interactions bring an extra envelope-like periodicity to the butterflies. In order to visualize the butterflies through one whole period, we have to span more $\alpha = p/q$ when we consider the second order interactions. For the sake of comparison between the first and the second order interactions, we prefer to plot the butterflies of the first order interactions with the same range of α in accordance with the 2nd order results.

We created the basis for the calculation of the Hofstadter butterflies for graphene with point defects. By treating one of the eight atoms as a vacancy or an impurity we obtain a concentration of 12.5% as explained above. We choose the atom labelled by "E" as an imperfection. The vacancy case corresponds to the case where atom "E" has zero hopping constant(s). Similarly, by changing the hopping constant(s) involving the interactions among atom "E", we can monitor effects of different substitutional impurities on the electronic structure.

5.3.1 First Nearest Neighbors

The Hofstadter butterflies of graphene with point defects can be seen in Fig. 5.5 for the first order interactions. As we mentioned before, the pure case is given by label **(c)**. This is the usual Hofstadter butterfly for graphene. Since we have only the first nearest neighbor interactions, the spectrum is symmetric around $E = 0 \ eV$. When we introduce an impurity to the system with a smaller hopping constant of $V_{pp\pi}^{E} = \frac{3}{4}V_{pp\pi}$, given in Fig. 5.5**(d)**, we see new formations of gaps and bands especially at regions close to E_{min} and E_{max}. Near $\alpha = 2$ and $E \simeq \pm 4$, there is a formation of new gaps. In addition, the bands in the region $1 \leq E \leq 3 \ eV$ (and also symmetric region with respect to $E = 0 \ eV$ line), and α lying in
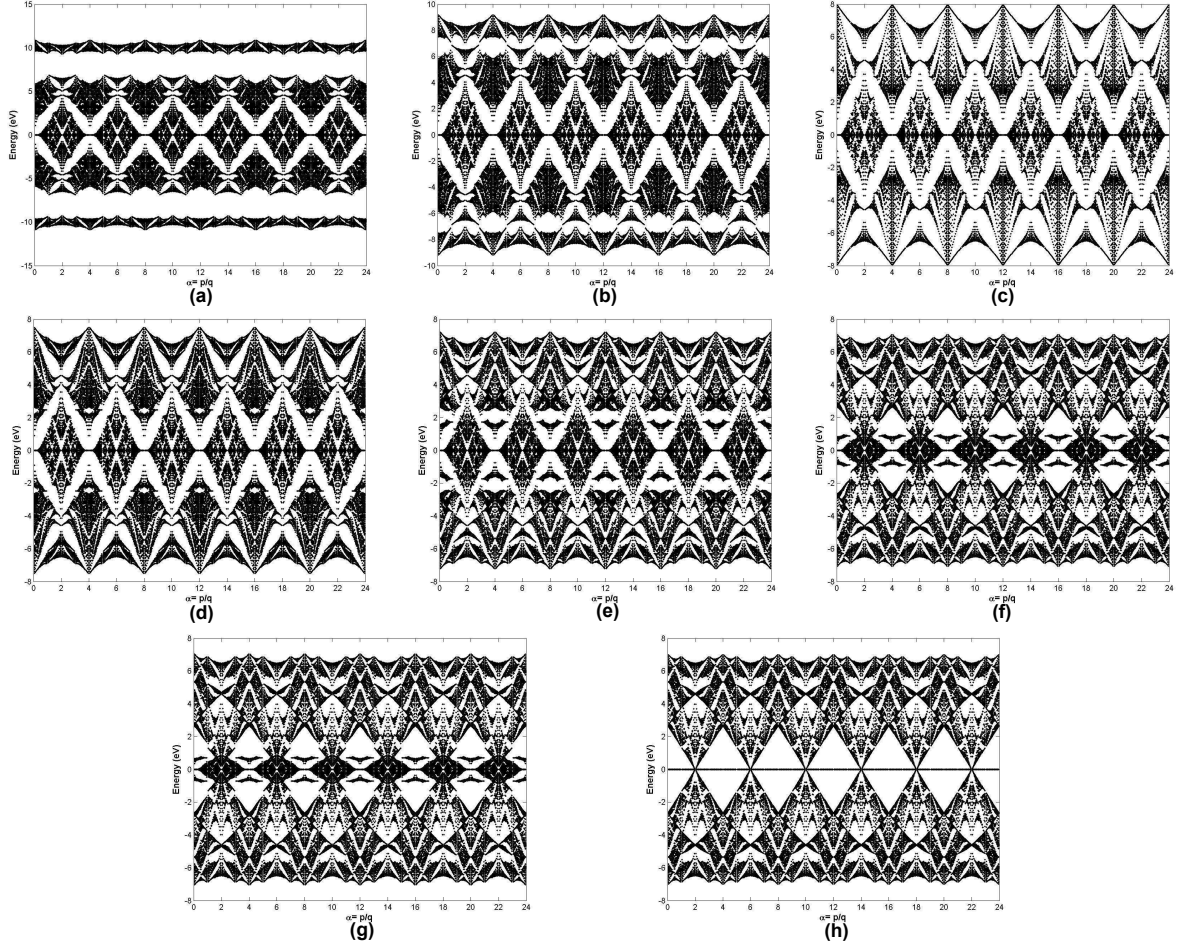
Figure 5.5: The Hofstadter Butterfly spectra of graphene with point defects with the first order interactions. **(a)** Impurity with larger hopping constant, $V_{pp\pi}^{E} = 2V_{pp\pi}$. **(b)** Impurity with large hopping constant, $V_{pp\pi}^{E} = \frac{3}{2}V_{pp\pi}$. **(c)** Pure case with all of the atoms are Carbon atoms, $V_{pp\pi}^{E} = V_{pp\pi}$. **(d)** Impurity with smaller hopping constant, $V_{pp\pi}^{E} = \frac{3}{4}V_{pp\pi}$. **(e)** Impurity with smaller hopping constant, $V_{pp\pi}^{E} = \frac{1}{2}V_{pp\pi}$. **(f)** Impurity with smaller hopping constant, $V_{pp\pi}^{E} = \frac{1}{4}V_{pp\pi}$. **(g)** Impurity with smaller hopping constant, $V_{pp\pi}^{E} = \frac{1}{5}V_{pp\pi}$. **(h)** Vacancy case where the atom "E" is missing, $V_{pp\pi}^{E} = 0$ [42].

between 3 and 4, start forming separate groups and these groups have tendencies to approach $E = 0\ eV$ line. Since the spectrum is periodic, the same structure can be observed for the values of α with a period of 4. As we reduce the hopping constant of atom "E" to one half of the usual tight-binding parameter, we observe that those groups form distinct 'bat' shaped regions within a large gap as seen in frame **(e)**. We see the similar behavior for the bands at around $E = \pm 5\ eV$. For those regions, there also new gap formations and the bands start to group. We continue to reduce $V_{pp\pi}^{E}$ to the one forth and the one fifth of the of $V_{pp\pi}$ and the corresponding spectra are given in frames **(f)** and **(g)**, respectively. For those graphs, we observe that, the central bands lying around $E = 0\ eV$ line with α is between 1 and 4 are shrank down, and the 'bat' like shaped group start to merge to $E = 0\ eV$. We also observe that, the central gaps are in approximately triangular shapes. The same sharpening of the gap boundaries can be observed for other large gaps. When we go to the limiting case, where $V_{pp\pi}^{E} = 0$ given by frame **(h)**, we obtain the vacancy case [89]. For this case, the boundaries of the central and large gaps are sharpened and they gain a more triangular shape. Also the shrank down bands and the 'bat' like shaped groups have now collapsed to the $E = 0\ eV$ line. So we see that, the new formations of gaps and bands are due to impurity atoms. As the hopping constant of this impurity atom is reduced to smaller values, these new bands are decoupled from the rest of the system. In addition to that the impurity atom reduces the scale of energy. We also remark that, these states due to the point defects (impurity or vacancy), are highly localized on the defect atoms which are not expected to contribute to the conduction. The other limit for the impurities is the case where the impurity atom has a larger hopping constant than the rest of the atoms. We start with the impurity atom located at the position of atom label "E" with stronger hopping constant $V_{pp\pi} = \frac{3}{2} V_{pp\pi}$, shown in the frame **(b)**. We see a formation of larger gaps at around E_{min} and E_{max} and bands within these regions are already grouped together. When we go one step further to frame **(a)** by fixing the hopping constant of the impurity to $V_{pp\pi}^{E} = 2 V_{pp\pi}$, we come across with the ribbon like spectra located at the top and the bottom of the original spectrum. These ribbons have their own gaps and bands and they are totally separated from the rest of the spectrum. Hence we can see that the lattice of impurity atoms with such high hopping constant produce

their own self similar Butterfly. Such a separate impurity band at the extrema of
the spectrum would be expected to modify the magnetotransport properties of
the system.

5.3.2   First and Second Nearest Neighbors

In general, the second nearest neighbor interactions bring an extra envelope-like
periodicity to the Hofstadter butterflies [88]. By implementing the next nearest
neighbor interactions into the calculations, we break the bipartite symmetry of
the lattice, hence the spectrum is no longer symmetric around $E = 0 \ eV$. The
Hofstadter butterflies with second order interactions are presented in Fig. 5.6
with the same sequence of defect atom hopping constants of Fig. 5.5. We observe
that the general characteristics of the spectra are the same and concentrate on
the differences. The gaps and bands are shifted with respect to each other, and
the central $E = 0 \ eV$ line is broken due to the loss of bipartite symmetry. We
see the same gaps and bands evolving as a function of impurity hopping constant
strengths. So we can claim that, the gaps and bands due to the impurity atom for
the first order interactions are robust to addition of the second order interactions.
For the standard second order hopping strengths as listed in Table 2.1, major
gaps in the spectrum remain open. Thus, conductance values in these major
gaps should not be effected by the second order hopping.

5.3.3   Impurity States

As the major qualitative features in the spectra calculated above are due to
impurity states we investigate the nature of these states in more detail. These
impurity states appear near $E = 0 \ eV$ for $t' < t$ ($t' = V_{pp\pi}^{E}$ is the hopping
strength of the impurity atom, $t = V_{pp\pi}$ is the hopping parameter for the rest of
the system.)and at the extrema of the spectrum for $t' > t$ as discussed. Thus we
calculate the probability distribution in real space for two states: One closest to
$E = 0 \ eV$ and one at the minimum energy. Our results are plotted in Fig 5.7(**a**)
and (**b**). For $t' > t$ (frame (**a**)) we see that the impurity state is not strictly
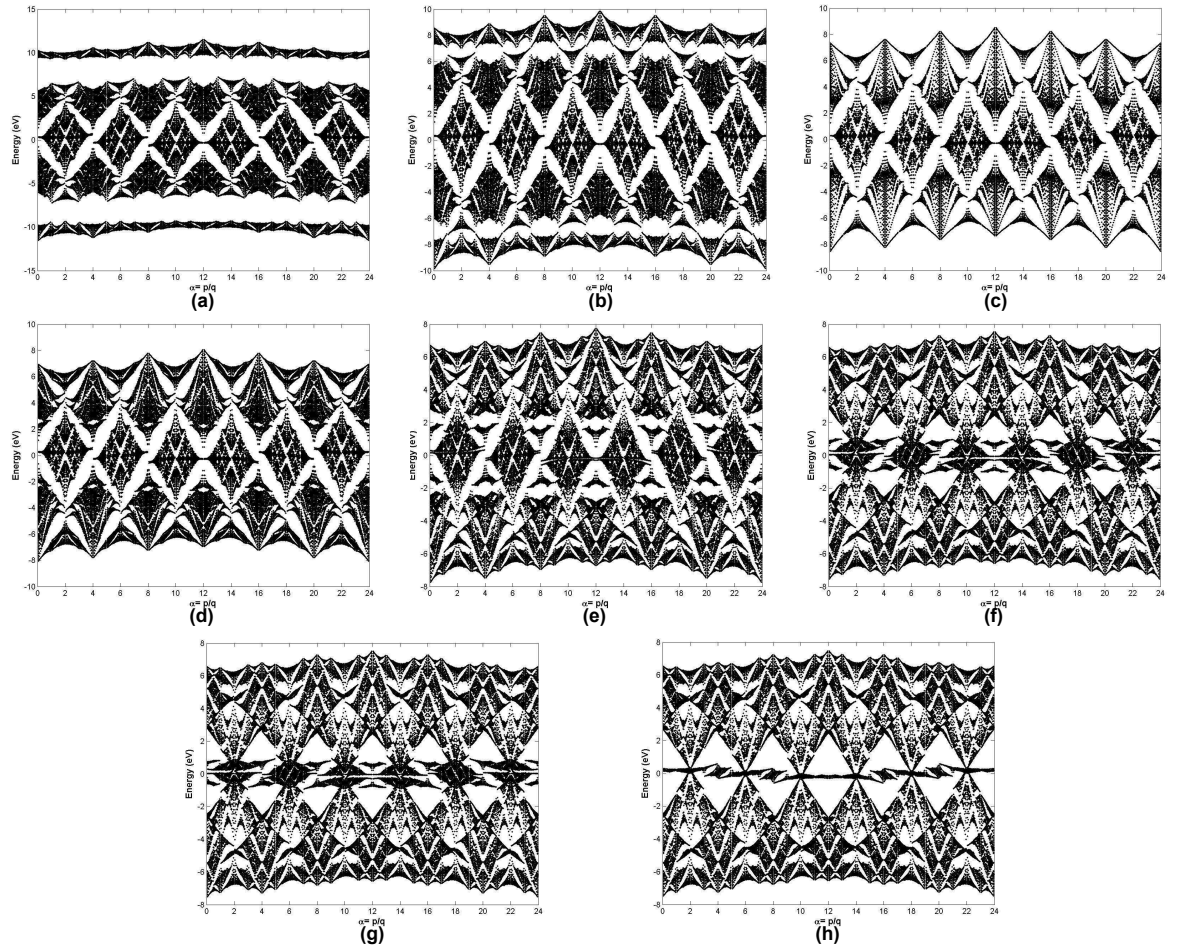
Figure 5.6: The Hofstadter butterfly spectra of graphene with point defects for the first and second order interactions. **(a)** Impurity with larger hopping constants, $V_{pp\pi}^E = 2V_{pp\pi}$, and $V_{pp\pi}^{2(E)} = 2V_{pp\pi}^2$. **(b)** Impurity with large hopping constants, $V_{pp\pi}^E = \frac{3}{2}V_{pp\pi}$, and $V_{pp\pi}^{2(E)} = \frac{3}{2}V_{pp\pi}^2$. **(c)** Pure case with all of the atoms are Carbon atoms, $V_{pp\pi}^E = V_{pp\pi}$, and $V_{pp\pi}^{2(E)} = V_{pp\pi}^2$. **(d)** Impurity with smaller hopping constants, $V_{pp\pi}^E = \frac{3}{4}V_{pp\pi}$, and $V_{pp\pi}^{2(E)} = \frac{3}{4}V_{pp\pi}^2$. **(e)** Impurity with smaller hopping constants, $V_{pp\pi}^E = \frac{1}{2}V_{pp\pi}$, and $V_{pp\pi}^{2(E)} = \frac{1}{2}V_{pp\pi}^2$. **(f)** Impurity with smaller hopping constants, $V_{pp\pi}^E = \frac{1}{4}V_{pp\pi}$, and $V_{pp\pi}^{2(E)} = \frac{1}{4}V_{pp\pi}^2$. **(g)** Impurity with smaller hopping constants, $V_{pp\pi}^E = \frac{1}{5}V_{pp\pi}$, and $V_{pp\pi}^{2(E)} = \frac{1}{5}V_{pp\pi}^2$. **(h)** Vacancy case where the atom "E" is missing, $V_{pp\pi}^E = 0$, and $V_{pp\pi}^{2(E)} = 0$ [42].
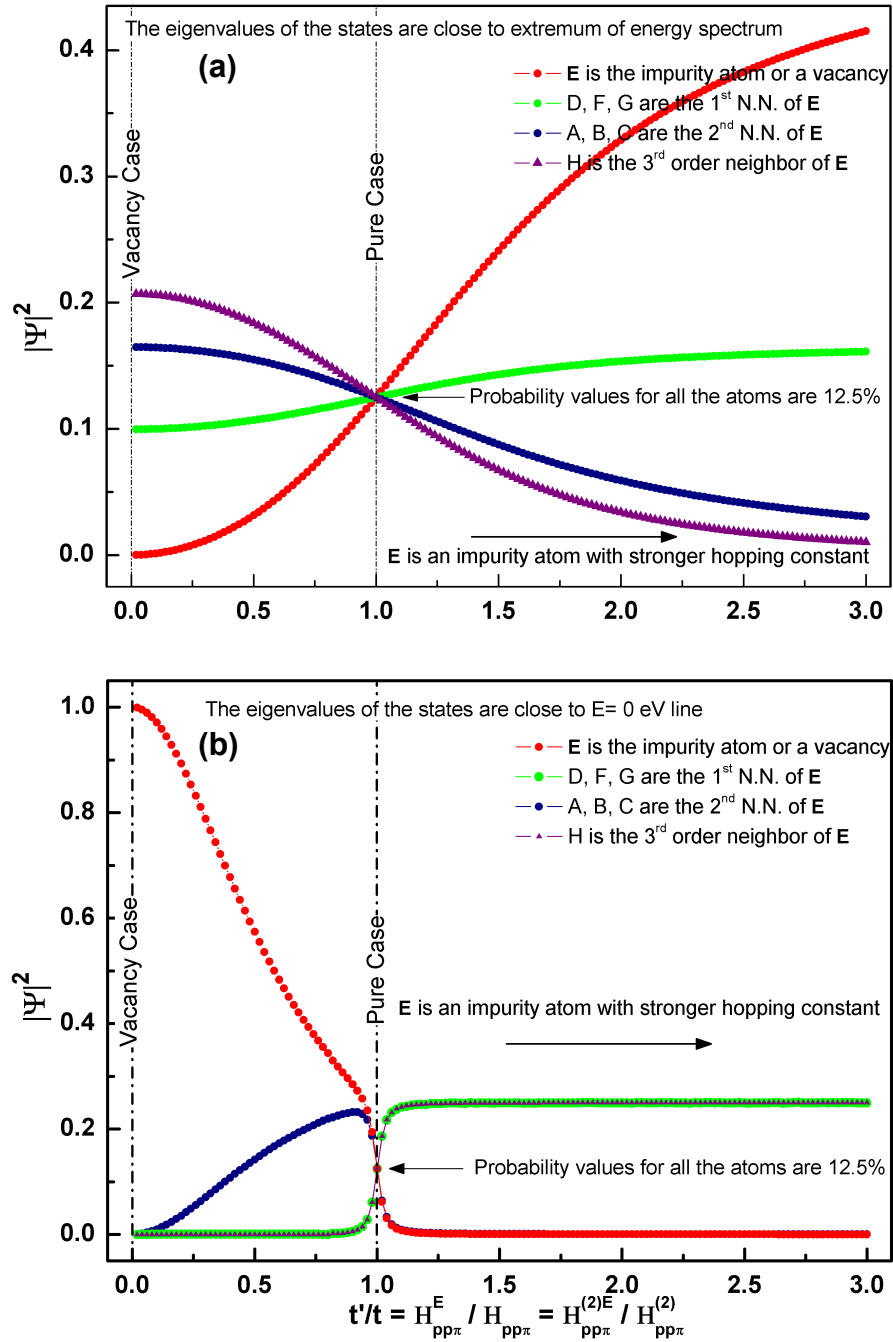
Figure 5.7: The values of $|\Psi|^2$ which give the projection of probabilities of the wavefunctions on to the atomic positions are displayed as a function of impurity hopping strengths. The parameter are set to $p = 1$ and $q = 5$, $k_x = k_y = 0$. The dotted vertical lines display the special cases: Vacancy and pure cases. **(a)** The eigenvalues for those eigenvectors are close to extremum of the energy spectrum. **(b)** The eigenvalues for those eigenvectors are close to $E = 0$ eV line. Note that there are several degenerate states near $0\ eV$ and we plot probabilities for only one of them [42].
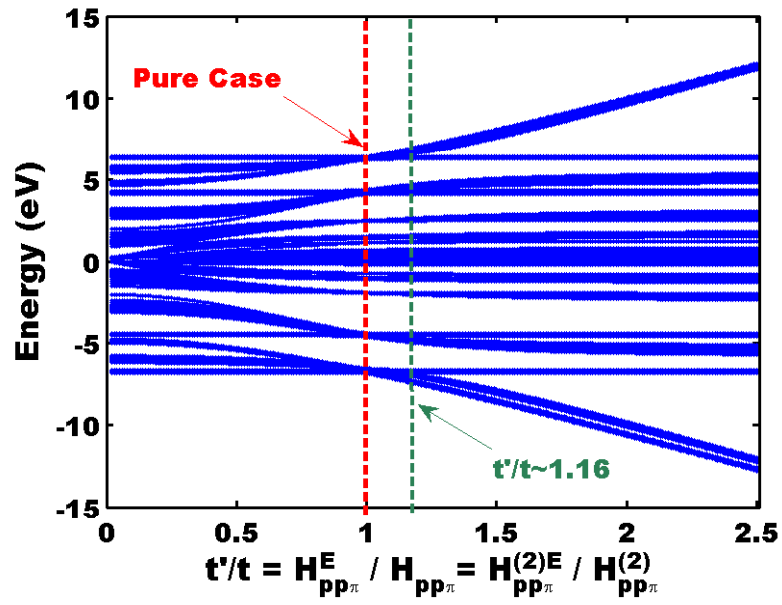
Figure 5.8: The change of band structure with respect to impurity hopping strength is displayed. The parameter are set to $p = 78$ and $q = 31$, $k_x = k_y = 0$. The pure case is represented via red dotted line, and the limiting value where the impurity bands start to leave the remaining spectrum is determined to be $t'/t \simeq 1.16$. [42]

localized on the "E" atom. In the limit of $t' \longrightarrow \infty$ the probability to be on the "E" atom is 0.5 and its nearest neighbors have probability 0.5/3 each. We see that these limiting values are asymptotically approached in Fig. 5.7(**a**). This state is separated in energy from the bulk of the spectrum forming ribbon-like structures observed in the Hofstadter Butterflies, asymptotically approaching to $\pm\sqrt{3}t'$ as seen in Fig. 5.8. For $t' < t$ (frame (**b**)) we observe rapid localization of the impurity state validating our observation regarding the spectra around $E = 0$ eV. The vacancy case merits more discussion as the impurity atom is not only decoupled from the system, but totally removed. Thus, in our calculation for the vacancy case we exclude the eigenvalue corresponding to this unphysical state from our spectra. However the absence of the atom modifies states which are not localized on the impurity but are close to 0 eV in energy. In Fig. 5.5(**h**), all the bands are closed up on $E = 0$ eV line, in contrast to Fig. 5.6(**h**) where we observe a self similar behavior of energy spectrum near $E = 0$ eV line. It is important to emphasize that the states at 0 eV in Fig. 5.5(**h**) are not unphysical impurity states but collapsed bands. The reason for this collapse is that the interactions of the remaining atoms with the *pseudo atom* cancel each other exactly for *eigenstates* respecting bipartite symmetry for the nearest neighbor case. For these states the breaking of the bipartite symmetry is especially important as their self similar nature can only be observed when their energy can deviate from 0(Fig. 5.6(**h**)).

It is important to understand the evolution of impurity states as a function of impurity hopping strengths and determine the critical values for t'/t at which major gaps open. We display the behavior of bands as a function impurity hopping strength in Fig. 5.8 including the next nearest neighbor hopping for a fixed value of magnetic field. In this figure, it is easy to discern states associated with the impurity atoms by their strong variation with the impurity hopping constant. We see that, the width of the spectrum does not change significantly between the vacancy and pure case limits. We observe modifications in the bands and creation of new gaps within this region. However when go to the strong coupling limit, two bands from the top and the bottom of the energy leave the remaining spectrum and exhibit their own self similar structures.(Corresponding to the ribbons observed in Figures 5.5 and 5.6 frames (**a**).) The critical value for the separation

is $V_{pp\pi}^{E}/V_{pp\pi} = V_{pp\pi}^{2(E)}/V_{pp\pi}^{2} \simeq 1.16$.

The reason for the self similar structure within impurity bands and gaps is that we introduce the impurities to the system in a periodic way. In reality the impurities are scattered randomly over the entire sample. For such a sample we believe that these separated bands would still exist, however the gaps and the bands would be blurred and the bands would lose their self similar structure due to the random distribution of the impurities.

In summary, we examine the effect of imperfections on the electronic structure of graphene in the presence of perpendicular magnetic field. We use the tight-binding method with both the first and the second nearest neighbor interactions are included within an enlarged unit cell. We also show the Hofstadter butterfly for pure graphene including all the orbitals. For the defect cases, the impurity atoms with smaller hopping constant(s), result highly localized states, and these states produce new gaps and bands in the energy spectra. As the hopping constant(s) of the impurity atom is reduced down to zero, we see that the bands are decoupled from the rest of the spectrum and they merge at the symmetry line where $E = 0\ eV$. So, these kind of impurities reduce the energy scale, and they mostly modify the spectrum around $E = 0\ eV$. In contrast to this case, when the impurity atom has a larger hopping constant, the bands and gaps due to the impurity atom are totally separated from the original energy spectrum. These new gaps and bands produce their own self similar collection of bands arranged into a ribbon. Such impurities also increase the overall energy scale. The second nearest neighbor interactions break the bipartite symmetry of the lattice and bring a new periodicity to the energy spectrum. The effect of impurity atoms on the energy spectrum are the same in the sense of new gaps and bands except for small shifts, when we consider the next nearest neighbor hopping.

Chapter 6

Hall Conductances for Defective Square Lattice and Graphene

6.1 Integer Quantum Hall Effect

The Hall effect was discovered and earned its name by Edwin Hall in 1878 by performing an experiment to test Maxwell's statement that the mechanical force acting on a conductor does not alter the electric current however it causes changes on the conductor itself [55]. He found out by the observation of a change in the potential difference between the lateral edges of his conductor (a gold leaf) that the magnetic field totally alters the charge distribution as well as the electric current mechanisms. This transverse voltage difference is called the Hall voltage and the Hall conductance is given by the ratio of current to the Hall voltage. In his experimental survey first he tried to test Maxwell's statement by using a metal bar which he failed, then he changed the metal bar with a gold leaf. The second choice worked well which indicates that the Hall effect is dependent on the properties of the material that is used. With a Hall setup one can examine the current carriers of specific materials.

The quantization of Hall effect under certain experimental conditions for 2D electronic systems made Klaus von Klitzing awarded the 1985 Nobel prize in

Physics. In the collaborative paper published in 1980 by Klaus von Klitzing, Michael Pepper and Gerhard Dorda [56], it is stated that in such systems the Hall conductance σ_{xy} is quantized to integer multiples of e^2/h simultaneously with vanishing longitudinal conductance, σ_{xx}, irrespective of the imperfections in the sample. It is also stated that this situation can be observed over a finite range of the parameters the magnitude of the magnetic field and the carrier concentration [57]. The quantization of the Hall conductance in the units determined by two fundamental physical quantities lead to high accuracy for defining the fine structure constant and also used in building up a new resistance standard.

It was shown by Ando [58] that the presence of an isolated impurity does not effect the Hall current. The connection of Hall conductance quantization to the nature of the states in a 2D electronic system was also appointed by Prange [59] in 1981. In his work, he demonstrated that an isolated δ-function impurity does not effect the Hall conductance. He states that the remaining delocalized states can carry enough current to compensate the loss [59]. It was then R. B. Laughlin [60] who showed the quantization can be derived from the gauge invariance of the Hamiltonian of the system. He used a model consisting of a thin metal ribbon bent into a ring in a magnetic field which is perpendicular to the surface at every point. The density of states (DOS) profile of the system without disorder displays a sequence of δ-functions each corresponding to Landau levels. If disorder is introduced to the system the δ-functions will be broadened into bands of extended states separated by localized states. In his model Ando fixes the Fermi energy in a mobility gap, i.e. located between the bands of extended states. The increasing of the flux induces a potential difference between the edges of the ring. This is simply an indicator of the charge transfer as observed in the classical Hall effect. However, the Hamiltonian of the system is gauge is invariant under the change of magnetic flux ϕ by flux quanta $\phi_0 = e^2/h$. By an increase of ϕ a flux quanta ϕ_0 the system is converted back to its initial state. However, finally a number n of electrons are transported form one edge to another of the ring in accordance with increase of the potential difference between the edges. As a result one cycle of the pump transferring n electrons is the adiabatic change in the flux by one flux quantum. Ando also stated that, the change in the total electronic energy

of the system induced by a cycle of the pump ($\phi \rightarrow \phi + \phi_0$) is due to forcing of the filled states toward one edge of the ribbon. If all the states in the system are localized states, then there will be no change in the total electronic energy of the system. They are the extended states which are responsible for the integer quantization of the Hall effect [57, 60].

The localization and non-localization nature of the states was developed by Anderson [61]. He demonstrated that if a quantum mechanical system is disordered enough, the states will be *localized* in space. For the electrons in those systems, the mean free path is shortened due to disorder and the hopping of electrons is blocked for the limiting case. From this point of view, the localization length can be considered as the decaying and eventually vanishing of the electrons transmission probability. However, for a slightly disordered system there might be some states remaining which are considered to be *extended states*, through which the transmission still exists. These kind of states contribute to the conduction even at zero temperature. The extended and localized states are separated from each other at the boundaries by mobility edges at where the nature of the states can not be deduced either localized or extended. The theory of localization for the non-existence of the extended states in 2D contradicts with the experimental and calculation results of the Integer Quantum Hall Effect (IQHE). Later it was shown that the strength of magnetic field is responsible for the occurring extended states, hence the non zero values for Hall conductance [62, 63]. The Hall conductance changes its value when it passes through mobility edges, it displays a stair-like behavior with sharp steps positioned at the single values energy belonging to the mobility edges [64]. Through the constant valued plateaus the system is considered to be in an insulating phase. Among these regions the longitudinal conductivity σ_{xx} vanishes and the Hall conductance σ_{xy} is quantized.

There are various ways to calculate the Hall conductance. When the Fermi level is in an energy gap, the value of the Hall conduction is expressed in terms of the famous Thouless-Kohmoto-Nightingale-den Nijs (TKNN) integers [44, 65] times e^2/h. The whole picture for the conductance can be calculated by either Streda [66] formula originating from the linear response theory, or by the Kubo formalism. Several works have been published which have concentrated both

on the Hall conduction and the Hofstadter Butterflies for the cases of square, triangular, kagomé and honeycomb lattices [37, 67, 68, 69, 70, 71, 72, 73, 74, 75, 76]. In this thesis, we used the Kubo formula to calculate the value of the Hall conductance continuously regardless of Fermi energy lying in a gap or in a band for a single value of $\phi/\phi_0 = p/q$ [44, 65]:

$$\sigma_{xy} = \frac{ie^2}{A_0\hbar} \sum_{E_\alpha < E_f} \sum_{E_\beta > E_f} \frac{(\partial \hat{H}/\partial k_x)_{\alpha\beta}(\partial \hat{H}/\partial k_y)_{\beta\alpha} - (\partial \hat{H}/\partial k_y)_{\alpha\beta}(\partial \hat{H}/\partial k_x)_{\beta\alpha}}{(E_\alpha - E_\beta)^2},$$
(6.1)

where A_0 is the area of the plaquette, the energies with indices α and β denote the energies of the states with lower and higher than the Fermi energies, respectively. The values of k_x and k_y span the magnetic Brillouin zone which is the reciprocal of the magnetic unitcell. This is a more general way of Hall conductance calculation where the method of Diophantine equation fails for the systems with impurities and even for graphene. In general the Diophantine equation associated to the rth gap of the energy spectrum is given as a function of two integers with a fixed value of $\phi/\phi_0 = p/q$:

$$r = pt_r + qs_r,$$
(6.2)

with a constraint specific to the lattice for the absolute value of the integer t_r. For square lattice this constraint is $t_r \leq q/2$ and each gap has an integer invariant "Chern number" which has a connection to Diophantine equation via $C_s = -t_r$ [77]. However, for graphene the validity of the constraint is already vanished even for the pure graphene, so the Chern numbers should be calculated by numerically or by Kubo formalism which gives the Hall conductances for all values of the Fermi Energy.

6.2   Topology in Hall Conductance

In 2D electronic systems the Brillouin zone is also confined into two dimensions. The real space lattice points on which the atoms are positioned can be represented in terms of the cartesian coordinates, the Brillouin zone due of this lattice is

the reciprocal lattice of the real lattice. The coordinates are determined by the reciprocal lattice vectors which simply span the values of the wavevectors k_x and k_y. This Brillouin zone in 2 dimensions can be regarded as a 2-torus $\mathbf{T}^2$. The eigenstates come as the solutions to the Harper's equation can be considered as the principle fiber bundles.

The First Chern numbers are the topological invariant integrals of the $U(1)$ fiber bundles formed by the wave functions over the magnetic Brillouin zone, i.e. they remain invariant under small deformations of the curvatures. For the special case of edge states, they describe the number of *windings* of a fiber bundle (edge state) over the manifold, base space . This can be related to the quantum mechanics. The Berry's phase rise up due to the curvature of the parameter space. If we transport an eigenstate adiabatically through a loop in the parameter space (our parameter space contain the magnetic flux and the chemical potential for instance) it will end up with the physically same state however the wave function will gain a phase factor. As it is mentioned before the probability of finding the particle in either of the states will remain the same since the phase factors have the structure $e^{i\theta}$ where $\theta \in \mathbf{R}$. The loop in the parameter space can be visualized as an intersection of two areas: The area inside the loop and the area surrounding the loop. The phase mismatch due to the parallel transport is given by the integrals of the curvatures through the area inside and area outside simply related to the Chern numbers [35]. Let us assume that the eigenstate has a phase $e^{i\theta_1}$ after transporting around such a loop in clockwise direction. If we transport our initial eigenstate in the counter-clockwise direction it will have another phase $e^{-i\theta_2}$, where the minus sign appears due to the oppositeness of the transportation direction. Since the state itself does not change at all during this kind of transportation, $e^{i\theta_1} + e^{i\theta_2} = 1$ urging that $\theta_1 + \theta_2 = 2\pi \times n$, where $n \in Z$. This integer multiple n is simply the first Chern number. The reason why n being an integer is behind the fact that the eigenstate must turn to itself after accomplishing a loop adiabatically in the parameter space. Otherwise, the initial eigenstate will be converted to other physical state. Another reason for the Chern numbers to be integers is that Chern class is an integer valued linear map through its mathematical definition.

As we mentioned above, we use the Kubo formula (Eq. 6.1) for the Hall conductance. The topological aspect of Hall conductance can also be visualized through this equation. The wavefunctions $\psi_\alpha(\vec{k})$ are indeed composed of an exponential factor function of the reciprocal lattice vectors k_x and k_y and a periodic function $u_{k_x k_y}(x, y)$ which carries the gauge information. We choose Landau gauge through the vector potential is given in y direction. Under these circumstances, the periodic function is periodic in y direction. Now, let us translate this wavefunction first parallel to k_x direction by $\vec{G}_1$. Since k_x and k_y both lie in the first Brillouin zone, only the transformations with the reciprocal lattice vectors $\vec{G}_1$ and $\vec{G}_2$ will enhance the periodic part of the wavefunction $u_{k_x k_y}$ by a phase factor:

$$u_{k_x k_y + \vec{G}_1} = e^{i\delta(k_x + \vec{G}_1)} u_{k_x k_y};$$

since in x direction q times periodicity atoms are connected, as a consequence of magnetic unit cell. Now, let us translate in k_y direction by $\vec{G}_2$:

$$u_{k_x k_y + \vec{G}_2} = e^{i\delta(k_x)} u_{k_x k_y},$$

where translating along k_y direction is independent of k_y due to the definition of u. These two consecutive translations regardless of their turn should end up with the matched phase factors as:

$$\delta(k_x + \vec{G}_1) = \delta(k_x) + 2\pi n,$$

where n is an integer [78].

If the phase of the state $|\varphi_\alpha(\vec{k})\rangle$ is well defined through the Brillouin zone such that there are no boundaries in the Brillouin zone, then the Hall conductance yields 0. As a consequence of that one can propose the energy band $E_\alpha(\vec{k})$

associated to the state $|\varphi_\alpha(\vec{k})\rangle$ does no contribute to the Hall conduction. The states corresponding to this case are the localized states. The Chern numbers, as well as the Hall conductance are not altered by localized states. The zero's of these kind of wavefunctions are confined in space [57]. Since the Chern numbers are topological invariants they are robust to small deformations of the Hamiltonian. As a result of that the Hall conductance displays constant values (plateaus) through the region of localized states, they have step-like sharp changes in between theses plateaus. In addition to that, due to Chern numbers being integers they do not change smoothly. The non-zero values of the Hall conduction occurs when the phase of the state $|\varphi_\alpha(\vec{k})\rangle$ can only be determined on some open subsets on the base space i.e. $\{U_1, U_2, ..., U_k\}$. The non-triviality of the wavefunctions and in other words the phase ambiguity of the wave functions over the magnetic Brillouin zone is responsible for the non zero values of Hall conductance [77, 79, 80]. The states associated with this definition are the extended states. They are the states which contributing to Hall conductance, such that they are the ones which carry the Hall current. The Chern numbers have their jumps between successive integer values through these kind of states. In the systems that are studied in this thesis, have the structure that, each Landau Band has the extended states at the center of the band which are separated by continuum of localized states.

6.3 Hall Conductances for Defective Square Lattice

In solid state experiments, its now a standard method to measure the Hall conductance by a four terminal strip. In a cold atom setting, in general, such methods are unavailable as there is no way to make contacts to the cold atom system. One way to overcome this difficulty is to make a scattering type of measurement by letting the cold atom cloud oscillate in a shallow external trap [90]. However, as long as the quantized Hall conductances are concerned, it has been shown that measuring the response of the density of the system to the external magnetic field yields a direct measurement of the Hall conductance by the virtue of Streda
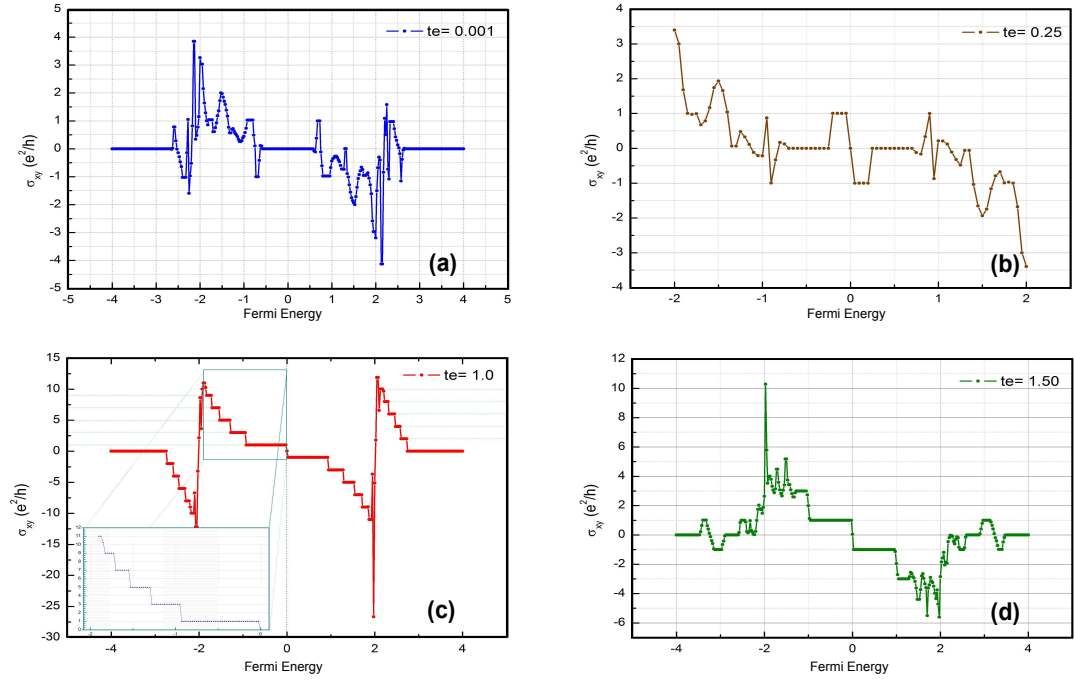
Figure 6.1: Hall conductivities (in the units e^2/h) as a function of Fermi Energy (in the units of "t") with the 1st order interactions where α is set to $p/q = 13/3$: **(a)** "E" is an impurity with $t_E = 0.001$. **(b)** "E" is an impurity with $t_E = 0.25$. **(c)** All of the atoms are the same with $t_E = t = 1.00$. (inset) The region of the spectrum enclosed by a rectangle is zoomed in. **(d)** "E" is an impurity with $t_E = 1.50$ [43].

formula [91]. Thus, in both cases the effects of impurities on the conductance should be experimentally accessible. Hence, it is important to calculate the Hall conductance in an impure system to understand these experiments. The Hall conductance of the square lattice over all energy values whose range is given by the Hofstadter Butterfly can be calculated by using the Kubo formula [44] for a single value of $\phi/\phi_0 = p/q$:

$$\sigma_{xy} = \frac{ie^2}{A_0\hbar} \sum_{E_\alpha < E_f} \sum_{E_\beta > E_f} \frac{(\partial \hat{H}/\partial k_x)_{\alpha\beta}(\partial \hat{H}/\partial k_y)_{\beta\alpha} - (\partial \hat{H}/\partial k_y)_{\alpha\beta}(\partial \hat{H}/\partial k_x)_{\beta\alpha}}{(E_\alpha - E_\beta)^2},$$

(6.3)

where the velocity operators are defined as the partial derivatives of the Hamiltonian with respect to wave vectors. In addition to two summations for the energy
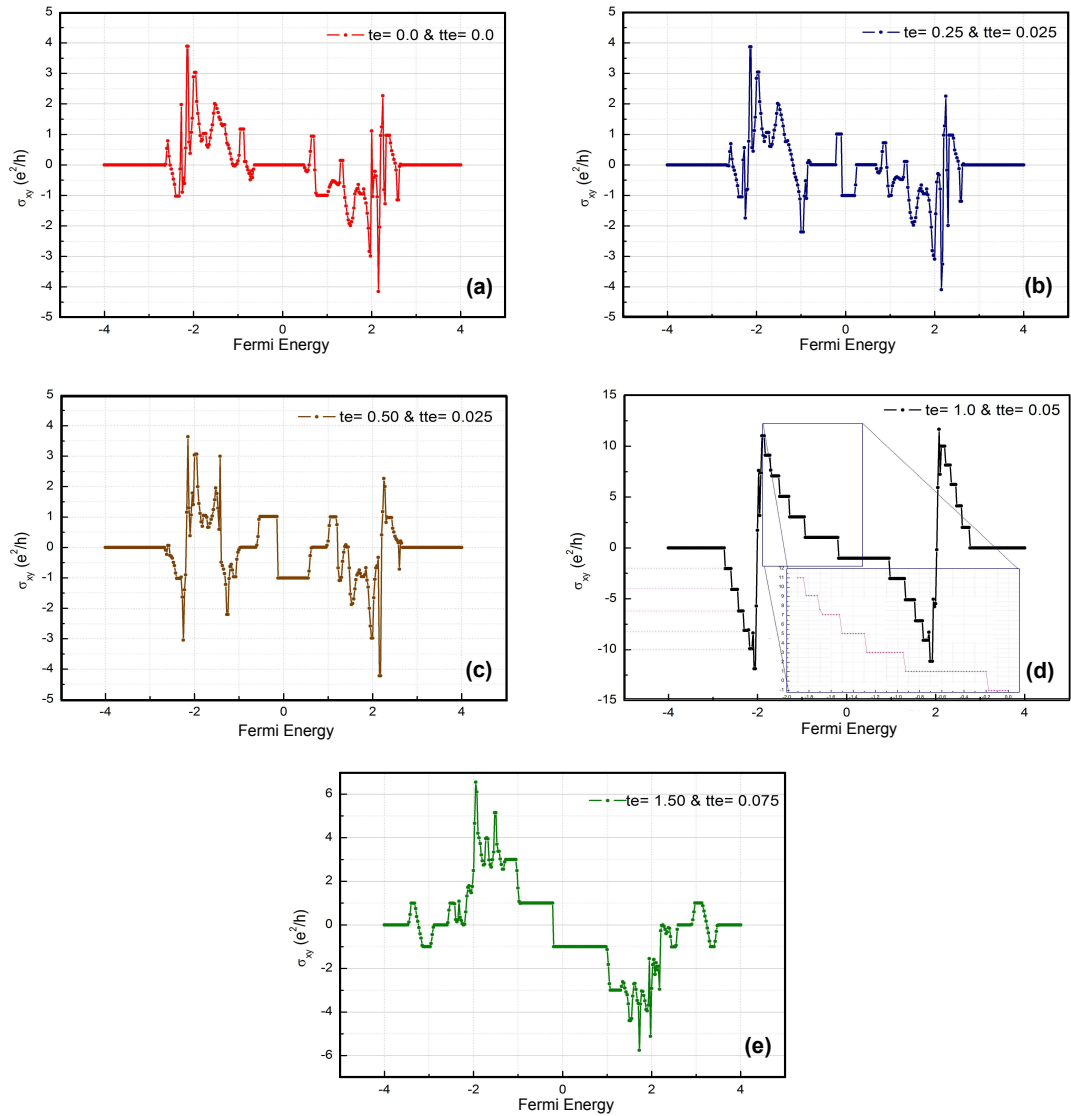
Figure 6.2: Hall conductivities (in the units e^2/h) as a function of Fermi Energy (in the units of "t") with the 2nd order interactions where α is set to $p/q = 13/3$: **(a)** "E" is a vacancy with $t_E = 0.0$ and $tt_E = 0.0$. **(b)** "E" is an impurity with $t_E = 0.25$ and $tt_E = 0.025$. **(c)** "E" is an impurity with $t_E = 0.50$ and $tt_E = 0.025$. **(d)** All of the atoms are the same with $t_E = t = 1.00$ and $tt_E = tt = 0.050$. (inset) The region of the spectrum enclosed by a rectangle is zoomed in. **(e)** "E" is an impurity with $t_E = 1.50$ and $tt_E = 0.075$ [43].

eigenvalues smaller than and greater than the fixed Fermi energy respectively, there is another implied summation over the whole magnetic Brillouin zone. Although, the Hall conductance in a gap for a pure system can be calculated via the Diophantine equation which results the famous TKNN integers [44], in the impurity case the calculation does not simplify to a Diophantine equation. So we calculate the Hall conductance explicitly through the Kubo formula, Eq. (6.6). When the Fermi energy lies within a gap, we find that the Hall conductance is an integer multiple of e^2/h, verifying our numerical procedure. Kubo formula also allows us to calculate the Hall conductance even when Fermi energy lies within a band.

The sweeping of Fermi energy is an indirect representation of the potential difference that should be present in the system in order to observe a non zero conduction. The similar procedure was carried for the triangular and Kagomé lattice under the influence of staggered magnetic field, and also for the square lattice with multiorbital interactions [69, 70].

The Hall conductances for various impurity cases (with the same impurity concentration displayed in Chapter 4) are displayed as a set in Fig. 6.1. These graphs show Hall conductances in the units of e^2/h, as a function of Fermi energy for the single value of $\alpha = \phi/\phi_0 = p/q = 13/3$ calculated as above. Again we have the pure case with $t_E = t = 1.0$ labelled by (c), in which we see the usual step like quantized integer Hall conductance. It is symmetric around Fermi energy $E_{Fermi} = 0$, and we observe successive integer sequence of conductance in agreement with the Diophantine equation of the Hofstadter Butterfly. When we look at the conductance spectrum in frame (b) where t_E is set to $t_E = 0.25$, we see a deformed conductance, however we can see the constant conduction Hall plateaus around $E_{Fermi} = 0$. We observe new Hall plateaus with Hall conductance $\sigma_{xy} = 0$ centered at $E_{Fermi} = \pm 0.5$ which are within the dome shaped gaps discussed in Hofstadter spectrum. For the case of $t_E = 0.001$ (frame a), we see that the $\pm e^2/h$ conductance plateaus for $E_{Fermi} = \pm 0.5$ are narrowed down as the dome shapes become more elliptic. Under these circumstances, a vacancy or an impurity with a smaller hopping constant in the unit cell bears new states that are highly localized on the defect atom. These localized states can not

contribute to the conduction, significantly. By setting the hopping parameter of the atom "E" to a value smaller than the rest of the atoms in the unit cell, we are disabling (or blocking for the vacancy case) the hopping of the electrons through this defect atom. The norm of a representative wavefunctions of $E = 0$ energy is plotted through a cut through the magnetic unitcell in Fig. 4.9. The two plots for $t_E = 0.005$ and $t_E = 0.50$ demonstrate the localization of the impurity states as t_E is decreased. We see that, the wavefunctions are highly localized on the point defect. When the impurity is strongly coupled, i.e. $t_E = 1.50$, the main change in the spectrum was observed near the extremal energies due to presence of new gaps. These impurity gaps have Hall conductance $\pm e^2/h$ as shown in Fig. 6.1(d). We can infer an impurity atom with higher hopping constant interacts more with the neighboring atoms creating a delocalized impurity state as a result of which new constant conductance Hall plateaus are created.

The Hall conductances for different impurity scenarios in the presence of the next nearest neighbor interactions are given in Fig. 6.2. The Hall conductance spectra are no longer symmetric around $E_{Fermi} = 0$, as bipartite symmetry is broken. The widths of the gaps are now changed, when we look at the energy spectrum along a vertical line which has $\alpha = p/q = 13/3$. Second order interactions do not change the nature of the impurity states. They are highly localized and do not contribute significantly to the conductance. Similarly for an impurity atom with a high hopping constant, the new conduction plateaus with conductance $\pm e^2/h$ are also robust with respect to the next nearest neighbor hopping. When magnetic bands of the Hofstadter Butterfly are extremely narrow, our direct calculation through the Kubo formula requires extremely fine k-point meshing. Thus, in regions with many small gaps, our results show scattered values for conduction. However, such fine meshes are not required for the calculation of conduction within large gaps or for impurity states.

6.4 Hall Conductances for Defective Graphene

6.4.1 Anomalous Integer Quantum Hall Effect in Graphene

A special case of IQHE is the Anomalous Integer Quantum Hall effect which can be observed in graphene. Graphene displays different Hall conductance behaviors through the Fermi energies that spans the energy window for high magnetic fields. For pure graphene, the energy spectrum is symmetric around $E = 0$ eV. This symmetry is a common result for the systems which have a bipartite symmetric lattice. The energy eigenvalues come as pairs $(E, -E)$. The bipartite symmetry is a result of the situation when the lattice can be considered as a union of two sublattices. In addition, all the interactions take place between these two sublattices, i.e. only inter-sublattice interactions. Since graphene has 2 atoms in its basis, its lattice can be thought of a composition of two sublattices belonging to two kinds of atoms. When we look at the Hall conductance plot as a function of Fermi energy (by use of bipartite symmetry, from $E = E_{max}$ to $E = 0$ eV) in graphene we see that there are two Hall conductance regimes separated by van Hove singularity regions. Starting from $E = E_{max}eV$ to van Hove singularity region the usual IQHE is observed. The Hall conductance takes values with $\sigma_{xy} = 2ne^2/h$ with $n = ..., 3, 2, 1, 0$. However beyond this region to $E = 0$ eV there is distinct character of IQHE where $\sigma_{xy} = 2(2n + 1) \times e^2/h$ with $n = ..., 3, 2, 1, 0$. The factor 2 arises due to the spin degeneracy. The reason for this anomalous behavior is the Dirac fermions in graphene.

When there is a magnetic field acting on 2D electronic system with a Bravais lattice, the energy levels are quantized in a series of equally spaced Landau levels for the motion of particles acting perpendicular to the field:

$$E_n = E \pm \hbar w_c(n + 1/2), n = 0, 1, 2, ... \tag{6.4}$$

where w_c is the cyclotron frequency. These systems can be described by non-relativistic quantum mechanics where the Schrödinger equation is satisfied. However, the lattice structure of graphene is different. It has non-Bravais lattice composed of two triangular Bravais lattices. The band structure of graphene displays

Dirac cones of conduction and valance bands touching each other at Dirac points. These bands have linear dispersion where $E = \pm v_F \hbar k$ with v_F is the Fermi velocity. Energy being linearly dependent on the velocity turns the non-relativistic quantum mechanical system into a relativistic quantum mechanical system. The Schrödinger equation is not satisfied any more but the Dirac equation is the equation through the system is defined. The Dirac points occur due to the internal degrees of freedom which cause a chirality. The solutions to the Dirac equation governing the system come as pairs with opposite chiralities: Particle and antiparticle pairs. As a result of that, the Landau level spectrum is changed with respect to Eq. 6.4.:

$$E_n = sgn(n)\sqrt{2e\hbar v_F^2 |n| B}, n = ..., -2, -1, 0, 1, 2, ... \tag{6.5}$$

The Dirac fermions with a Berry's phase π result the shifting of Hall conductance values leading Anomalous Integer Quantum Hall Effect. However since the Hall conductance plot (Fermi energy vs. Hall conductance) shows two distinct regimes for graphene, the Dirac equation can not be generalized for all the Fermi energy values in the energy window. The explanation above stays valid up to van Hove singularities where the bands have saddle points and as a result of that they intersect the Brillouin zone boundaries perpendicularly. Beyond that region the system is characterized by Schrödinger equation [19, 42].

6.4.2 Hall Conductances for Graphene and Defective Graphene

Graphene, after the isolation as single layer by mechanical exfoliation [2, 4], is one of the mostly studied systems in recent years. Graphene exhibits several unusual properties because of the Dirac points constituent of its band structure. For example, the unconventional quantum Hall effect was predicted in earlier calculations [12, 13]. Soon after the discovery of the anomalous integer quantum Hall effect in graphene [5, 14], many theoretical studies discussing the Hall
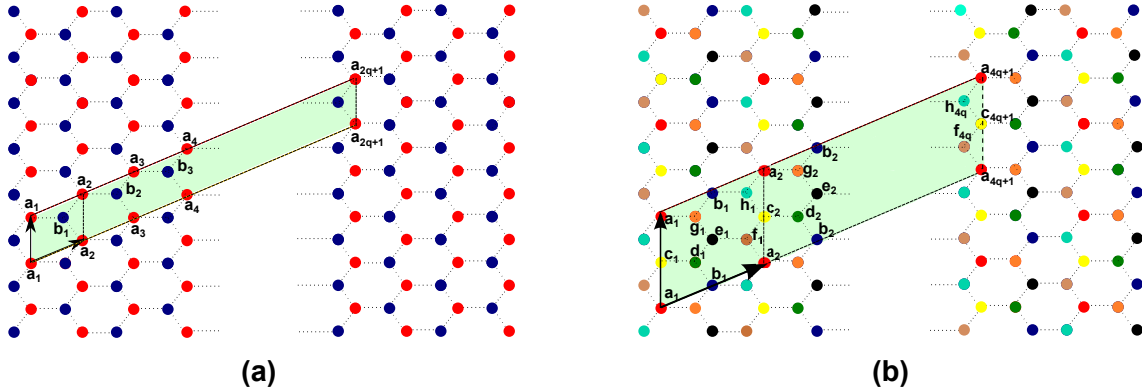
Figure 6.3: **(a)** Magnetic unit cell of graphene, in which $4q$ atoms are connected. The unit cell with basis of two atoms is indicated within the smaller parallelogram. **(b)** Larger magnetic unit cell of graphene suitable for point defect calculations through which $32q$ atoms are connected. The unit cell has eight atoms in the basis shown within the boundaries of smaller parallelogram, and the atom with label "**e**" is the defect atom.

conductance in low magnetic field regime were reported [15, 16, 17, 18, 19]. Yasumasa Hasegewa and Mahito Kohmoto calculated the Hall conductance for the plateaus from the Streda formula [15]. They found the Hall conductances are given by $\sigma_{xy} = 2ne^2/h$ with $n = ..., 3, 2, 1, 0$, in the high magnetic field regime where the additional factor of 2 arises from the spin degeneracy. In this paper, we follow the tight-binding approximation for the honeycomb lattice in the presence of magnetic field. After the diagonalization of the Hamiltonian, we use the corresponding eigenvalues and the eigenvectors in the Kubo formula to calculate the Hall conductance. We come up with $\sigma_{xy} = 2ne^2/h$ with $n = ..., 3, 2, 1, 0$ for high magnetic field limit. Similarly, in the lower magnetic field regime, we observe the anomalous integer quantum Hall effect given by $\sigma_{xy} = 2(2n + 1) \times e^2/h$ with $n = ..., 3, 2, 1, 0$. Our results for pure graphene are in accordance with experiments and previous calculations.

However, no real sample is defect free. Even in the cleanest material there are point defects like impurities or vacancies. These defects might be introduced intentionally in order to improve some materials property [92, 93, 94, 95]. Therefore, it is essential to understand the effect of these defects on properties like

magnetoconductance. Here, we investigate in detail the evolution of conductance with respect to presence of point defects such as vacancy and impurity atoms in graphene. The effect of uniform on-site disorder on graphene quantum Hall effect was investigated on a graphene ribbon [96]. A disorder model more relevant to graphene can be constructed by explicitly introducing impurities with modified hopping strength in a supercell approach. In this chapter, we present such a model in which we obtain a 12.5% concentration by treating one atom as a point defect out of eight atoms in the enlarged unit cell. By altering the hopping constant(s) of this impurity atom, we model different impurity atoms in graphene, and by setting the hopping constant(s) to 0, we model the vacancy case. We show that, the impurity atoms with smaller hopping constant than the rest of the atoms result in highly localized states which do not provide contribution to Hall conductance. However, the impurity atoms with higher hopping constant produce delocalized states which form their own bands.

The section is organized as follows: In the following subsection, we summarize the Kubo formalism for the calculation of the Hall conductance for pure graphene. Then we model graphene with point defects. Lastly, we discuss the Hall conductances for perfect and imperfect graphene.

Pure Graphene

Graphene has a honeycomb lattice structure with two atoms in its unit cell. The bond distance is 1.42 Å, and each atom has 3 nearest neighbors. We considered the isotropic case, in which the hopping parameter for the p_z orbitals interacting with the nearest neighbors is equal to -2.66 eV, and -0.1 eV for the next nearest neighbors [46].

When the well known tight binding method is applied with the Peierls substitution [53] for the Landau gauge $\vec{A} = (0, Bx, 0)$ we end up with the Harper's equation [54]. By applying the Bloch condition Harper's equation is written as an eigenvalue equation where the $4q \times 4q$ A_m matrix is the Hamiltonian. The elements of this matrix are composed of the interactions over the entire magnetic

unit cell, shown in Fig. 6.3(a).

The amount of flux per unit cell is given by $\phi = \frac{p}{q}\phi_0$, where the flux quantum $\phi_0 = h/e$. We consider the cases for which p and q are mutually prime integers. The system has a new unit cell under the magnetic field, which is called the magnetic unit cell. In this unit cell, due to the magnetic periodicity, and the basis, now $4q$ atoms are connected as shown in Fig. 6.3**(a)**. We have new lattice vectors for this case, which have lengths depending on the parameter q. As we increase q, our magnetic unit cell is enlarged as opposed to the magnetic Brillouin zone. Increasing q has another consequence such that, it yields lower magnitude for the magnetic field. Since we have to solve eigenvalue equations among the whole Brillouin zone, increasing q brings computational cost for the diagonalization, however our magnetic Brillouin zone scales down with q, requiring summation over less k-points. The eigenvalues of the A_m matrix are the energy eigenvalues, which yield the Hofstadter butterflies for graphene as a function of flux $\alpha = p/q$ [36, 40].

Once the eigenvalues and corresponding eigenstates are obtained, Hall conductance can be calculated from the Kubo formula [44]:

$$\sigma_{xy} = \frac{ie^2}{A_0\hbar} \sum_{E_\alpha < E_f} \sum_{E_\beta > E_f} \frac{(\partial \hat{H}/\partial k_x)_{\alpha\beta}(\partial \hat{H}/\partial k_y)_{\beta\alpha} - (\partial \hat{H}/\partial k_y)_{\alpha\beta}(\partial \hat{H}/\partial k_x)_{\beta\alpha}}{(E_\alpha - E_\beta)^2}.$$

(6.6)

The derivative expressions are the velocity matrix elements. The sums over energies above and below the Fermi energy also imply a summation over the magnetic Brillouin zone. The energy eigenvalues are grouped into occupied (α) and unoccupied (β) states. So, by changing the Fermi energy we can calculate the Hall conductance for a given system. This sweep of Fermi energy corresponds to the change in the gate voltage in the usual quantum Hall experiments. Similar calculations based on this approach have been carried out for other lattice geometries [69, 70].
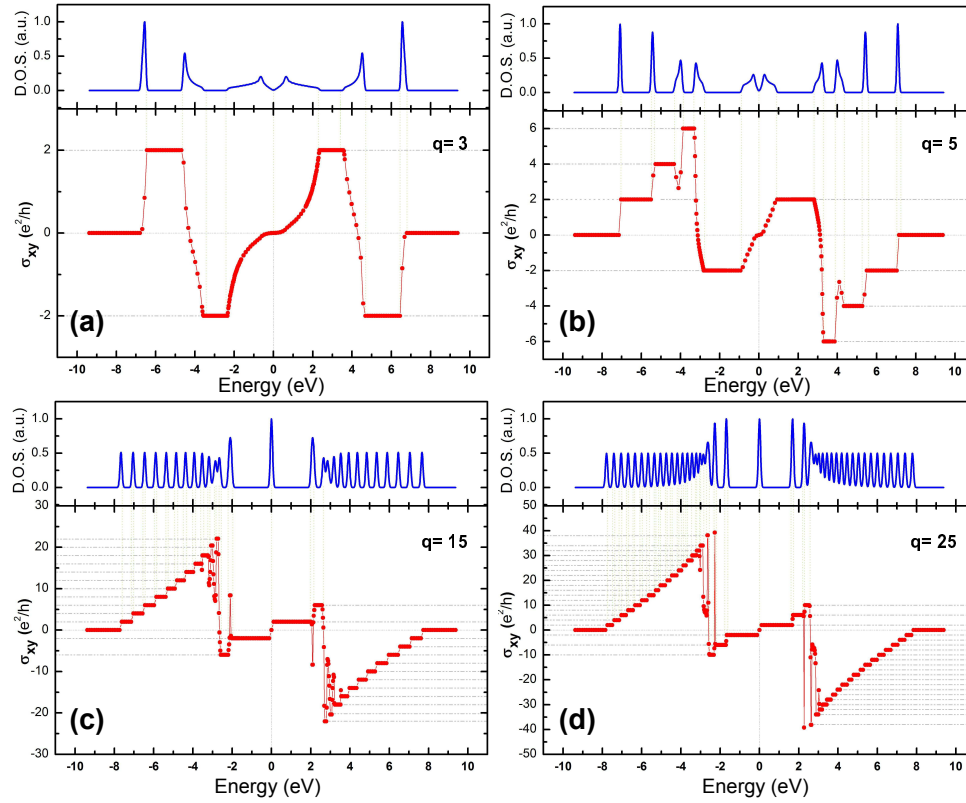
Figure 6.4: **(a)**The Hall conductance spectrum for graphene with $q = 3$ and $p = 1$. The plateaus have the constant conductances proportional to $n \times e^2/h$, where $n = +2, -2, +2, -2, 0$. **(b)** The Hall conductance spectrum for graphene with $q = 5$ and $p = 1$. The plateaus have the constant conductances proportional to $n \times e^2/h$, where $n = +2, +4, +6, -2, +2, -6, -4, -2, 0$. **(c)** The Hall anomalous conductance spectrum for graphene with $q = 15$ and $p = 1$. The plateaus around $E_F = 0$ have the constant conductances proportional to $n \times e^2/h$, where $n = -6, -2, +2, +6,$. The steps have conductance values as a set of even integers. **(d)** The Hall anomalous conductance spectrum for graphene with $q = 25$ and $p = 1$. The plateaus around $E_F = 0$ have the constant conductances proportional to $n \times e^2/h$, where $n = -10, -6, -2, +2, +6, +10$. The insets are the density of states data.

Graphene with Point Defects

In the previous subsection we assume that graphene has a defect free structure. However, in real world any material has defects such as impurity atoms and vacancies. These imperfections may appear in the crystal structure naturally, also might be deliberately introduced [97, 98, 99, 100, 101]. We model a defect atom by changing its hopping constant(s). If one of the atoms in the usual basis of graphene with 2 atoms is modified we end up with a composite structure like an alloy with a concentration of 50%. In order to reduce this concentration to reasonable values, we use a 2×2 unit cell as shown in Fig. 6.3(**b**). Thus with this enlargement we obtain a defect concentration of 12.5%. The defects in our system

are well separated (~ 10 Å) but form a regular lattice.

The natural defects are of course randomly scattered throughout the sample. However, as long as the defect concentration is low, the main effect of defects on transport is through their action as individual scatterers. Thus in this paper, we model the impure system by considering a regular lattice of point defects as explained above. As long as the point defects create states which are well localized, they can be modelled by enlarging the unit cell [102]. Furthermore, the Hall conductance is a very robust physical quantity as it can be related to certain topological invariants [44, 17, 60, 103]. We expect our model closely represents the properties of randomly scattered impurities as long as the conditions above are met.

The enlarged unit cell is shown in Fig. 6.3(**b**). The smaller parallelogram in which the atoms are labelled $a, b, c, ..., h$ and index 1 is the enlarged unit cell. The tight-binding procedure is similar to the usual unit cell of graphene, however since we have 8 atoms, our Hamiltonian is now an 8×8 matrix. All the elements of this matrix contain the p_z orbital interactions between the first nearest neighbors and the second order neighbors, if necessary. The magnetic field is introduced to system via Peierls substitution with Landau gauge. Different from the previous calculation in Subsection 6.4.2, the magnetic phase factors are now $4q$ periodic.
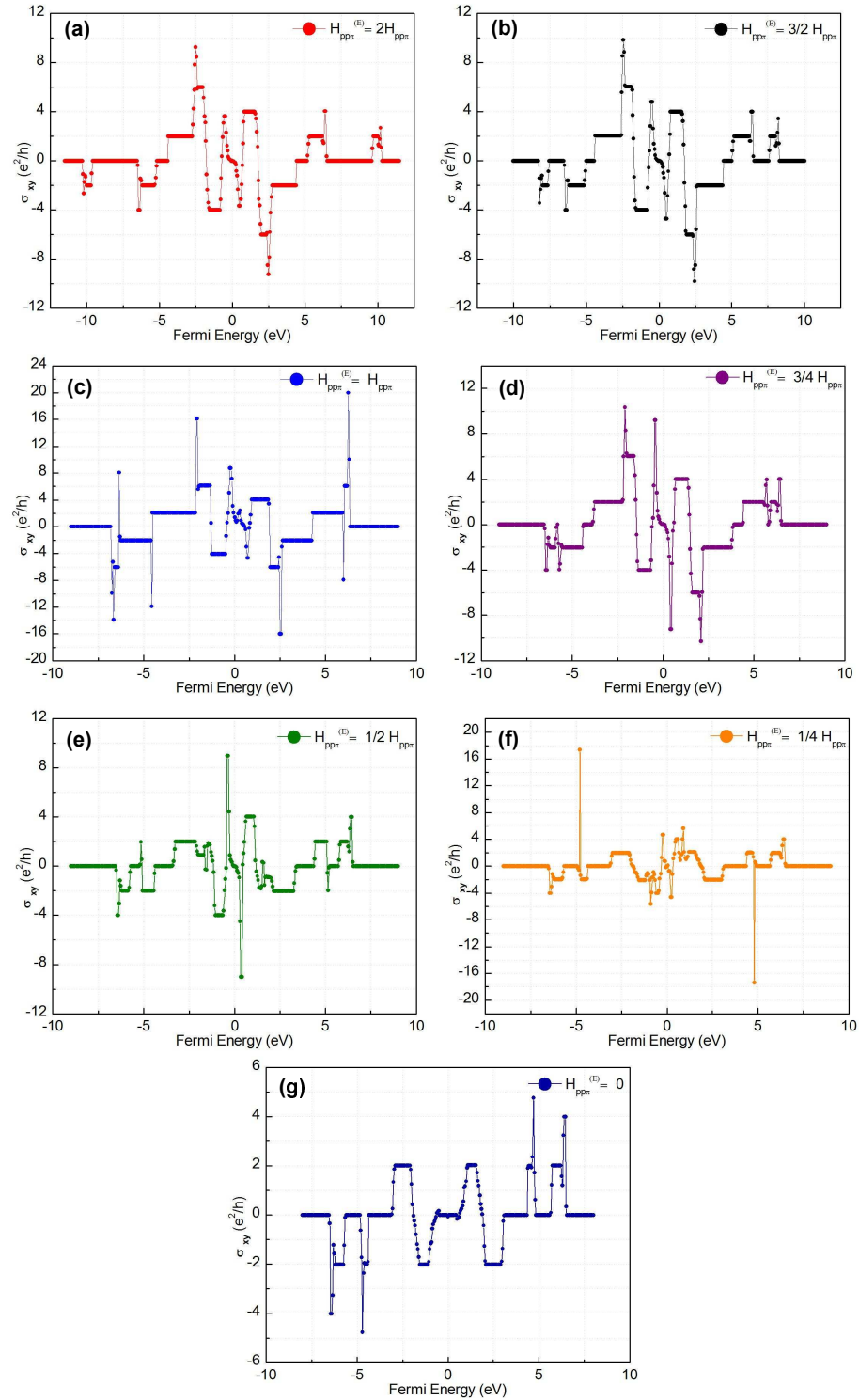
Figure 6.5: Integer quantum Hall conductance for graphene with point defects, only the first order interactions are considered. For all of the calculations $\alpha = p/q = 7/3$ (a) $V_{pp\pi}^E = 2V_{pp\pi}$, (b) $V_{pp\pi}^E = \frac{3}{2}V_{pp\pi}$, (c) $V_{pp\pi}^E = V_{pp\pi}$, (d) $V_{pp\pi}^E = \frac{3}{4}V_{pp\pi}$, (e) $V_{pp\pi}^E = \frac{1}{2}V_{pp\pi}$, (f) $V_{pp\pi}^E = \frac{1}{4}V_{pp\pi}$, (g) $V_{pp\pi}^E = 0$
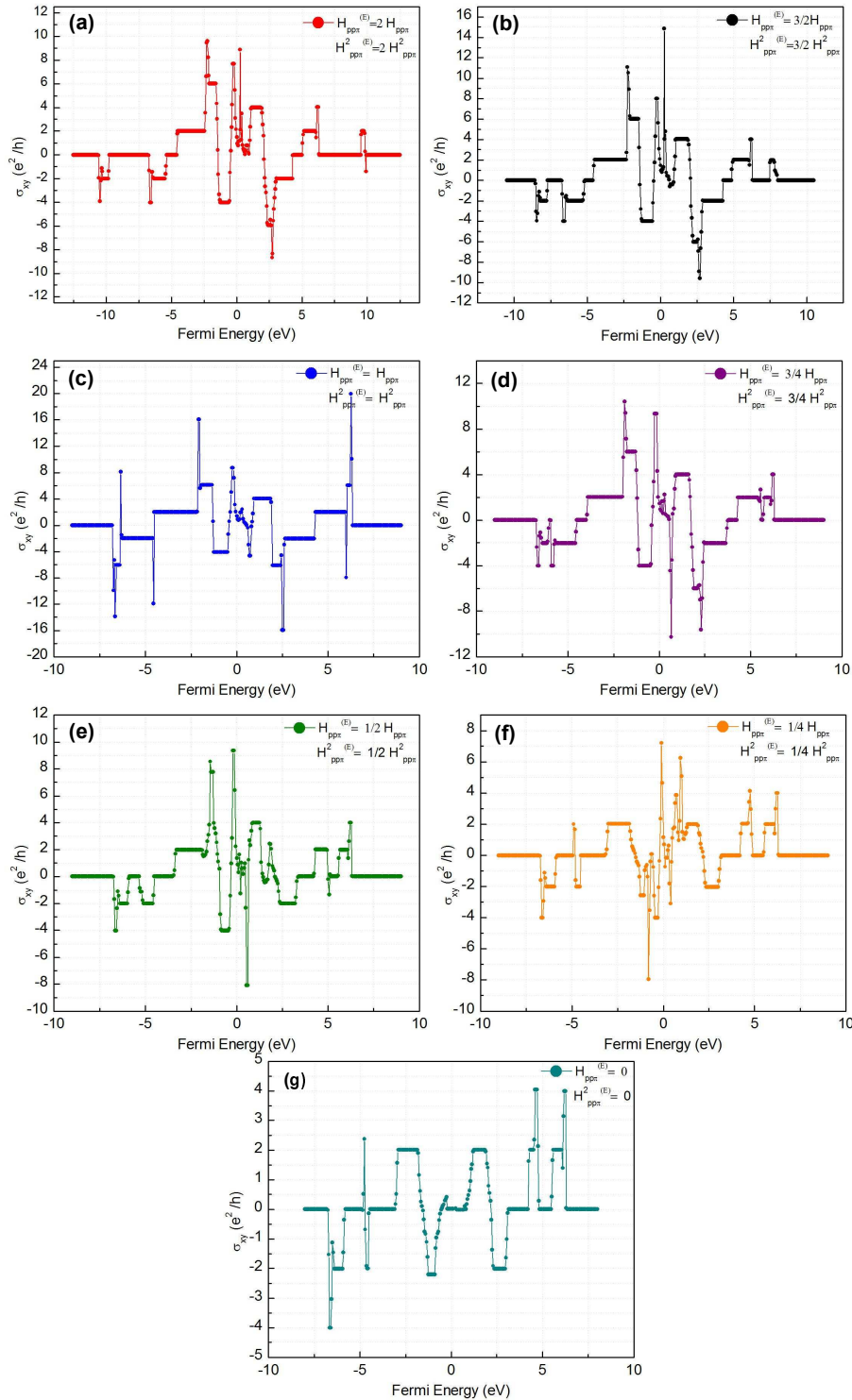
Figure 6.6: Integer quantum Hall conductance for graphene with point defects, both the first and the second order interactions are considered. For all of the calculations $\alpha = p/q = 7/3$ **(a)** $V_{pp\pi}^{E} = 2V_{pp\pi}$ and $V_{pp\pi}^{2(E)} = 2V_{pp\pi}^{2}$, **(b)** $V_{pp\pi}^{E} = \frac{3}{2}V_{pp\pi}$ and $V_{pp\pi}^{2(E)} = \frac{3}{2}V_{pp\pi}^{2}$, **(c)** $V_{pp\pi}^{E} = V_{pp\pi}$ and $V_{pp\pi}^{2(E)} = V_{pp\pi}^{2}$, **(d)** $V_{pp\pi}^{E} = \frac{3}{4}V_{pp\pi}$ and $V_{pp\pi}^{2(E)} = \frac{3}{4}V_{pp\pi}^{2}$, **(e)** $V_{pp\pi}^{E} = \frac{1}{2}V_{pp\pi}$ and $V_{pp\pi}^{2(E)} = \frac{1}{2}V_{pp\pi}^{2}$, **(f)** $V_{pp\pi}^{E} = \frac{1}{4}V_{pp\pi}$ and $V_{pp\pi}^{2(E)} = \frac{1}{4}V_{pp\pi}^{2}$,**(g)** $V_{pp\pi}^{E} = 0$ and $V_{pp\pi}^{2(E)} = 0$

As a result of that and having 8 atoms in the basis, we end up with a $32q \times 32q$ A_m matrix. When the Kubo formula is applied on the eigenvalues and eigenvectors of A_m matrix which is now our magnetic Hamiltonian, we get the Hall conductance as a function of Fermi Energy and magnetic field. We define α as $\alpha = p/q = \phi/\phi_0$, with ϕ_0 is the flux quantum and ϕ is the amount of flux per *enlarged* unit cell. We calculate the Hall conduction in the presence of point defects up to second nearest neighbors for p_z orbitals.

By changing the ratio α by means of changing q, one can work either in the low or high magnetic field regimes. For the high magnetic field regime, we see a similar behavior of the Hall conductance to the square lattice case. The value of Hall conductance is given by the Chern numbers, which come as the solutions for the Diophantine [44, 87] equation when the Fermi energy lies in the gaps. For the square lattice the hall conductance σ_{xy} is given as $n \times e^2/h$, with $n = +1, -1, 0$ when $q = 3$ for the Fermi energy is in a gap. The case for the graphene is slightly different than this; for the single value of $q = 3$, the Hall conductance is given by $\sigma_{xy} = n \times e^2/h$ with $n = +2, -2, +2, -2, 0$. The Hall conductance in major gaps of the spectrum is displayed in Fig. 6.4(a) in units of e^2/h.

Similarly when we have $q = 5$ given in Fig. 6.4(b), we have the conductances as $n = +2, +4, +6, -2, +2, -6, -4, -2, 0$. This behavior of Hall conductance is similar to the results of the square lattice except for the extra factor of 2 originating due to the spin degeneracy in graphene. However, the most interesting case arises when the magnetic field is reduced in magnitude. For both $q = 3$ and $q = 5$, we are still working with really high order magnetic field. In the experiments performed in 2005 [5, 14], the anomalous quantum hall effect was observed for the magnetic fields on the order of 10T.

This strange behavior of conductance is that, it is equal to $2(2n+1)e^2/h$, where n is $0, 1, 2, 3, ...$ We see that this anomalous quantum Hall regime can be probed even with $q = 15$. The corresponding conductance is displayed in Fig. 6.4(c). With setting q to 15 we observe two plateaus around -3 eV $\leq E_F \leq 0$ eV with the conductances are given by $-2(2n+1)e^2/h$, with $n = 0, 1$. A similar structure appears within 0 eV $\leq E_F \leq 3$ eV, with Hall conductances $2(2n+1)e^2/h$, where

$n = 0, 1$. These plateaus are surrounded by scattered-like conductance values, due to the van Hove singularities in the density of states. As we look from the bottom limit of the E_F, we see the step like increasing conductance which is the electron-like conductance behavior. Each step increases the conductance by a factor of two in this region where the gaps are wider than the bands [17]. The same behavior has a mirror image for the Fermi energies on the positive axis as a result of bipartite symmetry of the lattice, since we are just considering the first order interactions. For this case, the observed behavior is the hole-like conductance behavior. The similar spectrum can be seen for $q = 25$ displayed in Fig. 6.4(d), where the anomalous quantum Hall conductance plateaus have the constant conductances with $-2(2n + 1)e^2/h$ and $2(2n + 1)e^2/h$ where $n = 0, 1, 2$. It is also reported that the Hall conductances are given by multiples of Chern numbers when the Fermi energy lies in a gap [17]. In that study, they divide Fermi energy axis into intervals with respect to the magnitude of the hopping constant. They give the value of the Hall conductance as different functions of Dirac-Landau level indices depending on the which interval Fermi energy lies within ($\times 2$ due to the spin degeneracy). Although they calculate the Hall conductances for the entire energy region, they are able to find the value of the Hall conductance only when the Fermi energy lies in a gap. However Kubo formula allows us to calculate the Hall conductance regardless of the position of the Fermi energy. As reported in Ref. [17], Hall conductance displays qualitatively different behavior in the energy range between the van Hove singularities.(See Fig. 6.4(**d**).) The change of electron-like conduction into anomalous integer quantum Hall conduction (anomalous integer quantum Hall conduction into hole-like conduction on the positive Fermi energy axis) occurs at the region of van Hove singularities. At those regions, calculation of Hall conductance requires very fine meshing of k-points, as a result of that our conduction values show a scattered structure. However, two main regimes of Hall conduction, integer quantum Hall effect and anomalous integer quantum Hall effect can still be observed clearly. We achieve the anomalous integer quantum Hall effect for graphene when the magnitude of the magnetic field is reduced, also we observe "even" integer quantum Hall effect through higher magnetic fields. When the magnetic field magnitude is reduced by means of increasing the value of q, we see 5 different behavior regions. As

starting from the smallest value of the E_F, the first region is the electron-like conduction region, the second one is the scattered conductance region due to the van Hove singularities for the corresponding region of the density of states, then comes the anomalous quantum Hall effect region with the neighbor of the other van Hove singularities region, and lastly comes the hole-like conduction region.

We examine the effects of point defects on the Hall conductance for two cases: First with only the nearest neighbor interactions are considered, and second when next nearest hopping is also included. The results for the first nearest neighbors are given as a set of impurity hopping constant strengths in Fig. 6.5. The conductance values are distributed symmetrically over right and left hand sides of the entire region of Fermi energy as a result of lattice bipartite symmetry [40]. Since the Hall conduction is calculated for a single value of α, we set it to $\alpha = p/q = 7/3$. We tried to keep q as small as possible due to being a parameter that defines the size of A_m matrix $(32q \times 32q)$ to be diagonalized. We model several scenarios for atom with label "**e**" being different atoms or just a vacancy located at the atomic position of one of the Carbon atoms. Frame **(a)** corresponds to the case where the atom "**e**" is an impurity with twice the usual hopping constant. The integer quantum Hall effect with even steps can be observed. The frame **(c)** is the pure case where all the atoms including the atom "**e**" are Carbon atoms. One of the differences between frames **(a)** and **(c)** is that, the widths of the plateaus are narrowed down in frame **(a)** with respect to the pure case. Also, this impurity atom modifies the conduction at the bottom and top regions of the Fermi energy scale. This larger hopping constant impurity brings out new conduction plateaus at around $E_f \simeq -10$ eV and $E_f \simeq 10$ eV with Hall conductance of $-2e^2/h$ and $2e^2/h$ separated from the ones in the pure case with plateaus of 0 Hall conductance, respectively. A similar behavior still survives when the hopping constant of atom "**e**" is reduced to $\frac{3}{2}V_{pp\pi}$, given in frame **(b)**. This additional Hall plateaus occur due to increase in the interaction of the impurity atom with the neighboring atoms. The states due to this kind of impurity appear to be delocalized and they contribute to Hall conduction.

The rest of the frames in Fig. 6.5 constitute a second set where the atom "**e**" is again an impurity but this time its hopping constant is reduced to several

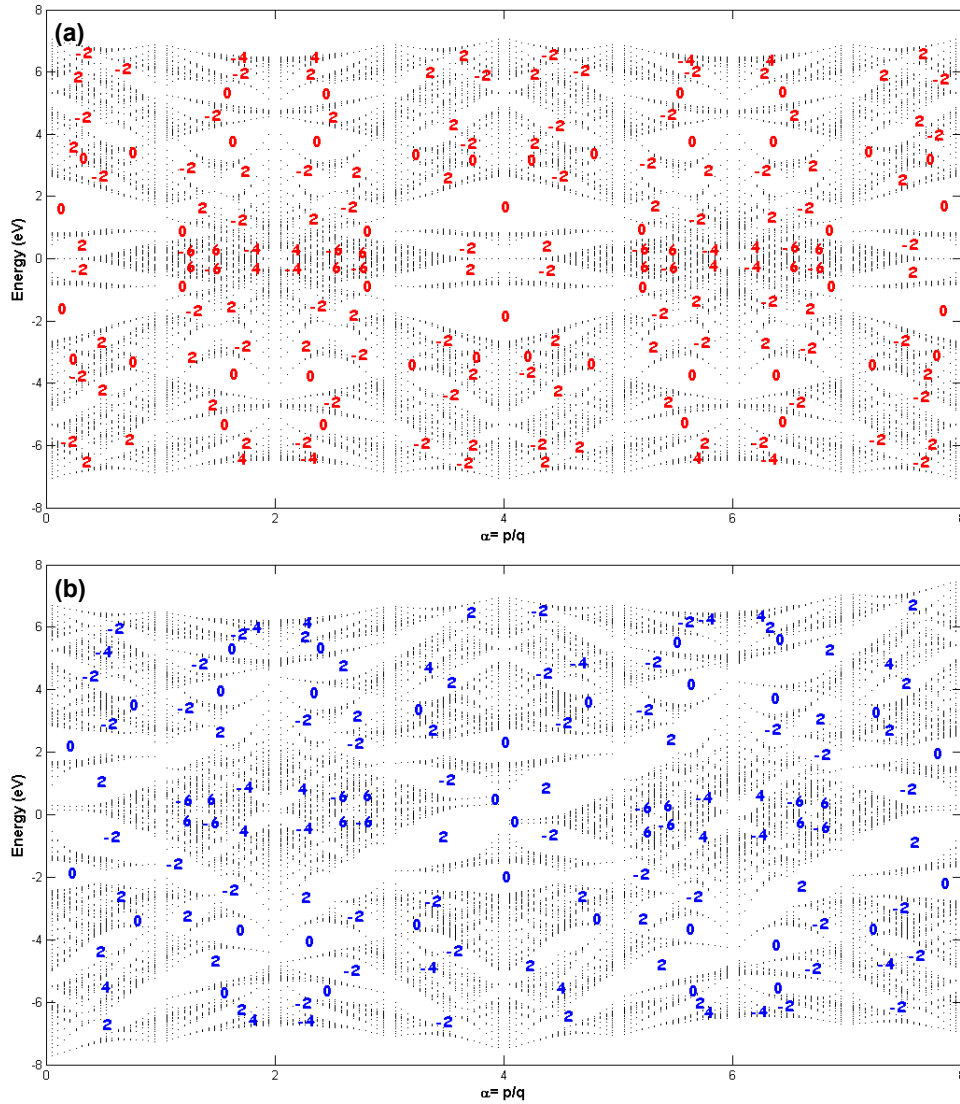Figure 6.7: Portion of Hofstadter butterflies for graphene with point defects. The Hall conduction values of main gaps are scripted on the graphs. **(a)** First order interactions, atom with label "**e**" has $V_{pp\pi}^E = \frac{1}{4}V_{pp\pi}$. **(b)** Both the first and the second order interactions are involved, atom with label "**e**" has $V_{pp\pi}^E = \frac{1}{2}V_{pp\pi}$ and $V_{pp\pi}^{2(E)} = \frac{1}{2}V_{pp\pi}^2$

fractions of the rest of the atoms. The frame **(d)** represents the case of impurity with $V_{pp\pi}^E = \frac{3}{4}V_{pp\pi}$. We see that there are still plateaus with 0 Hall conduction in -5 eV $\leq E_f \leq -2.5$ eV (and 2.5 eV $\leq E_f \leq 5$ eV), but this time they are not followed by $\pm 2e^2/h$ conduction plateaus. In addition, the plateaus with conduction values of $-6e^2/h$ and $6e^2/h$ in the regions -7.5 eV $\leq E_f \leq -5$ eV and 5 eV $\leq E_f \leq 7.5$ eV are reduced to $-4e^2/h$ and $4e^2/h$. Moreover, the constant conduction of $-2e^2/h$ and $2e^2/h$ lying in the regions -6.4 eV $\leq E_f \leq -4.6$ eV and 4.6 eV $\leq E_f \leq 6.4$ eV for the pure case, now split with a plateau of 0 conductance. This splitting is increasing as we keep reducing the hopping parameter of atom "**e**" seen in frames **(e)** and **(f)**, and it has its maximum width in frame **(g)**, where atom "**e**" is the vacancy. When we look at the general trend of Hall conduction in frames **(e)** and **(f)**, we see that the conduction is suppressed with respect to the pure case. As we end up with the vacancy case shown in the last frame, there remain only the plateaus with $-2e^2/h$, $2e^2/h$ and 0 conductance. We can state that, by reducing the hopping constant of atom "**e**", we are interrupting the conduction mechanism. The states due to this kind of impurity appear to be highly localized on the defect atoms in the entire magnetic unit cell, as a result of that they have no contribution to the conductance, rather they suppress the Hall conduction mechanism. As the impurity states are highly localized, our results should not be modified by the random distribution of defects.

The Hall conductance in the presence of the second order interactions is depicted in Fig. 6.6 as a complementary set to Fig. 6.5. Due to the breaking of the bipartite symmetry of the lattice by introducing the 2nd order interactions, the conductance values are no longer symmetrically distributed over the whole region of Fermi energy. Similar to the previous calculation the value of α is equal to $7/3$. We observe that the Hall conductance values are robust with respect to the second order interactions in graphene. However the widths of the plateaus are changed as the widths of the gaps and bands are modified. The larger hopping constant impurity results in new nonzero Hall conduction values, by modifying conduction values at around the bottom and the top regions of the Fermi energy. Similar to the first order calculations, the impurity atoms with smaller hopping constants do not contribute to Hall conduction. Their presence suppress the conduction,
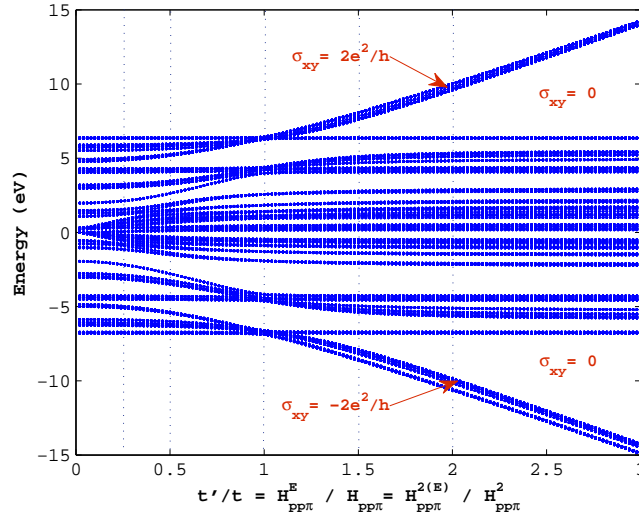
Figure 6.8: The change in the band structure of impure graphene as a function of impurity hopping strengths. $p = 80$ and $q = 31$, both the first and the second neighbor interactions are considered. The conduction values for the dotted lines can be visualized from Fig. 6.6.

and as we keep reducing the hopping constants, we only get conduction plateaus with $-2e^2/h$, $2e^2/h$ and 0 conductance. In Fig. 6.7 portions of Hofstadter Butterflies for imperfect graphene is displayed with Hall conductances indicated in the major gaps. In Fig. 6.7($\mathbf{a}$), only the first order interactions are assumed to exist. The x-axis has the values for $\alpha = p/q = \phi/\phi_0$, where ϕ is the amount of magnetic flux per *enlarged* unit cell. The atom "$\mathbf{e}$" has its hopping strength as one forth of the other atoms. The corresponding Hall conduction is given in Fig. 6.5($\mathbf{f}$) for $\alpha = 7/3$. The gaps with Hall conduction $\pm 6e^2/h, \pm 4e^2/h$ is observed in the neighborhood of $E_f = 0$ eV, which is not observed in Fig. 6.5($\mathbf{f}$) as only a single α value is considered. Fig. 6.7($\mathbf{b}$) is the case when the second order interactions are involved. The breaking of bipartite symmetry result in shifting of gaps and bands with respect to $E = 0$ eV line. This specific case is the case which has the impurity atoms with $V_{pp\pi}^E = \frac{1}{2}V_{pp\pi}$ and $V_{pp\pi}^{2(E)} = \frac{1}{2}V_{pp\pi}^2$. The same $\pm 6e^2/h, \pm 4e^2/h$ valued conduction gaps are still there. Regardless of the effect of second order interactions, the widths of these gaps are larger in comparison with Fig. 6.7($\mathbf{a}$). Hence, our claim of suppression of the Hall conductance -by

means of narrowing of the plateaus- increases with the reduction of the hopping constant of the impurity atom is once again verified.

The effect of impurity atoms on the energy can be visualized via Fig. 6.8. We take $\alpha = p/q = 80/31 \simeq 2.58$, and consider both the first and the second order interactions. We can keep track of the conduction values for the gaps roughly from Fig. 6.6 for the vertical dotted lines. Since the Hall conductance is a topological invariant within a gap, its value does not change unless the bands cross. Thus the conductance value within the major gaps can be easily discerned from the calculation at a single t'/t value. The impurities with smaller hopping constants modify the Hofstadter Butterfly mostly around $E = 0$ eV line. We see that as the impurity hopping strengths are increased up to $V_{pp\pi} = t = t'$, we see new gap and band formation around that region. In addition the width of the spectrum is constant for $t'/t \leq 1$. However, the spectrum displays unusual behavior beyond this point. For the impurities with greater hopping constants, some bands are separated from the rest of the energy spectrum around the minimum and the maximum. The original spectrum mostly remains intact. As we increase the hopping strength to higher values, we see that these bands gain their own self-similar structure separated by zero conductance gaps from the original spectrum. This separation happens roughly around $t'/t = 1.2$. Beyond $t'/t \geq 1.5$, the bulk of the spectrum remains unchanged while two impurity bands further separate increasing the 0 conductance gaps. The Hall conduction plateaus with $\sigma_{xy} = \pm 2e^2/h$ presented in Fig. 6.6 are located within these bands. As a result, we observe that the higher hopping constant impurities produce their own self similar band by modifying the energy spectrum around the top and the bottom values of the energy. A shortcoming of our model is the periodic arrangement of the defect atoms. This periodic arrangement results in well defined $\sigma_{xy} = \pm 2e^2/h$ conduction plateaus within these separated bands and their overall self similar behavior. However, in a real sample the impurities would be distributed over the system randomly. Although this randomness would disturb the self similar structure of these bands, it is not expected to significantly modify their energies. As beyond $t'/t \geq 1.5$, the impurity bands are separated from the bulk of the spectrum by large gaps their behavior should be mostly independent. These

independent bands would still survive under randomness, however one would not expect Hall conduction plateaus within these bands, or any well defined self similarity with regard to defect states.

The anomalous integer quantum Hall effect can be observed for impure graphene, too. However, modelling graphene with point defects of reasonable concentration requires high computational cost. We model defects with 12.5% concentration, which needs a $32q \times 32q$ matrix diagonalization. In order to see anomalous quantum Hall effect which happens at large $q \geq 15$ (Fig. 6.4), we should have larger values for q, which automatically increases the computation time enormously with the sufficient amount of k-point meshing.

In conclusion, we applied Kubo conductance formula to graphene in order to investigate the magnetoconductance properties. For pure graphene our results clearly display the usual and the anomalous quantum Hall effects even though our magnetic fields are much higher than the usual experimental values. This physical limitation for the magnitude of the magnetic field can be overcome by some other indirect methods. For example, it was reported that [104], the shear strain applied to graphene results in a pseudo magnetic field. There is an extra phase factor arising due to the shear strain, which makes the problem identical with the magnetic field application from the point of view of the tight binding method. Our calculations show that even when the magnetic field is large enough to preclude a continuum Dirac equation description of electronic conduction, anomalous and normal integer quantum Hall effects are present for graphene. Anomalous Hall effect is always sandwiched between the usual Hall effect regions with van Hove singularities marking the boundaries between them.

The point defects which are natural ingredients of graphene have interesting effects on the Hall conduction. The defect atoms with smaller hopping constants do not have major contributions to Hall conductance. The states originating from these weakly coupled impurity atoms are highly localized on the defect atoms. This localization is at its maximum for the vacancy case. On the other hand, by increasing the hopping constant of the impurity atoms we increase the interaction of these sites with the neighboring ones. Hence, the states corresponding to

strongly coupled impurities are delocalized. Such delocalized states form separate bands at the extrema of the spectrum creating large, 0 Hall conductance gaps. The bulk of the spectrum and corresponding magnetoconductance properties are not modified by these impurity states.

Chapter 7

Conclusions

In thesis we examined the electronic properties of graphene when it is subjected to external fields. The two example to the external fields we demonstrate were the mechanical strain and the magnetic field. The initial idea for applying strain to graphene was risen due to the possibility of band gap engineering for graphene. A work done by Ref. [27] suggested that it is possible to obtain a band gap opening when there is uniaxial strain acting on graphene. In their study they also used the tight-binding methodology however they neither had the second order interactions nor the σ bands due to the remaining orbitals other than p_z orbitals. In our calculations we see that, the second order interactions as well as the σ bonds have critical value in this problem. In contrast to what they reported, the gap opening due to uniaxial strain for the π bands when there is only first order interactions take place in the system, is actually closed down by other bands crossing the Fermi level. Unfortunately, we propose that graphene is not a suitable material for band gap engineering with a mechanical strain field.

The electronic response of graphene to magnetic field is also investigated during this study. For the problem of response of 2D electronic systems to a perpendicular magnetic field, we started with a simpler lattice configuration "square lattice". We examined the energy spectrum of square lattice under magnetic field which is the Hofstadter Butterfly. We also demonstrate the integer quantum Hall conductance for the square lattice. In addition to the calculations of

the pure systems, we also show the effects of imperfections (impurities or vacancies) introduced to the system periodically and systematically on the Hofstadter Butterfly and Hall conductances. This problem of imperfections is also applied to graphene. The results of imperfections for both lattice configurations are the same: The impurity atoms with smaller hopping constants modify the Hofstadter Butterfly around $E = 0$ eV. They cause formations of new gaps and bands mostly around this region. However, the smaller hopping constant impurities and also the vacancies do not contribute to Hall conductance since they are responsible for the formations of highly localized states. Rather than that they suppress the Hall plateaus and the new gaps due to these kind of impurities have zero Hall conductance. However when there are impurities with higher hopping constants, the Hofstadter Butterfly is modified around the extrema of the energy. The new gaps and bands due to the imperfections are mostly located around these regions. Differently from the previous impurity constant regime, these new formations are due to the extended states created by the higher hopping constant impurities. For graphene, we observe that if the hopping constant of the impurity atom is high enough, two impurity bands leave the bulk of the spectrum and form their own self-similar structure. The gaps in these bands and the gaps around the extrema of the energy for the square lattice have non-zero Hall conductance values. We conclude that the higher hopping constant impurities result extended states which contribute to Hall Conductance.

Bibliography

[1] A.H. Castro Neto, F. Guniea, N.M.R. Peres, K.S. Novoselov ve A.K. Geim, *Reviews of Modern Physics* **81**(1), 109 (2009).

[2] K. S. Novoselov, A. K. Geim, S. V. Morozov, D. Jiang, Y. Zhang, S. V. Dubonos, I. V. Grigorieva, and A. A. Firsov, *Science* **306**, 666 (2004).

[3] K. S. Novoselov, D. Jiang, F. Schedin, T.J. Booth, V. V. Khotkevic, S. V. Morozov, and A. K. Geim, *Proc. Natl. Acad. Sci. U.S.A.*, **102**, 10451 (2005).

[4] K.S. Novoselov, A.K. Geim, S.V. Morozov et al, *Nature* **438**, 197 (2005).

[5] Y. Zhang, Y.-W. Tan, H.L. Stormer, P. Kim, *Nature* (London) **438**, 201 (2005).

[6] C.-H. Park, Y.W. Son, L.Yang, M.L. Cohen, and S.G. Louie, Nano Lett. **101**8, 2920 (2008).

[7] C.-H. Park, L. Yang, Y.W. Son, M.L. Cohen, and S.G. Louie, Phys. Rev. Lett. 101, 126804 (2008).

[8] P. R. Wallace, Phys. Rev. **71**, 622 (1947).

[9] N.M.R. Peres, A.H. Castro Neto, F. Guniea, *Physical Review B* **73**, 195411 (2006a).

[10] A. Calogeracos, N. Dombey, *Contemporary Physics* **40**, 313 (1999).

[11] C. Itzykson, J.-B. Zuber, *Quantum Field Theory*, Dover Press: New York, (2006).

[12] V.P. Gusynin, S.G. Sharapov, *Physical Review Letters* **95**, 146801 (2005).

[13] Y. Zheng and T. Ando, *Phys. Rev. B* **65**, 245420 (2002).

[14] K. S. Novoselov, A. K. Geim, S. V. Morozov, D. Jiang, M. I. Katsnelson, I. V. Grigorieva, S. V. Dubonos, and A. A. Firsov, *Nature* **438**, 197 (2005).

[15] Y. Hasegewa and M. Kohmoto, *Phys. Rev. B* **74**, 155415 (2006).

[16] N. M. R. Peres, F. Guinea, and A. H. Castro Neto, *Phys. Rev. B* **73**, 125411 (2006).

[17] Y. Hatsugai, T. Fukui, and H. Aoki, *Phys. Rev. B* **74**, 205414 (2006).

[18] B. A. Bernevig, T. L. Hughes, S. C. Zhang, H. D. Chen, and C. Wu, *Int. J. Mod. Phys. B* **20**, 3257 (2006).

[19] M. Sato, D. Tobe, and M. Kohmoto, *Phys. Rev. B* **78**, 235322 (2008).

[20] Z.H. Ni, T. Yu, Y. H. Lu, Y. Y. Wang, Y. P. Feng, and Z. X. Shen, *ACS Nano 2* **11**, 2301 2008.

[21] K. S. Kim, Y. Zhao, H. Jang, S. Y. Lee, J. M. Kim, K. S. Kim, J. H. Ahn, P. Kim, J. Choi, and B. H. Hong, *Nature* (London) **457**, 706 (2009).

[22] T. M. G. Mohiuddin, A. Lombardo, R. R. Nair, A. Bonetti, G. Savini, R. Jalil, N. Bonini, D. M. Basko, C. Galiotis, N. Marzari, K. S. Novoselov, A. K. Geim, and A. C. Ferrari, *Phys. Rev. B* **79**, 205433 (2009).

[23] C. Lee, X. Wei, J. W. Kysar, and J. Hone, *et al.*, *Science* **321** , 385 (2008).

[24] M. Huanga, H. Yanb, C. Chena, D. Songb, T. F. Heinzb and J. Honea, *PNAS* **106**(18), 7304 (2009).

[25] M.L. Teague, A.P. Lal, J. Velasco, C.R. Hughes, A.D. Beyer, M.W. Bockrath, C.N. Lau, and N.-C. Yeh, *Nano Lett.* **9**(7), 2542 (2009).

[26] N. Ferralis, R. Maboudian, and C. Carraro, *Phys. Rev. Lett.* **101**, 156801 (2008).

[27] V. M. Pereira, A.H. Castro Neto, N.M. Peres, *Phys. Rev. B* **80**, 045401 (2009).

[28] G. Montambaux, F. Piéchon, J.-N. Fuchs, and M.O. Goerbig, *Phys. Rev. B* **80**, 153412 (2009).

[29] S. Reich, J. Maultzsch, J. Thomsen, and P. Ordejón, *Phys. Rev. B* **66**, 035412 (2002).

[30] S.-M. Choi, S.-H. Jhi, and Y.-W. Son, *Phys. Rev. B* **81**, 081407(R) (2010).

[31] Y.-J. Lin, R. L. Compton, A. R.Perry, W. D. Phillips, J. V. Porto and I. B. Spielman, *Phys. Rev. Lett.* **102**, 130401 (2009).

[32] Y.-J. Lin, R. L. Compton, K. Jiménez-García, J. V. Porto and I. B. Spielman, *Nature* **462**, 628 (2009).

[33] M. Aidelsburger, M. Atala, S. Nascimbène, S. Trotzky, Y.-A. Chen and I. Bloch, *Phys. Rev. Lett.* **107**, 255301 (2011).

[34] K. Jiménez-García, L. J. LeBlanc, R. A. Williams, M. C. Beeler, A. R. Perry and I. B. Spielman, *arXiv:1201.6630v1 [cond-mat.quant-gas]*, (2012).

[35] J. E. Avron, D. Osadchy and R. Seiler, *Physics Today* **56**, 38 (2003).

[36] D. R. Hofstadter, *Phys. Rev. B* **14**, 2239 (1976).

[37] Y. Hasewaga, Y. Hatsugai, M. Kohmoto, and G. Montambaux, *Phys. Rev. B* **41** 9174 (1990).

[38] G. Gumbs and P. Fekete, *Phys. Rev. B* **56**, 3787 (1997).

[39] J.-M. Hou and W.-X. Yang, *Physics Letters A* **373**, 2774 (2009).

[40] R. Rammal *J. Phys.* (Paris) **46**, 1345 (1985).

[41] N. Nemec and G. Cuniberti, *Phys. Rev. B* **74**, 165411 (2006).

[42] S. İslamoğlu, M. Ö. Oktel and O. Gülseren *Phys. Rev. B* **85**, 235414 (2012).

[43] S. İslamoğlu, M. Ö. Oktel and O. Gülseren, *J. Phys C* **24**, 345501(2012).

[44] D.J. Thouless, M. Kohmoto, M.P. Nightingale,and den M. Nijs, *Phys. Rev. Lett.* **49**, 405 (1982).

[45] G. Dresselhaus, M.S. Dresselhaus, R. Saito, *Physical Properties of Carbon Nanotubes*, Imperial College Press: London, (1998).

[46] J.-C. Charlier, Ph. Lambin, and T. W. Ebbesen, *Phys. Rev. B* **54**, 8377 (1996).

[47] E. Kaxiras, *Atomic and Electronic Structure of Solids*, Cambridge University Press: London (2003).

[48] F. Liu, P. Ming, and Ju Li, *Phys. Rev. B* **76**, 064120 (2007).

[49] A. H. Castro Neto and F. Guinea, *Phys. Rev. B* **75**, 045404 (2007).

[50] C. Kittel, *Introduction to Solid State Physics*, John Wiley and Sons, Inc. (1996).

[51] N. W. Ashcroft and N. David Mermin, *Solid State Physics*, Brooks Cole (1976).

[52] M. Methfessel, and A.T. Paxton, *Phys. Rev. B* **40**, 3616 (1989).

[53] R. Peierls, *Z. Phys.* **80**, 763 (1933).

[54] P. G. Harper, Proc. Phys. Soc. London Sect. A **68**, 874 (1955).

[55] J.C. Maxwell, *A Treatise on Electricity and Magnetism*, Clerandon Press: Oxford (1873).

[56] K. von Klitzing, G. Dorda, M. Pepper, *Phys. Rev. Lett.* **45**, 494 (1980).

[57] B. Hückestein, *Rev. Mod. Phys.* **67**, 357 (1995).

[58] T. Ando, *J. Phys. Soc. Jpn* **37**, 622 (1974).

[59] R. E. Prange, *Phys. Rev. B* **23**, 4802 (1981).

[60] R. B. Laughlin, *Phys. Rev. B* **23**, 5632 (1981).

[61] P. W. Anderson, *Phys. Rev.* **109**, 1492 (1958).

[62] H. Aoki, and T. Ando, *Solid State Comm.* **38**, 1079 (1981).

[63] Y. Ono, *J. Phys. Soc. Jpn.* **51**, 2055 (1982b).

[64] J. T. Chalker, *J. Phys. C* **20**, L493 (1987).

[65] M. Kohmoto, *Ann. Phys. (N.Y.)* **160**, 343 (1985).

[66] P. Streda *J. Phys.* C **15**, L717 (1982).

[67] C. Albrecht ,J. H. Smet, K. von Klitzing, D. Weiss, V. Umansky and H. Schweizer, *Phys. Rev. Lett.* **86**, 147 (2001).

[68] J. G. Analytis, S. J. Blundell and A. Ardavan, *Am. J. Phys.* **72**, 613 (2004).

[69] J. Li , Y.-F. Wang and C.-D. Gong *J. Phys: Condens. Matter* **23**, 156002 (2011).

[70] Y.-F. Wang and C.-D. Gong *Phys. Rev.* B **82**, 113304 (2010).

[71] T. Geisel, R. Ketzmeric, and G. Petschel *Phys. Rev. Lett.* **66**, 1651 (1991).; T. Geisel, R. Ketzmeric, and G. Petschel *in Quantum Chaos* edited by G. Casati and B. Chirikov, Cambridge University Press, Cambridge (1995).

[72] T. Schlösser, K. Ensslin, J.P. Kotthaus, M. Holland *Europhys. Lett.* **33**(9), 683 (1996).

[73] V. Gudmundsson and R. R. Gerhardts *Phys. Rev. B* **54**, R5223 (1996).

[74] U. Kuhl and H.-J. Stöckmann *Phys. Rev. Lett.* **80**, 3232 (1998).

[75] O. Richoux and V. Pagneux *Europhys. Lett.* **59**, 34 (2002).

[76] U. Kuhl, S. Barkhofen, T. Tudorovskiy, H.-J. Stöckmann, T. Hossain, L. de Forges de Parny, and F. Mortessagne *Phys. Rev. B* **82**, 094308 (2010).

[77] N. Goldman, *J. Phys. B* **42**, 055302 (2009).

[78] Graduate Texts in Contemporary Physics *The Quantum Hall Effect* edited by R. E. Prange, S. M. Girvin, Springer-Verlag, New York (1987)

[79] N. Goldman, *Ph. D. Thesis*, ULB: Brussels (2009).

[80] Y. Hatsugai *Phys. Rev. Lett.* **71**, 3697 (1993).

[81] H. Ott, E. de Mirandes, F. Ferlaino, G. Roati, G. Modugno, and M. Inguscio, *Phys. Rev. Lett.* **92**, 160601 (2004).

[82] B. Zimmermann, T. Müller, J. Meineke, T. Esslinger and H. Moritz *New J. Phys.* **13**, 043007 (2011).

[83] L. Tarruell, D. Greif, T. Uehlinger, G. Jotzu, and T. Esslinger *Nature* **483**, 302 (2012).

[84] R. M. Ribeiro, V. M. Pereira , N. M. R. Peres, P. R. Briddon, and A. H. Castro Neto, *New J. Phys.* **11**, 115002 (2009).

[85] L. Blakslee, D. G. Proctor, E. J. Seldin, G. B. Stence, and T. Wen, *J. Appl. Phys.* **41**, 3373 (1970).

[86] M. Farjam and H. Rafii-Tabar, *Phys. Rev. B* **80**, 167401 (2009).

[87] M. Kohmoto *Phys. Rev. B* **39**, 11943 (1989).

[88] Y. Hatsugai and M. Kohmoto *Phys. Rev.* B **42**, 8282 (1990).

[89] A. L. C. Pereira and P. A. Schulz, *Phys. Rev. B*, **78**, 125402 (2008).

[90] L.J. LeBlanc, K. Jiménez-García, R. A. Williams, M.C. Beeler, A.R.Perry, W.D. Phillips, and I.B. Spielman *arXiv:1201.5857v1 [cond-mat.quant-gas]* (2012).

[91] R.O. Umucalılar, H. Zhai, and M. Ö.Oktel *Phys. Rev. Lett.* **100**, 070402 (2008).

[92] P. Esquinazi, D. Spemann, R. Hhne, A. Setzer, K.-H. Han, and T. Butz, Phys. Rev. Lett. **91**, 227201 (2003).

[93] A. Hashimoto, K. Suenaga, A. Gloter, K. Urita, and S. Iijima, Nature **430**, 870 (2004).

[94] P. O. Lehtinen, A. S. Foster, Y. Ma, A. V. Krasheninnikov, and R. M. Nieminen, Phys. Rev. Lett. **93**, 187202 (2004).

[95] O. V. Yazyev and L. Helm, Phys. Rev. B **75**, 125408 (2007).

[96] D. N. Sheng, L. Sheng, and Z. Y. Weng, Phys. Rev. B **73**, 233406 (2006).

[97] F. Schedin, A. K. Geim, S. V. Morozov, E. W. Hill, P. Blake, M. I. Katsnelson, and K. S. Novoselov, Nature Materials **6**, 652 (2007).

[98] J.-H. Chen, C. Jang, S. Adam, M. S. Fuhrer, E. D. Williams, and M. Ishigami, Nature Physics **4**, 377 (2008).

[99] T. O. Wehling, A. V. Balatsky, M. I. Katsnelson, A. I. Lichtenstein, K. Scharnberg, and R. Wiesendanger, Phys. Rev. B **75**, 125425 (2007).

[100] Y.-W. Tan, Y. Zhang, K. Bolotin, Y. Zhao, S. Adam, E. H. Hwang, S. Das Sarma, H. L. Stormer, and P. Kim, Phys. Rev. Lett. **99**, 246803 (2007).

[101] H. Zhang, C. Lazo, S. Blgel, S. Heinze, and Y. Mokrousov, Phys. Rev. Lett. **108**, 056802 (2012).

[102] C. G. Van de Walle and J. Neugebauer, J. Appl. Phys. **95**, 3851 (2004).

[103] R. B. Laughlin, Phys. Rev. Lett. **50**, 1395 (1983).

[104] N. Levy, S. A. Burke, K. L. Meaker, M. Panlasigui, A. Zetti, F. Guinea, A. H. Castro Neto, and M. F. Crommie, Science **329**, 544 (2010).